Biological Imaging with Low Coherence Optical Interferometry

by

Michael Richard Hee

B.S., Electrical Engineering
Stanford University, 1990

Submitted to the

DEPARTMENT OF ELECTRICAL ENGINEERING AND COMPUTER SCIENCE

in partial fulfillment of the requirements for the degree of

MASTER OF SCIENCE

at the

MASSACHUSETTS INSTITUTE OF TECHNOLOGY

September 1992

Signature of Author _____
Department of Electrical Engineering and Computer Science
August 28, 1992

Certified by _____
Professor James G. Fujimoto
Thesis Supervisor

Accepted by _____
Campbell L. Searle
Chairman, Department Committe on Graduate Students

Biological Imaging with Low Coherence Optical Interferometry

by

Michael Richard Hee

Submitted to the Department of Electrical Engineering and Computer Science
on August 28, 1992 in partial fulfillment of the requirements
for the degree of Master of Science.

Abstract

A new technique based on low coherence optical interferometry is developed for time-gated imaging through turbid media and the investigation of coherent photon scattering processes. In coherence-gated transillumination, femtosecond pulses and heterodyne detection time-resolve light transmitted through scattering media. Short pulses from a modelocked titanium:sapphire laser enter a fiber-optic interferometer and are split into a reference delay path and a sample transmission path. In highly scattering media, the pulse propagating through the sample temporally broadens due to multiple scattering. The transmitted and broadened sample pulse is recombined with the reference pulse to produce coherent interference signal at a photodetector only for the component of the transmitted pulse which temporally and coherently overlaps the reference pulse.

Coherence-gated transillumination is used to temporally profile the phase coherent constituent of the on-axis, scattered pulse propagating through suspensions of scattering microspheres. The transmitted light consists of an unscattered ballistic component, and a later arriving, temporally broadened, diffuse component. The arrival time and temporal profile of these components are investigated as functions of scattering anisotropy and microsphere concentration. The ballistic peak power is found to attenuate exponentially as the number of scattering mean-free-paths (MFPs), or increasing sample thickness. The diffuse peak attenuates about a factor of 10 more slowly.

Time-gated imaging of hidden objects embedded in scattering microsphere suspensions is demonstrated using both ballistic and early arriving diffuse light. The reference path length is kept constant while the sample is raster scanned over each spatial resolution element. A confocal imaging arrangement takes advantage of spatial rejection of scattered light. Ballistic component images through 27 scattering MFPs of 1 μm diameter microspheres exhibit 100 μm spatial resolution. However, ballistic gated images may only be obtained through relatively thin samples. Ballistic imaging through tissue is revealed to be fundamentally limited by quantum noise and tissue damage thresholds to samples thinner than about 4 mm. Purely spatial resolved confocal or heterodyne imaging techniques are shown to be inferior to time-gated methods for ballistic imaging. Diffuse light images may be obtained through comparatively thicker samples due to the reduced attenuation rate with sample thickness, but at the expense of reduced spatial resolution. The trade-off between spatial resolution and time-gate delay is experimentally investigated and empirical resolution limits are established.

Thesis supervisor: Professor James G. Fujimoto
Department of Electrical Engineering and Computer Science

Acknowledgments

The research presented here would not have been possible without the resources of the ultrafast optics group at MIT. I would like to thank my advisor Jim Fujimoto for providing the opportunity and training to allow me to undertake this work.

Many individuals were essential to the success of this project. Joe Izatt provided the Mie theory calculations, the geometric resolution limit on diffuse imaging, and spent a number of late nights with me mixing dilutions and running the coherence-gated scattering experiments. Joe Jacobson generously provided the use of his titanium:sapphire laser system, and was always on call to produce spur of the moment operating changes and realignments. He also helped to get the initial coherence-gated transillumination system up and working. Eric Swanson generously provided the fiber optics and designed the dual balanced detection system.

Additional thanks go to Dave for getting me started in optics when I was clueless; to Keren for letting me borrow and uncalibrate the spectrum analyzer; to Chih-Kuang for agreeing to use the other lock-in; to Nick for cleaning the machine shop; to Malini for consistent great advice; to Steve for letting me realize that one can actually graduate; to Don for thoughts of CA; and to Jerry for intermittent philosophical e-mail.

Finally, I would like to thank Mom, Dad and Bob for their support, and June for her encouragement and patience.

Six more years to go.

Right.

Contents

Chapter 1

Introduction

The aim of this thesis is to investigate optical imaging of biological tissue using low coherence interferometry. The research assesses the potential of optical interferometry for non-invasive transillumination imaging in scattering systems as well as provides information about fundamental properties of light transport through tissue and other random media.

This thesis develops a coherence-gated transillumination system applicable to fundamental studies of optical scattering and transillumination imaging through turbid media. Transmission measurements of coherent light scattering in model uniform scattering media are described, and the prospect of time-gated imaging of absorbing objects embedded in highly scattering media is investigated.

Optical imaging through turbid biological media is a difficult problem because multiple light scattering and absorption in tissue severely limit image resolution. Despite these limitations, optical transillumination has developed into a specialized diagnostic method, especially in pediatric medicine for cranial and chest pathologies, where tissues are relatively transparent and high resolution is not critical. Recently, there has been interest in transillumination as an alternative or supplement to mammography for the early diagnosis of breast cancer. Optical radiation is relatively safe and may be capable of distinguishing malignant tissue before calcification based on the differential optical properties of the surrounding neovascularization. Multiple light scattering, however, precludes the submillimeter image resolution likely needed for transillumination to become a widespread diagnostic tool for early tumor detection.

Recently, several optical imaging methods have emerged which improve resolution by discriminating against spatial or temporal characteristics of multiply scattered light. Spatially resolved discrimination methods, which are related to confocal imaging, require transmitted light to have a certain directionality or spatial phase coherence before detection.

A short pulse of light propagating through tissue will be severely lengthened due to multiple scattering events and will lose image bearing information. However, a shadowgram of objects embedded in the tissue may be reconstructed by temporally isolating the early-arriving, or least scattered light from the later-arriving diffuse, or multiply scattered light. Time-gated imaging techniques preferentially detect this early light, which has taken a more direct path through the tissue. Incoherent time-gating methods, including electronic, streak camera, and various nonlinear gating techniques, do not require a uniform phase front across the entire detector aperture. In contrast, coherent time-gating methods restrict the spatial and temporal coherence of detected light. Coherent approaches are based on both traditional and electronic time-resolved holographic and interferometric methods.

This thesis develops coherence-gated transillumination, a new coherent imaging approach which takes advantage of both temporal and confocal directional rejection of scattered light. The system is employed to investigate fundamental resolution and sensitivity limits for the entire class of time and spatially resolved imaging techniques.

A specialized fiber-optic interferometer for coherence-gated transillumination imaging has been constructed. Low temporal coherence light from a modelocked titanium:sapphire laser is split into a reference fiber path and a sample transmission path. Scattered light emerging from the sample is recombined with the reference light at a photodetector. Coherent interference between the reference and sample light only occurs at the detector when the reference path length time delay matches the delay of light exiting the sample to within the temporal coherence of the source. This coherence-gating mechanism allows time-resolved analysis of scattered light from the specimen by simply changing the reference path length delay.

Two-dimensional, time-gated transillumination images are formed by raster scanning the specimen over each spatial resolution element while setting the reference arm path length to coherence-gate only the early arriving light transmitted through the

sample. A confocal imaging arrangement in the sample transmission path directionally rejects scattered light and reduces incoherent background light at the detector.

Heterodyne light detection and narrowband signal modulation make the coherence-gated interferometer very sensitive to weak light transmitted through the specimen. The system can detect light as weak as 5 femtowatts, which is 10^{-13} of the incident optical power of 50 mW.

Fundamental time-resolved studies of light scattering with the coherence-gated transillumination interferometer have elucidated coherent scattering mechanisms and tissue optical properties. Prior research employing incoherent, time-resolved detection techniques indicates that a short pulse propagating through a scattering medium splits into an early arriving, unscattered, or ballistic component, and a later arriving, temporally broadened diffuse component. This same division has been observed with coherence-gated transillumination in model scattering media by profiling coherent interference signal amplitude versus reference pulse time delay. The attenuation and profile of both the ballistic and coherent diffuse components have been assessed as functions of scattering cross section, anisotropy, and sample thickness. Model scattering media consist of suspensions of microspheres of varying particle sizes and concentrations.

Preliminary studies of time-gated imaging through turbid media have focused on imaging standard resolution charts through model uniform scattering systems. Tissue phantoms consist of calibrated size microsphere suspensions with well defined scattering properties computed from Mie scattering theory. Image resolution has been investigated as a function of time-gate delay.

Fundamental resolution and sensitivity limits on coherent and incoherent time-gated imaging and non-gated confocal imaging through scattering media are established.

Chapter 2

Optical Imaging Through Turbid Media

2.1 Introduction

Optical imaging of tissue offers the potential of a non-invasive diagnostic with non-ionizing radiation and the possibility of using spectroscopic properties to distinguish tissue type and probe metabolic function. In optically dense or thick tissue specimens, however, absorption and multiple light scattering severely degrade image resolution. Recently, several optical imaging methods have emerged which improve resolution by discriminating against spatial or temporal characteristics of multiply scattered light. This chapter provides an overview of these various imaging techniques.

Spatially resolved discrimination methods require transmitted light to have a certain directionality or spatial phase coherence before detection and attempt to isolate light which has traveled a more direct path through tissue. Time resolved discrimination methods temporally separate the early arriving, least scattered light from the later arriving diffuse, or multiply scattered light, based on the total traversed optical path length. Time resolved discrimination approaches may be classified as either incoherent or coherent imaging systems.

The success of different imaging techniques may be compared by considering image resolution versus sample thickness in number of mean-free-paths (MFPs) and versus total optical energy delivered to each image resolution element during the detection period.

2.2 Review of Incoherent Time-Gating Techniques

Incoherent time-gating methods do not require a uniform phase front across the entire detector aperture and are sensitive only to the intensity of the incident light. Since incoherent imaging methods do not restrict the phase of the detected light, these approaches are potentially more sensitive to diffuse light than coherent time-gating techniques. Incoherent gating methods rely either on electronic switching, or nonlinear optical effects to temporally resolve light.

2.2.1 Streak Camera

The streak camera system temporally profiles the intensity of light entering the camera slit. Light incident on the slit hits a photocathode which emits electrons proportional to the intensity. The electron beam is swept across a CCD camera which produces an image corresponding to light intensity versus time. Time-gated images through turbid media are created by taking a streak camera image for every resolution point on the sample and extracting an early portion of the arriving light. Two-dimensional scanning is required. The temporal resolution in synchroscan mode is typically limited[1-4] to about 10 ps, meaning that submillimeter imaging is probably not possible. However, the long gating times may be beneficial in increasing the amount of diffuse light detected through very thick samples.

Temporal profiles of pulses 1 ps or shorter propagating through non-dairy creamer and polystyrene particle suspensions have shown that the scattered pulse broadens out to hundreds of picoseconds[1,2,4]. One and two-dimensional images of opaque objects about a centimeter wide have been demonstrated through milk, non-dairy creamer, and polystyrene particle suspensions; however, the scattering parameters of these tissue phantoms have not been well quantified[1,2,4]. Both multi-mode fiber and bulk optic delivery systems have been used.

Low temporal resolution prevents isolation of ballistic light and limits streak camera systems to imaging later arriving diffuse light. Yoo, *et. al.*[3] have proposed that the limited temporal resolution is not a handicap for imaging large objects through thick scattering media. They integrate the intensity of the first 50 ps of the diffuse light, which extends for several hundred picoseconds. A spatial resolution of a few millimeters is demonstrated in images of centimeter sized transparent objects placed in a milk solution

with a thickness of 12 forward scattering MFPs. A 5 mW colliding-pulse-modelocked laser was used and the detection time was not reported.

2.2.2 Electronic Gating

Electronic gating methods employ commercial photon counting instruments to temporally resolve light. The minimum temporal resolution is limited by electronic switching times to 2 ps and two-dimensional scanning of either the specimen or the source and detector is required. The systems described below employ multi-mode fiber detection schemes so that light transmitted through the sample is only detected within a certain acceptance angle. Like the streak camera methods, electronic gating techniques are limited to low temporal resolution; however, high temporal resolution may not be needed for imaging large objects through thick scattering media.

Andersson-Engels, *et. al.*[5] have used a 50 mW, 8 ps dye laser to resolve light transmitted through 34 mm of breast tissue with 80 ps resolution. The transmitted light extended to 3-4 ns, and had a time-resolved profile similar to a 35 mm piece of parafilm. The first 100 ps of arriving light was gated to produce one-dimensional images of a human hand, showing bones with about 5 mm resolution. Acquisition time was about 60 s per resolution element so that 3 J was deposited per pixel during detection.

Benaron, *et. al.*[6] have extended the photon-counting technique, employing a 100 ps pulsed diode source and a novel image reconstruction technique. They create one and two-dimensional shadowgrams, and three-dimensional tomographic images by plotting the time of arrival of the first 0.01% of all photons for each image pixel. This time of arrival transformation focuses on the early arriving light, but is a function of the shape of the entire time resolved diffuse curve and may provide more contrast than strict time-gating methods. The system can resolve light propagating through 4 cm of tissue with a collection time of 16 s per pixel. The optical power is not reported.

Like streak camera systems, electronic gating techniques are suited to diffuse light imaging where high spatial resolution is not critical. So far, these methods have been the only time-gating imaging techniques demonstrated on *in vivo* biological specimens.

2.2.3 Nonlinear Gating

Virtually any nonlinear optical effect may be used in conjunction with short pulses to gate early arriving light. Some nonlinear gating techniques can acquire the entire two-dimensional image at once and do not require scanning the probe beam. Femtosecond gating times may be achieved with ultrashort pulsed lasers and fast nonlinear materials. Detection sensitivities are typcially limited by low nonlinear conversion efficiencies and nonlinear gate rejection ratios. Nonlinear gating techniques may be employed to achieve fast gating times without the coherence restrictions of coherent imaging techniques. Most experimental work has focused on using these fast gating times to image with the unscattered ballistic component of the transmitted pulse.

Time-gated imaging using the optical Kerr gate was first proposed by Duguay and Mattick[7] in 1971. They temporally resolved reflections from the front and back of a pair of glass slides. Wang, *et. al.*[8] have subsequently used a CS_2 Kerr shutter and 8 ps pulses at 527 nm to generate two-dimensional images of a 100 μm bar chart placed behind 3 mm of chicken breast and 3.5 mm of human breast. The entire two-dimensional image was obtained at once and no image scanning was required. A time-resolved scattering profile is presented for light propagating through 21.7 scattering MFPs of 460 nm diameter microspheres showing an unscattered ballistic peak at 0 ps delay and a diffuse peak arriving 20 ps later. Images were obtained with 1.3 μJ energy deposited per pixel. The dynamic range of an optical Kerr gate system is limited by the effectiveness of crossed polarizers to eliminated ungated light. Residual transmission is normally about 0.001%. The material relaxation time of CS_2 restricts gating times to slower than 2 ps. The 2 ps temporal resolution prevents gating only the ballistic light, meaning that diffraction limited ballistic imaging in general cannot be achieved. The incomplete extinction of the crossed polarizers limits imaging in highly diffuse media, where the intensity of late arriving diffuse light can be orders of magnitude larger than the early arriving ballistic, or forward scattered light.

Second harmonic generation (SHG) gating eliminates the crossed-polarizer problems of the optical Kerr gate. The relatively fast nonlinearity allows femtosecond gating times. However, unlike the Kerr gate, two-dimensional scanning is required. SHG gating was originally employed by Fujimoto, *et. al.*[9] for single point, time resolved reflectance measurements in skin and cornea with 65 fs pulses and 15 μm spatial resolution. A sensitivity to reflected light of 70 dB was obtained with 2 mW incident power. More recently, Yoo, *et. al.*[10] have used SHG to achieve submillimeter image resolution of one-dimensional opaque objects through 28 scattering MFPs, computed

from Mie theory, of 300 nm latex microspheres in suspension. A colliding pulse modelocked laser outputted 100 fs pulses at 5 mW, which was amplified by a copper-vapor laser to 5 mW [sic.] This reported power is probably incorrect. The sample was scanned over every image resolution element, with a detection bandwidth of 1 kHz. The dynamic range of a SHG system is limited primarily by the noise from laser intensity fluctuations and scattered second harmonic energy from the reference pulse so that shot noise limited detection is almost impossible to achieve.

Transient stimulated Raman amplification[11] has produced direct, two-dimensional images of 300 μm opaque bars through 33 reduced MFPs of non-dairy creamer, and 26 MFPs of 300 nm latex microspheres (image not shown). The MFP of these phantoms was empirically determined by measuring the attenuation of a He-Ne laser propagating through a 100 μm thin slice of the sample. Although 30 ps pulses were used, faster gating times could be attained with femtosecond sources. The images were integrated over 64 shots of Stokes converted light from a 5 Hz modelocked Nd:Yag laser so that 0.8 mJ was deposited over the entire image in 13 s. The sensitivity of stimulated Raman amplification closely approaches the quantum shot noise limit. The author's statement that measurement through the microsphere suspension closely approached the system detectivity limit suggests that the dynamic range is slightly better than e^{26} = 113 dB. Unlike the optical Kerr gate, or SHG gating, the stimulated Raman amplification system allows a combination of two-dimensional image acquisition, shot noise limited sensitivity, and fast gating times. However, the system is complex.

2.3 Review of Coherent Time-Gating Techniques

Coherent time-gating methods restrict the spatial and temporal coherence of detected light and are based on both traditional and electronic time-resolved holographic and interferometric methods. All coherent methods use a short coherence length light source which is split into a reference and a sample beam. The sample beam passes through the scattering media while the reference light propagates through a variable delay path. The two beams are recombined and the interference signal is detected. The length of the reference delay path is adjusted so that interference signal only occurs for the early arriving component of the transmitted light.

Coherent imaging techniques are able to achieve extremely fast gating times with low temporal coherence sources. Since detected light must be phase coherent with the

reference light, however, coherent detection techniques are probably less sensitive to diffuse light than incoherent detection approaches. The fast gating and insensitivity to diffuse light make the coherent methods ideal for ballistic imaging. However, these methods may be less successful for imaging with the early arriving portion of the diffuse light, where high temporal resolution and coherence loss may reduce the available signal power.

2.3.1 Traditional Holography

Traditional time resolved holographic methods[12,13] use low coherence light and conventional holographic film to record a holographic image only for early arriving light. Scanning is not required since the entire holographic image is formed at once. Initial imaging experiments have been performed with absorbing objects placed between glass diffuser plates and parafilm tissue phantoms. A 1 cm high letter "C" with 2 mm linewidth was placed between 3.7 mm of parafilm and imaged with 0.08 mJ / cm^2 from a modelocked dye laser for 200 ms. The source coherence time was 1.1 ps; however, image resolution and sensitivity were not well quantified. A principle limitation of traditional holographic techniques is that fringe visibility may be washed out if the late arriving diffuse light is too intense relative to the coherent interference component. Chemical bleaching must often be employed to remove incoherent film blackening. The sensitivity of a traditional holographic technique strongly depends on the dynamic range and quantum efficiency of the holographic film.

In another initial demonstration, Rebane and Feinberg[13] have used molecular resonances to record the holographic image rather than film. The holographic medium consisted of a polystyrene block doped with protophorphyrin and kept at 2° K in a liquid helium bath. Text on the front and back of a frosted microscope slide was resolved with 500 fs coherence-time pulses from a dye laser. An exposure time of 2-3 minutes was needed to record the hologram, during which 70-100 mJ / cm^2 was deposited on the image. Resolution and sensitivity limits were not well described.

2.3.2 Electronic Holography

Electronic holography[15,16] eliminates the incoherent film blackening problems of traditional holography and the complexities of using molecular resonances to record images. The two-dimensional holographic image is directly formed onto a CCD camera,

which normally has a higher quantum efficiency than film. Numerical image processing techniques separate the interference signal from the incoherent background so that shot noise limited detection is possible. The electronic holography technique is particularly suited to signal averaging which may be necessary for coherent imaging techniques to reduce the effects of image speckle noise. Two-dimensional images of 1 mm pins placed behind 6 mm of chicken breast have been obtained using 120 fs pulses at 820 nm from a 70 mW modelocked titanium:sapphire laser. Seventy-five 100 ms exposures were averaged and speckle decorrelation was produced after each exposure by translating or pinching the sample. The technique, and similar images, have also been demonstrated in the frequency domain, where a continuous-wave tunable dye laser is swept over a large bandwidth and the image is obtained from Fourier reconstruction[17].

2.3.3 Low Coherence Interferometry

Interferometry with low temporal coherence light sources has been used in the relatively transparent tissues of the eye[18-22] to resolve the distance of reflective boundaries, and in the artery[23] to profile coherent optical backscatter intensity versus depth. Scanning the reference arm path length provides depth resolved information, while a broad bandwidth continuous-wave diode light source permits distance resolution better than 20 μm. Signal modulation and heterodyne detection allow shot noise limited sensitivity. Single-mode fiber optics provide spatial rejection of multiply scattered light.

Optical coherence tomography[24] is an extension of low-coherence reflectometry where the sample is scanned in a transverse dimension to produce a profile of optical backscatter versus depth in a two-dimensional thin slice of tissue. Images of retinal and arterial tissue have showed a penetration depth of about 1 mm with 70 μW of incident power and a 4 cm / s longitudinal scanning rate. With these parameters, a detection sensitivity of 90 dB has been attained.

The application of these methods to tissue transillumination has so far been limited by the low incident optical power. Unlike holographic techniques, interferometric methods require raster scanning the sample in two dimensions. However, since each resolution point is obtained separately, confocal imaging principles may be used to provide additional directional rejection of scattered light. In this case, speckle noise is also reduced since light from different resolution elements does not interfere.

2.4 Review of Spatial Rejection Imaging Techniques

Spatial rejection imaging methods discriminate against the directional and spatial coherence properties of multiply scattered light. While time-gated imaging techniques definitely reject light that has traveled a longer path length through a random medium, the same is not true for spatially resolved methods. After propagation through a thick turbid media, it is conceivable that some fraction of the multiply scattered light may be spatially coherent at the detector aperture to degrade image resolution. Results from coherent scattering experiments described in this thesis support this limitation.

Each of the spatially resolved imaging techniques described below has similar properties and may be considered variants of the confocal imaging principle.

2.4.1 Confocal Imaging

In an ideal confocal scanning arrangement[25,26], the turbid medium is located between a point light source and an oppositely arranged point detector which are scanned in tandem across the sample. Dilworth, *et. al.*[27] have theoretically and experimentally demonstrated that confocal scanning provides a resolution improvement over broad beam transillumination, and have also developed a point-spread function deconvolution algorithm. Initial studies have involved tape-strip objects embedded in unquantified diffusers. The same group has recently extended their technique to three-dimensional imaging by taking successive confocal images with the detector moved progressively off-axis from the source, and numerically reconstructing the image[28]. Images of human breasts have been obtained with this method, which mostly show blood vessels residing near the surface.

Imaging with single-mode optical fibers may also be considered confocal[29]. Thus, any incoherent or coherent time-gating technique which uses a pair of scanning single-mode fibers for light delivery and reception also makes use of confocal spatial rejection of multiply scattered light.

2.4.2 Optical Heterodyne Imaging

Optical heterodyne detection requires detected light to be phase coherent with a reference beam over the spatial extent of the detector aperture. This wavefront alignment requirement translates into a directional selectivity similar to confocal imaging and fully

equivalent to detection with a single mode fiber. Sawatari[30] first demonstrated the advantages of heterodyne detection for scanning microscopy, including confocal imaging properties, shot-noise limited detection, discrimination against incoherent background light, and correlation of weak reflected light from the sample with a strong reference beam.

Toida, *et. al.*[31,32] have used the directional selection and sensitivity properties of an optical heterodyne receiver for transillumination imaging. Using a continuous-wave He-Ne laser with a sample beam power of 0.5 mW, a two-dimensional image of a bar chart embedded in a milk-gelatin mixture was obtained by scanning the sample and detecting the interference signal. A modelocked laser is not required and two-dimensional scanning is necessary. The image demonstrates 400 μm resolution, although the scattering medium was unquantified and the signal was thresholded into one of only 16 levels (thereby improving its appearance). The reported dynamic range was a shot noise limited 100 dB with a 10 kHz detection bandwidth.

2.4.3 Spatial Incoherence Imaging

Imaging with spatially incoherent light may also provide confocal rejection of scattered light[17,33]. Unlike confocal or optical heterodyne imaging, however, the entire two-dimensional image may be acquired at once. In this technique, light with reduced spatial coherence propagates through the turbid media and is holographically interfered with a reference beam to create interference only for directionally selected light. Preliminary images of a bar chart placed between ground glass diffusers have been demonstrated.

2.5 Other Optical Imaging Techniques

2.5.1 Increasing Absorption

Imaging at wavelengths where absorption is significant preferentially attenuates light which has traveled a longer path in the medium[34]. This concept has been demonstrated by adding absorbing dye to a scattering suspension of 300 nm microspheres. An image of a 2 mm size object placed behind 25 MFP (computed from

Mie theory) of the scattering medium was obtained using a 15 mW colliding pulse modelocked laser and a video camera for detection.

References

1. K. M. Yoo and R. R. Alfano, "Time-resolved coherent and incoherent components of forward light scattering in random media," Opt. Lett. **15**, 320-322 (1990).

2. P. P. Ho, P. Baldeck, K. S. Wong, K. M. Yoo, D. Lee, and R. R. Alfano, "Time-dynamics of photon migration in semiopaque random media," Appl. Opt. **28**, 2304-2310 (1989).

3. K. M. Yoo, B. B. Das, and R. R. Alfano, "Imaging of a translucent object hidden in a highly scattering medium from the early portion of the diffuse component of a transmitted ultrafast laser pulse," Opt. Lett. **17**, 958-960 (1992).

4. J. C. Hebden, R. A. Kruger, and K. S. Wong, "Time resolved imaging through a highly scattering medium," Appl. Opt. **30**, 788-794 (1991).

5. S. Andersson-Engels, R. Berg, S. Svanberg, and O. Jarlman, "Time-resolved transillumination for medical diagnostics," Opt. Lett. **15**, 1179-1181 (1990).

6. D. A. Benaron, M. A. Lennox, and D. K. Stevenson, "2-D and 3-D images of thick tissue using time-contrained times-of-flight and absorbance (tc-TOFA) spectrophotometry," unpublished manuscript.

7. M. A. Duguay and A. T. Mattick, "Ultrahigh Speed Photography of Picosecond Light Pulses and Echoes," Appl. Opt. **10**, 2162-2170 (1971).

8. L. Wang, P. P. Ho, C. Liu, G. Zhang, and R. R. Alfano, "Ballistic 2-D Imaging Through Scattering Walls Using and Ultrafast Optical Kerr Gate," Science **253**, 769-771 (1991).

9. J. G. Fujimoto, S. De Silvestri, E. P. Ippen, C. A. Puliafito, R. Margolis, and A. Oseroff, "Femtosecond optical ranging in biological systems," Opt. Lett. **11**, 150-152 (1986).

10. K. M. Yoo, Q. Xing, and R. R. Alfano, "Imaging objects hidden in highly scattering media using femtosecond second-harmonic-generation cross-correlation time gating," Opt. Lett. **16**, 1019-1021 (1991).

11. M. D. Duncan, R. Mahon, L. L. Tankersley, and J. Reintjes, "Time-gated imaging though scattering media using stimulated Raman amplification," Opt. Lett. **16**, 1868-1870 (1991).

12. N. Abramson, "Light-in-flight recording: high speed holographic motion pictures of ultrafast phenomena," Appl. Opt. **22**, 215-232 (1983)

13. K. G. Spears, J. Serafin, N. H. Abramson, X. Zhu, and H. Bjelkhagen, "Chrono-Coherent Imaging for Medicine," IEEE Trans. Biomed. Engr. **36**, 1210-1221 (1989).

14. A. Rebane and J. Feinberg, "Time-resolved holography," Nature **351**, 378-380 (1991).

15. H. Chen, Y. Chen, D. Dilworth, E. Leith, J. Lopez, and J. Valdmanis, "Two-dimensional imaging through diffusing media using 150-fs gated electronic holography techniques," Opt. Lett. **16**, 487-489 (1991).

16. E. Leith, H. Chen, Y. Chen, D. Dilworth, J. Lopez, R. Masri, J. Rudd, and J. Valdmanis, "Electronic holography and speckle methods for imaging though tissue using femtosecond gated pulses," Appl. Opt. **30**, 4204-4210 (1991).

17. E. Leith, C. Chen, H. Chen, Y. Chen, D. Dilworth, J. Lopez, J. Rudd, P.-C. Sun, J. Valdmanis, and G. Vossler, "Imaging through scattering media with holography," J. Opt. Soc. Am. A **9**, 1148-1153 (1992).

18. A. F. Fercher, K. Mengedoht, W. Werner, "Eye-length measurement by interferometry with partially coherent light," Opt. Lett. **13**, 186-188 (1988).

19. C. K. Hitzenberger, "Optical measurement of the axial eye length by laser Doppler interferometry," Inv. Ophthalmol. Vis. Sci. **32**, 616 (1991).

20. C. K. Hitzenberger, W. Drexler, and A. F. Fercher, "Measurement of Corneal Thickness by Laser Doppler Interferometry," Inv. Ophthalmol. Vis. Sci. 33, 98-103 (1992).

21. E. A. Swanson, D. Huang, M. R. Hee, J. G. Fujimoto, C. P. Lin and C. A. Puliafito, "High-speed optical coherence domain reflectometry," Opt. Lett. **17**, 151-153 (1991).

22. D. Huang, J. Wang, C. P. Lin, C. A. Puliafito and J. G. Fujimoto, "Micron-Resolution Ranging of Cornea Anterior Chamber by Optical Reflectometry," Lasers Surg. Med. **11**, 419 (1991).

23. X. Clivaz, F. Marquis-Weible, R. P. Salathe, R. P. Novak, and H. H. Gilgen, "High-resolution reflectometry in biological tissue," Opt. Lett. **17**, 4-6 (1992).

24. D. Huang, E. A. Swanson, C. P. Lin, J. S. Schuman, W. G. Stinson, W. Chang, M. R. Hee, T. Flotte, K. Gregory, C. A. Puliafito, J. G. Fujimoto, "Optical Coherence Tomography," Science **254**, 1178-1181 (1991).

25. C. J. R. Sheppard and T. Wilson, "Image formation in confocal scanning microscopes," Optik **55**, 331-342 (1980).

26. P. Davidovits and M. D. Egger, "Scanning Laser Microscope for Biological Investigations," Appl. Opt. **10**, 1615-1619 (1971).

27. D. S. Dilworth, E. N. Leith, and J. L. Lopez, "Imaging absorbing structures within thick diffusing media," Appl. Opt. **29**, 691-698 (1990).

28. D. S. Dilworth, E. N. Leith, and J. L. Lopez, "Three-dimensional confocal imaging of objects embedded within thick diffusing media," Appl. Opt. **30**, 1796-1803 (1991).

29. M. Gu, C. J. R. Sheppard, and X. Gan, "Image formation in a fiber-optical confocal scanning microscope," J. Opt. Soc. Am. A **8**, 1755-1761 (1991).

30. T. Sawatari, "Optical Heterodyne Scanning Microscope," Appl. Opt. **12**, 2768-2772 (1973).

31. M. Toida, M. Kondo, T. Ichimura, and H. Inaba, "Experimental Verificaiion of Image Detection in Highly Scattering Media Using Antenna Properties of Optical Heterodyne Microscope Scheme," Electron. Lett. **26**, 700-702 (1990).

32. M. Toida, M. Kondo, T. Ichimura, and H. Inaba, "Two-Dimensional Coherent Detection Imaging in Multiple Scattering Media Based on the Directional Resolution Capability of the Optical Heterodyne Method," Appl. Phys. B **52**, 391-394 (1991).

33. E. N. Leith, C. Chen, H. Chen, Y. Chen, J. Lopez, P.-C. Sun, and D. Dilworth, "Imaging through scattering media using spatial incoherence techniques," Opt. Lett. **16**, 1820-1822 (1991).

34. K. M. Yoo, F. Liu, and R. R. Alfano, "Imaging through a scattering wall using absorption," Opt. Lett. **16**, 1068-1070 (1991).

Chapter 3

Coherence-Gated Transillumination System

3.1 System Overview

Coherence-gated transillumination is an optical imaging method which simultaneously discriminates against both temporal and directional characteristics of multiply scattered light.

Short coherence length light and coherent interferometric detection temporally resolve light transmitted through a specimen. Short pulses (100 to 400 fs) from a modelocked titanium:sapphire laser enter a fiber-optic modified Mach-Zehnder interferometer, depicted in Fig. 1. A fiber splitter directs these pulses onto a reference mirror and a sample. Light retroreflected from the mirror recombines at another splitter with temporally broadened light transmitted through the sample to create interference signal only for the component of the transmitted pulse which temporally and coherently overlaps the reference pulse. A modelocked titanium:sapphire laser was chosen because of its high output power and broad wavelength tunability; however, short coherence length continuous-wave or long pulse light sources may also be used.

In the sample path, light exiting the fiber is focused over a distance longer than the sample thickness and symmetrically recoupled back into the interferometer. This confocal arrangement provides spatially resolved rejection of scattered photons because light must couple back into a single-mode fiber aperture before detection The coupling requirement is also equivalent to the directional selection properties of another spatially

resolved imaging technique based on an optical heterodyne receiver, as well as spatially incoherent imaging techniques.

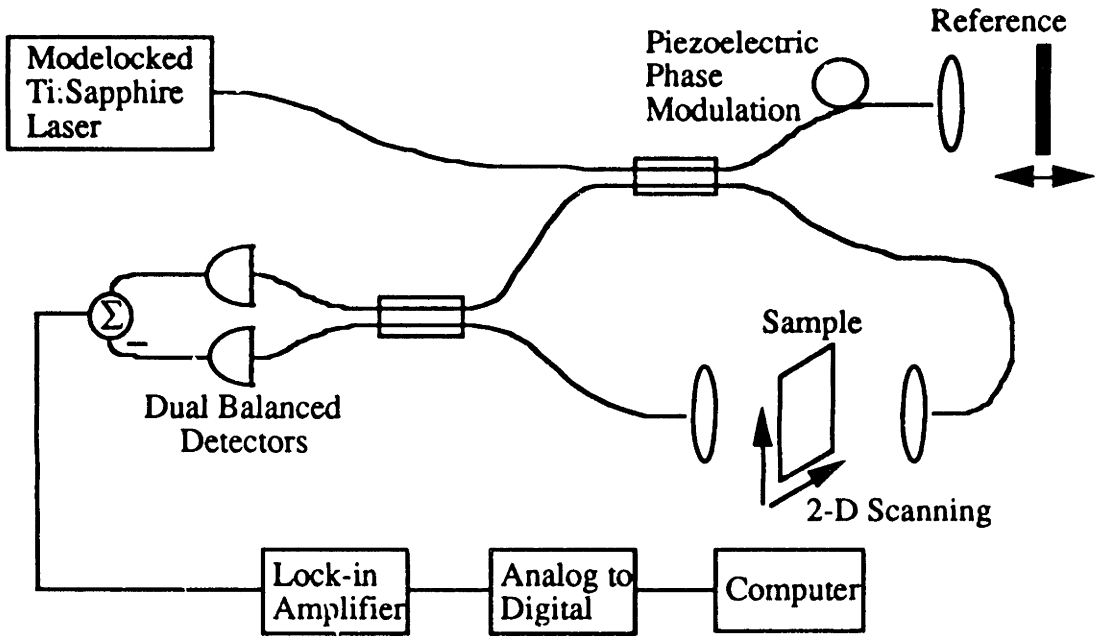

Figure 3.1. Schematic diagram of the coherence-gated transillumination system.

The coherence-gated transillumination system is highly sensitive to small amounts of light transmitted through the sample. The modelocked laser source illuminates the specimen with 50 mW of 830 nm light. The relatively strong reference beam multiplies light emerging from the sample to create discernable interference at the detectors even when the attenuation through the sample is severe. The system can detect coherent transmitted light as small as 10^{-13} of the incident optical power, defining a 130 dB dynamic range. A piezoelectric fiber stretcher phase modulates the interference signal at 10 kHz allowing lock-in demodulation to efficiently frequency filter the desired signal from the surrounding noise. Dual balanced detectors cancel the effect of random laser intensity fluctuations so that the quantum shot noise detection limit is achieved.

3.2 Spatial Rejection of Scattered Light

The single-mode fiber transmission arm of the interferometer behaves as a confocal imaging system. In an ideal confocal transmission imaging arrangement, a point

light source is scanned synchronously opposite a point detector over the object. Image formation is coherent, and resolution is improved since both the source and receiver lens contribute to image construction[1]. In practice, most real confocal systems are only partially coherent, since finite aperture detectors and sources must be used[2].

In contrast, a scanning fiber-optic system is a completely coherent imaging modality, since the single-mode detection fiber demands a consistent phase across the fiber face for fiber coupling[3]. Directional resolved rejection of scattered light occurs because light must also scatter within the collection angle of the receiving lens to reach the fiber face. This directional and spatial coherence requirement is similar to a bulk optic heterodyne receiver[4-6], and holography with spatially incoherent light[7,8].

Since only one image pixel is obtained at a time, either the specimen or the source-detector pair must be scanned in two dimensions. Compared to instantaneous two-dimensional image acquisition, this point-by-point scanning reduces image degradation caused by light scattered out of an illumination pixel into a different detection pixel. For the same reason, a point scanning system should also exhibit diminished image speckle compared to two-dimensional coherent, or holographic imaging techniques.

3.3 Coherence-Gating and Temporal Resolution

The temporal resolution of the system coherence-gate is determined by the coherence length of the light source. In this section, the coherence-gating properties of the interferometric transillumination system will be examined and related to the light source spectral bandwidth. The effect of fiber-arm group velocity dispersion and nonlinear self-phase modulation on the coherence-gate temporal resolution and signal strength will also be analyzed.

3.3.1 Notation and Definitions

The Fourier transform pair is defined according to the electrical engineering convention:

$$f(t) = \int_{-\infty}^{\infty} F(\omega) e^{j\omega t} \frac{d\omega}{2\pi} \tag{3.1}$$

$$F(\omega) = \int_{-\infty}^{\infty} f(t) e^{-j\omega t} dt \tag{3.2}$$

and the following Fourier transform relations will prove useful in the succeeding sections:

$$e^{j\omega_0 t} f(t) \Leftrightarrow F(\omega - \omega_0) \tag{3.3}$$

$$\frac{1}{\sqrt{2\pi\sigma^2}} e^{-\frac{t^2}{2\sigma^2}} \Leftrightarrow e^{-\frac{\sigma^2\omega^2}{2}}. \tag{3.4}$$

Note that the gaussian waveform above has been defined with a characteristic width 2σ equal to 2 standard deviations. For a gaussian waveform, the full-width-half-maximum (FWHM) is related to the standard deviation through $\Delta t_{FWHM} = 2\sigma\sqrt{2\ln 2}$.

3.3.2 Interferometer Analyzed for a Single Fourier Component

The interferometer will first be analyzed for a single monochromatic Fourier component of the source. Then, the analysis will be extended to finite bandwidth sources. Light incident on the interferometer is split at the first fiber beamsplitter into a reference and a sample path. Light retroreflected from the reference mirror is recombined at a second beamsplitter with light transmitted through the sample. Defining the reference and sample electric fields E_R and E_S respectively incident on the second beamsplitter as

$$E_R = A_R e^{-j(\beta_R \ell_R - \omega_R t)}$$

$$E_S = A_S e^{-j(\beta_S \ell_S - \omega_S t)}, \tag{3.5}$$

the fields E_1 and E_2 at the two balanced detectors may be computed from the scattering matrix as

$$\begin{bmatrix} E_1 \\ E_2 \end{bmatrix} = \begin{bmatrix} r & jt \\ jt & r \end{bmatrix} \cdot \begin{bmatrix} E_R \\ E_S \end{bmatrix}. \tag{3.6}$$

The mean photocurrent I after balanced detection is given by the difference of the individual detector photocurrents:

$$I = \frac{\eta e}{\hbar\omega} \cdot \frac{|E_1|^2 - |E_2|^2}{2\eta_0} \tag{3.7}$$

where we have assumed equivalent detectors, η is the detector quantum efficiency, e is the electronic charge, and η_0 is the intrinsic impedance of free space. If the analyzing beamsplitter is exactly 50/50, then $r^2 = t^2 = 1/2$ and the DC photocurrents from each detector exactly cancel leaving the interference term

$$\begin{aligned} I &= \frac{\eta e}{\hbar\omega} \cdot \frac{\mathrm{Re}\left\{jE_R^* E_S\right\}}{\eta_0} \\ &= \frac{\eta e}{\hbar\omega} \cdot \frac{1}{\eta_0} \cdot \cos\left[\beta_S \ell_S - \beta_R \ell_R - (\omega_S - \omega_R)t + \frac{\pi}{2}\right]. \end{aligned} \tag{3.8}$$

As expected, the detectors see interference fringes as the reference and sample arm path lengths ℓ_R and ℓ_S are varied. These fringes oscillate in time at the difference frequency $(\omega_S - \omega_R)$, which in the present case is zero.

Complete interference information is contained in the cross-spectral term $E_R^* E_S$. Therefore, future analysis will focus on this term noting that its real part is basically proportional to the signal photocurrent.

3.3.3 Source Power Spectral Bandwidth and Coherence-Gate Temporal Width in a Dispersion Free Medium

The above analysis for a monochromatic source may be extended to a finite, broad bandwidth source, such as a modelocked laser or a superluminescent diode, by integrating the cross-spectral term $E_R^* E_S$ over the harmonic content of the light source. We redefine the fields incident on the analyzing beamsplitter as

$$\begin{aligned} E_R &= A_R e(\omega) e^{-j\left(\sum_i \beta_{Ri}(\omega)\ell_{Ri} - \omega t\right)} \\ E_S &= A_S e(\omega) e^{-j\left(\sum_i \beta_{Si}(\omega)\ell_{Si} - \omega t\right)} \end{aligned} \tag{3.9}$$

where the sum in exponent allows each interferometer arm to be composed of many segments of different lengths and propagation constants, $e(\omega)$ represents the Fourier transform of the source field, and A_R and A_S account for losses on each interferometer path. The interference signal is the sum of the interference due to each plane wave component, according to

$$I \propto \int_{-\infty}^{\infty} E_R^* E_S \frac{d\omega}{2\pi} = A_R A_S \int_{-\infty}^{\infty} S(\omega) e^{-j\Delta\phi(\omega)} \frac{d\omega}{2\pi} \tag{3.10}$$

where

$$\Delta\phi(\omega) = \sum_i \beta_{Si}(\omega)\omega_{Si} - \sum_j \beta_{Ri}(\omega)\omega_{Ri}. \tag{3.11}$$

$S(\omega) = |e(\omega)|^2$ is the source power spectral density, and $\Delta\phi(\omega)$ is the phase mismatch for each frequency component. Basically, Eq. (3.10) propagates each source frequency component through the interferometer. Note that equal length path segments with identical propagation constants in both interferometer arms will cancel in $\Delta\phi(\omega)$ so that the interferometric signal depends only on the difference in the reference and sample paths. The left term of Eq. (3.10) is the interferometric photocurrent, which is proportional to the cross-correlation of the reference and sample arm fields as a function of reference and sample arm path mismatch. The right term is essentially an inverse Fourier transform relation.

To see the time and frequency relationships more clearly, we examine the ideal case where the reference and sample arm paths consist of a uniform, linear, and non-dispersive material. We assume that the source has a gaussian distributed power spectral density:

$$S(\omega) = \sqrt{\frac{2\pi}{\sigma_\omega^2}} e^{-\frac{(\omega-\omega_0)^2}{2\sigma_\omega^2}} \tag{3.12}$$

with center frequency ω_0, a standard deviation power spectral bandwidth equal to $2\sigma_\omega$ (rad/s), and normalized to unit power:

$$\int_{-\infty}^{\infty} S(\omega) \frac{d\omega}{2\pi} = 1. \tag{3.13}$$

The reference and sample arm propagation constants β_R and β_S are assumed to be equal and linear functions of frequency:

$$\beta_S(\omega) = \beta_R(\omega) = \beta(\omega_0) + \beta'(\omega_0)(\omega - \omega_0). \tag{3.14}$$

The phase mismatch $\Delta\phi(\omega)$ in Eq. (3.11) is then solely determined by the path length mismatch $\Delta\ell = \ell_S - \ell_R$ through

$$\Delta\phi(\omega) = \beta(\omega_0)\Delta\ell + \beta'(\omega_0)(\omega - \omega_0)\Delta\ell. \tag{3.15}$$

The integral over the power spectral density in Eq. (3.10) becomes

$$I \propto A_R A_S \sqrt{\frac{2\pi}{\sigma_\omega^2}} e^{-j\omega_0\Delta\tau_p} \int_{-\infty}^{\infty} e^{-\frac{(\omega-\omega_0)^2}{2\sigma_\omega^2}} e^{-j(\omega-\omega_0)\Delta\tau_g} \frac{d(\omega-\omega_0)}{2\pi} \tag{3.16}$$

where the phase delay mismatch $\Delta\tau_p$ and group delay mismatch $\Delta\tau_g$ are defined as

$$\Delta\tau_p = \frac{\beta(\omega_0)}{\omega_0}\Delta\ell = \frac{\Delta\ell}{v_p} \tag{3.17}$$

$$\Delta\tau_g = \beta'(\omega_0)\Delta\ell = \frac{\Delta\ell}{v_g}. \tag{3.18}$$

v_p is the center frequency phase velocity and v_g is the group velocity in the length mismatched section of the interferometer. Eq. (3.16) is basically a statement of the familiar Wiener-Khintchine theorem: the correlation function is equal to the inverse Fourier transform of the power spectral density. Evaluating the Fourier transform in Eq. (3.16), we find the interferometric photocurrent

$$I \propto A_R A_S e^{-\frac{\Delta\tau_g^2}{2\sigma_\tau^2}} e^{-j\omega_0\Delta\tau_p}. \tag{3.17}$$

The photocurrent contains a gaussian envelope, with characteristic standard deviation temporal width $2\sigma_\tau$ (sec) inversely proportional to the power spectral bandwidth:

$$2\sigma_\tau = \frac{2}{\sigma_\omega}. \tag{3.18}$$

The envelope falls off quickly with increasing group delay mismatch $\Delta\tau_g$ and is modulated by interference fringes which oscillate with increasing phase delay mismatch $\Delta\tau_p$. Thus, Eq. (3.17) defines the coherence-gating properties of the system. For a particular reference arm path length, the detector only sees interference fringes for light emerging from the sample arm at approximately zero group delay. Light arriving more than $\pm\sigma_\tau$ earlier or later falls outside the temporal width of the coherence-gate and is effectively rejected. Translating the reference arm changes the reference path length and moves the coherence-gate in time. Time-resolved profiles of light emerging from specimens placed in the transmission path may be obtained by plotting the interference signal as a function of reference mirror delay.

The temporal width of the coherence-gate in Eq. (3.17) may alternatively be expressed as a free space coherence length by assuming that the group velocity equals the speed of light in free space. For a source with a center wavelength λ and a FWHM wavelength bandwidth $\Delta\lambda$, the FWHM free space coherence-gate length is

$$\ell_{FWHM} = \frac{4\ln 2}{\pi}\frac{\lambda^2}{\Delta\lambda}. \tag{3.19}$$

3.3.4 Effect of Group Velocity Dispersion

In the Sec. 3.3.3, the medium in the interferometer paths was assumed to be dispersion free. A fiber-optic interferometer, however, will have significant amounts of dispersion. There also may be dispersion in the sample. To include group velocity dispersion (GVD) in the analysis, the propagation constants β_R and β_S in each interferometer path are Taylor expanded to second order:

$$\beta(\omega) = \beta(\omega_0) + \beta'(\omega_0)(\omega - \omega_0) + \frac{1}{2}\beta''(\omega - \omega_0)^2. \tag{3.20}$$

We assume that the phase and group velocities are equal in the section of both arms which have different path lengths, and that a GVD mismatch exists in a length L of the sample and reference paths. The frequency dependent phase mismatch from Eq. (3.11) is then

$$\Delta\phi(\omega) = \beta(\omega_0)\Delta\ell + \beta'(\omega_0)(\omega - \omega_0)\Delta\ell + \frac{1}{2}\Delta\beta''(\omega - \omega_0)^2 L \tag{3.21}$$

where $\Delta\ell$ is defined as before, and $\Delta\beta''(\omega) = \beta_S''(\omega) - \beta_R''(\omega)$ is the GVD mismatch between the two paths. Note that only the difference in GVD between the two interferometer arms enters Eq. (3.21). Thus, the deleterious effects of dispersion may be decreased by equalizing the GVD in both interferometer arms.

Inserting $\Delta\phi(\omega)$ into the propagation equation (Eq. (3.10)) gives the photocurrent

$$I \propto A_R A_S e^{-j\omega_0\Delta\tau_p} \int_{-\infty}^{\infty} S(\omega-\omega_0) e^{-j\frac{1}{2}\Delta\beta''(\omega-\omega_0)^2 L} e^{-j(\omega-\omega_0)\Delta\tau_g} \frac{d(\omega-\omega_0)}{2\pi} \quad (3.22)$$

where the phase delay mismatch $\Delta\tau_p$ and group delay mismatch $\Delta\tau_g$ have been defined in Eqs. (3.17) and (3.18). The GVD mismatch multiplies the source power spectral density $S(\omega-\omega_0)$ in a frequency dependent quadratic phase term. The interferometric cross-correlation signal I looks like a short pulse, with Fourier transform $S(\omega-\omega_0)$, which propagates through a length L of dispersive medium with second order dispersion equal to the difference in GVD between the interferometer arms. Thus, just as a short pulse broadens and chirps after propagation through a dispersive medium, the interferometric cross-correlation should also broaden and chirp due to GVD mismatch in the two interferometer arms.

To establish the analogy further, we again assume that the source has a gaussian power spectral density according to Eqs. (3.12) and (3.13). Using Eq. (3.22) to propagate the spectrum through the interferometer, we obtain a modulated interferometric signal with a complex gaussian envelope described by

$$I \propto A_R A_S \frac{\sigma_\tau}{\Gamma(L)} e^{-\frac{\Delta\tau_g^2}{2\Gamma(L)^2}} e^{-j\omega_0\Delta\tau_p} \quad (3.23)$$

where σ_τ is the standard deviation half-width of the dispersion-free coherence-gate from Eq. (3.18). The characteristic width of the coherence-gate in the presence of dispersion, $\Gamma(L)$, is a complex parameter and depends on both the propagation length L and the dispersion-free half coherence-width σ_τ via

$$\Gamma(L)^2 = \sigma_\tau^2 + j\Delta\beta''(\omega_0)L. \quad (3.24)$$

The real and imaginary components of $1/\Gamma(L)^2$ describe the broadening and chirping of the interferometric cross-correlation, respectively, and are

$$\frac{1}{\Gamma(L)^2} = \frac{\sigma_\tau^2}{\sigma_\tau^4 + \tau_{critical}^4} - j\frac{\tau_{critical}^2}{\sigma_\tau^4 + \tau_{critical}^4} \tag{3.25}$$

where we have defined the dispersion parameter

$$\tau_{critical} = \sqrt{\Delta\beta''(\omega)L}. \tag{3.26}$$

Using the expression for $1/\Gamma(L)^2$ in Eq. (3.23) for the interferometric cross-correlation, we discover the gaussian envelope is broadened to the new coherence-width $2\tilde{\sigma}_\tau$:

$$2\tilde{\sigma}_\tau = 2\sigma_\tau\sqrt{1+\left(\frac{\tau_{critical}}{\sigma_\tau}\right)^4}. \tag{3.27}$$

The broadening factor becomes appreciable when the magnitude of the dispersion parameter $\tau_{critical}$ becomes greater than the unbroadened half coherence-width σ_τ. For a typical fused silica fiber at 800 nm, $\beta'' \approx 35$ ps^2 / km[9]. If the unbroadened coherence width $2\sigma_\tau \approx 100$ fs, then coherence-width broadening becomes a factor if the interferometer arm fiber arm lengths are mismatched by at least a length L/2 = 4 cm. For $\tau_{critical} > \sigma_\tau$, the amount of coherence broadening increases approximately linearly with increasing propagation length.

The chirping of the interferometric autocorrelation with increasing path length mismatch $\Delta\ell$ may be described by differentiating the phase in the exponent of Eq. (3.23):

$$k = \frac{d\varphi}{d\Delta\ell} = \beta(\omega_0) - \frac{\tau_{critical}^2}{\sigma_\tau^4 + \tau_{critical}^4}\Delta\beta'(\omega_0)^2\Delta\ell. \tag{3.28}$$

where k describes the spatial frequency of the interference fringes versus the distance measure $\Delta\ell$. For the positive dispersion mismatch regime $\Delta\beta''(\omega_0) > 0$, as the reference arm path length is increased to examine progressively later arriving sample light, $\Delta\ell$ decreases, the wavenumber k increases, and interference fringes occur at the detector more often. It is important to note that the spatial frequency bandwidth of the interference signal does not change relative to the dispersion free case.

Dispersion mismatch also degrades the peak height of the interferometric envelope which reduces the system dynamic range. The degradation in the photocurrent amplitude is described by the multiplicative factor

$$\frac{\sigma_\tau}{|\Gamma(L)|} = \frac{1}{\left[1+\left(\frac{\tau_{critical}}{\sigma_\tau}\right)^4\right]^{\frac{1}{4}}}. \tag{3.29}$$

The reduction of the signal amplitude peak scales as the square root of the coherence-width broadening. Assuming the dynamic range is measured in terms of the signal squared, or photocurrent power, then the loss in dynamic range scales linearly with the coherence-width broadening.

3.3.5 Effect of Fiber Self-Phase Modulation

If a short pulse laser is used as a broad bandwidth, low coherence source, the peak pulse intensities may be strong enough to cause nonlinear effects in the fiber-optics. The effect of nonlinear self-phase modulation (SPM), which causes pulse chirping and spectral broadening in frequency, will be analyzed[9-11].

SPM arises due to a nonlinear, intensity dependent refractive index $n = n_0 + n_2|E|^2$. Since the effect is nonlinear, the power spectrum $S(\omega)$ cannot be propagated through the interferometer as if it were a short pulse as in the previous section. The amount of SPM each interferometer arm will depend on the intensities in the reference and sample path and in general will be unequal.

A general solution would require propagating each pulse separately down both interferometer paths considering both SPM and GVD, and then analyzing the cross-correlation of the pulses at the recombining beamsplitter. Accurate consideration of the simultaneous effects of both SPM and GVD in general, however, requires numerical solution of the nonlinear Schrodinger equation[9]. An incomplete and very approximate analysis is developed here.

Consider first the action of SPM without the effects of GVD. An initially unchirped gaussian pulse, with time-varying envelope

$$E(t) = E_0 e^{-\frac{t^2}{2\sigma^2}} \tag{3.30}$$

and center frequency ω_0 passing through a length L of nonlinear medium will undergo an intensity dependent phase shift

$$\phi(t) = \frac{\omega_0}{c}\left(n_0 + n_2|E|^2\right)L. \tag{3.31}$$

This phase shift will produce an approximate frequency shift and chirp the pulse according to

$$\Delta\omega(t) = -\frac{\partial\Delta\phi(t)}{\partial t} = \frac{\omega_0}{c} n_2|E_0|^2 \frac{2t}{\sigma^2} e^{-\frac{t^2}{2}} L \tag{3.32}$$

where $\Delta\omega(t)$ is the instantaneous frequency shift. The instantaneous frequency of the early portion of the pulse ($t < 0$) is downshifted towards the red and the later arriving portion ($t > 0$) is upshifted towards the blue. The temporal extent of the pulse remains the same; however, its spectral bandwidth is broadened by (very approximately)

$$\Delta bandwidth \approx 2\Delta\omega_{\max} = 2\frac{\omega_0}{c} n_2|E_0|^2 \sqrt{\frac{2}{\sigma^2}} e^{-\frac{1}{2}} L. \tag{3.33}$$

The addition of GVD either enhances or reduces the chirping effect of SPM. For materials with negative dispersion ($\beta'' < 0$), blue frequencies travel faster than red, and the pulse tends to recompress itself during propagation, leading to soliton formation[9]. A silica fiber at 800 nm, however, is in the positive dispersion regime ($\beta'' > 0$)[9], so that the later arriving blue portion of the pulse will travel more slowly than the early arriving red portion. Thus, the pulse further broadens and chirps in time, and the effects of GVD and SPM act synergistically.

Numerical simulations and linear pulse compression experiments[12-14] have demonstrated that the chirp due to SPM and positive GVD is approximately linear. Thus, the effect of SPM on the temporal resolution and sensitivity of the transillumination system may be approximately analyzed by neglecting the propagation through the fiber system and just assuming that two gaussian pulses, with different bandwidths and different amounts of chirp due to the combined action of SPM and GVD, are recombined at the final beamsplitter.

The interferometer is sensitive to the cross-correlation of the two pulses, which may be computed, similar to Eq. (3.16), from the inverse transform of the cross-spectral power density. Following Eq. (3.16), the photocurrent is proportional to

$$I \propto e^{-j\omega_0\Delta\tau_p}\int_{-\infty}^{\infty} E_R^*(\omega-\omega_0)E_S(\omega-\omega_0)e^{-j(\omega-\omega_0)\Delta\tau_g}\frac{d(\omega-\omega_0)}{2\pi} \tag{3.34}$$

where the power spectrum $S(\omega)$ has been replaced by the cross-spectrum $E_R^*(\omega)E_S(\omega)$ between the two pulses. A gaussian spectrum for both $E_R(\omega)$ and $E_S(\omega)$ will be assumed such that

$$E_x(\omega) = \sqrt{P_x}\left(\frac{2\pi}{\sigma_x^2}\right)^{\frac{1}{4}} e^{-\frac{(\omega-\omega_0)^2}{4\sigma_x^2}} e^{-j\frac{\delta_x}{2}(\omega-\omega_0)^2} \tag{3.35}$$

where the subscript x will denote either the reference (R) or sample (S) pulse. The linear chirp comes from the quadratic frequency dependent phase factor and is described by the chirp parameter δ_x. The standard deviation power spectral bandwidth of each pulse is $2\sigma_x$, and the pulse energy is given by

$$\int_{-\infty}^{\infty}\left|E_x(\omega)\right|^2\frac{d\omega}{2\pi} = P_x. \tag{3.36}$$

The inverse Fourier transform in Eq. (3.34) evaluates to the cross-correlation seen at the interferometer output:

$$I \propto \sqrt{P_R P_S}\,\frac{1}{\sqrt{\sigma_R\sigma_S\Gamma^2}} e^{-\frac{\Delta\tau_g^2}{2\Gamma^2}} e^{-j\omega_0\Delta\tau_p} \tag{3.37}$$

where the complex broadening and chirp parameter Γ is defined by

$$\frac{1}{\Gamma^2} = \frac{\tau_{unchirp}^2}{\tau_{unchirp}^4 + \tau_{critical}^4} - j\frac{\tau_{critical}^2}{\tau_{unchirp}^4 + \tau_{critical}^4}. \tag{3.38}$$

$2\tau_{unchirp}$ is the standard deviation coherence-gate width that would be obtained if both pulses were unchirped, or had equal chirps:

$$\tau_{unchirp} = \sqrt{\frac{1}{2\sigma_R^2} + \frac{1}{2\sigma_R^2}} \tag{3.39}$$

while $\tau_{critical}$ describes the amount of chirp mismatch between the reference and sample pulse:

$$\tau_{critical} = \sqrt{\delta_S - \delta_R}\,. \tag{3.40}$$

Equation (3.39) shows that, if both pulses have equal or no chirp, then the coherence-width is primarily determined by the bandwidth of the narrower pulse. Thus, the coherence-width will be determined by the fiber interferometer arm with the least SPM, or smallest pulse energy. This results from the fact that the cross-spectral density of the two pulses is equal to the product each pulse's Fourier transform, which is dominated by the narrower bandwidth.

The minimum standard deviation coherence-width, $2\tau_{unchirp}$, will be broadened with increasing chirp mismatch $\tau_{critical}$ between the pulses according to

$$2\tau_{chirp} = 2\tau_{unchirp}\sqrt{1+\left(\frac{\tau_{critical}}{\tau_{unchirp}}\right)^{\frac{1}{4}}}\,. \tag{3.41}$$

The broadening becomes apparent when the magnitude of the chirp mismatch parameter $\tau_{critical}$ approaches the unbroadened half coherence-width $\tau_{unchirp}$.

The spatial frequency, k, of the cross-correlation will be chirped with increasing path length mismatch $\Delta\ell$, similar to Eq. (3.28):

$$k = \frac{d\varphi}{d\Delta\ell} = \beta(\omega_0) - \frac{\tau_{critical}^2}{\tau_{unchirp}^4 + \tau_{critical}^4}\Delta\beta'(\omega_0)^2\Delta\ell\,. \tag{3.42}$$

Finally, the peak of the cross-correlation signal, which influences the interferometer sensitivity, will decrease by the multiplicative factor

$$\frac{1}{|\Gamma|\sqrt{\sigma_R\sigma_S}} = \sqrt{\frac{2\sigma_R\sigma_S}{\sigma_R^2+\sigma_S^2}}\cdot\frac{1}{\left[1+\left(\frac{\tau_{critical}}{\tau_{unchirp}}\right)^4\right]^{\frac{1}{4}}}\,. \tag{3.43}$$

The first term on the right hand side of Eq. (3.43) describes the signal amplitude degradation due to the bandwidth mismatch between the pulses. For a 3 dB degradation in signal power (signal amplitude squared), the bandwidths of the reference and sample pulse must be mismatched by a factor of about 3.7. The second term on the right hand side of Eq. (3.43) is the signal loss due to chirp mismatch between the pulses, and as seen

the in the previous section, the loss in signal amplitude scales as the square root of the coherence-width broadening.

If a modelocked laser source is employed, then the deleterious effects of SPM may be reduced by ensuring that the reference and sample pulses both have the same bandwidth and chirp. The effect of SPM on a pulse will decrease with increasing propagation distance, since increasing amounts of pulse chirping and broadening will decrease the peak intensity. Thus, the input fiber to the interferometer should be long so that most of the nonlinear effect occurs before the pulse is split into the reference and sample arm paths. In the current transillumination system, the input fiber length is greater than 2 m.

3.4 Signal Modulation

The coherence-gated interferometric signal is placed on an intermediate carrier frequency by piezoelectric phase modulation to enhance detectivity and allow narrowband detection above the predominant low frequency mechanical noise in the system. This section describes this modulation and detection technique.

3.4.1 Narrowband Phase Modulation and AM Lock-In Detection

The reference arm path length is sinusoidally varied at a modulation frequency ω_m by a piezoelectric fiber stretcher mathematically described by

$$\Delta\tilde{\ell} = \Delta\ell + M\sin\omega_m t \tag{3.44}$$

where M denotes the extent of the modulation. If $M << \lambda$, then the modulation only affects the interference fringes in Eq. (3.17) and the envelope of the coherence-gate remains relatively constant, giving

$$I \propto A_R A_S e^{-\frac{\Delta\tau_g^2}{2\sigma_\tau^2}} e^{-j\omega_0\Delta\tau_p} e^{-j\beta(\omega_0)M\sin\omega_m t}. \tag{3.45}$$

For $M << \lambda$, the time-varying phase term can be Taylor expanded:

$$e^{-j\beta(\omega_0)M\sin\omega_m t} \approx 1 - j\beta(\omega_0)M\sin\omega_m t. \tag{3.46}$$

The actual photocurrent is then determined by the real part of the phase terms in Eq. (3.45)

$$I \propto A_R A_S e^{-\frac{\Delta\tau_g^2}{2\sigma_\tau^2}} \left[\cos\omega_0\Delta\tau_p - \sin\omega_0\Delta\tau_p \cdot \beta(\omega_0) M \sin\omega_m t\right] \tag{3.47}$$

and consists of both a DC component and a time varying component at the modulation frequency ω_m.

Lock-in detection demodulates the sinusoidally varying component of the photocurrent by correlating the interferometric signal with a reference signal at the modulation frequency. The modulated component is obtained by subsequent low-pass filtering, giving a DC signal proportional to

$$A_R A_S e^{-\frac{\Delta\tau_g^2}{2\sigma_\tau^2}} \sin\omega_0\Delta\tau_p \cdot \frac{1}{2}\beta(\omega_0) M \tag{3.48}$$

The modulation reduces the signal amplitude by a factor of

$$\frac{1}{2}\beta(\omega_0) M. \tag{3.49}$$

3.4.2 Quadrature Fluctuations

Eq. (3.48) shows that the demodulated interference signal disappears when $\sin\omega_0\Delta\tau_p = 0$, or at the interferometric fringe peaks and valleys, and is at a maximum when the two interferometer path phase delays are in quadrature. These periodic signal drop-outs are undesirable and may be exacerbated by thermal fluctuations in the interferometer path lengths over a distances of more than a quarter wavelength.

The signal amplitude may be averaged over the thermal fluctuations in arm length, resulting in an approximate 6 dB loss of signal power. This averaging, however, limits acquisition time to a few seconds per resolution point, since the thermal fluctuations oscillate at about 1-2 Hz.

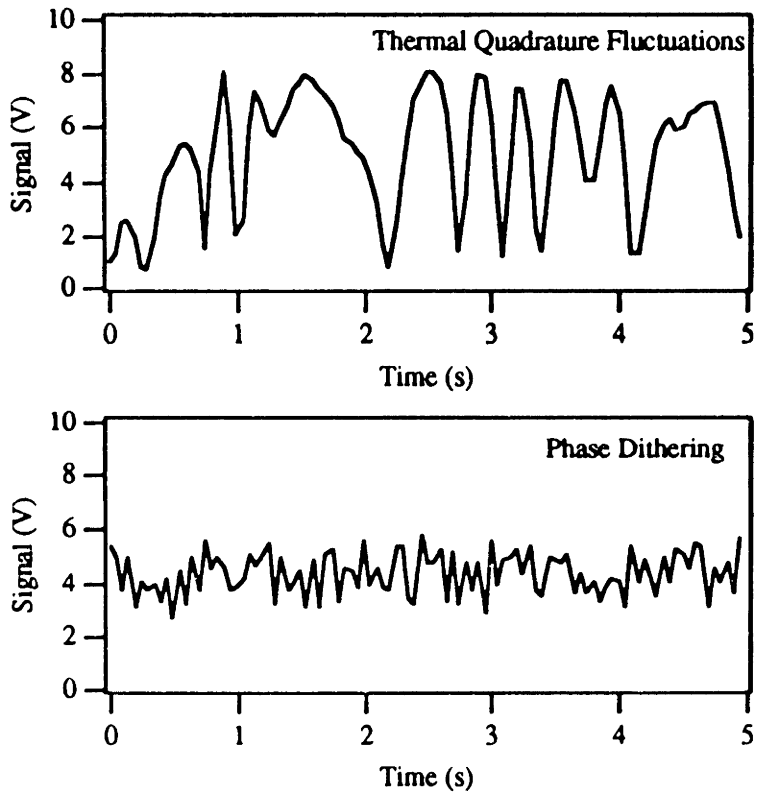

Figure 3.2. Quadrature fluctuations. (A) Demodulated interferometric signal as a function of time showing thermal quadrature fluctuations. (B) Demodulated interferometric signal versus time with the phase dithering and averaging technique employed. Quadrature fluctuations are significantly reduced. A 6 dB loss in peak signal power is incurred.

Faster acquisition may be obtained by inducing artificial path length variations in the interferometer arms over a quarter of a wavelength which are faster than the thermal variations. This phase dithering technique may be accomplished by superposing a low frequency (10-100 Hz) modulation waveform on the piezoelectric transducer responsible for phase modulation of the signal. The low frequency modulation should dither the phase over at least a quarter of a wavelength during the acquisition time for each resolution element to ensure that a signal maximum is reached. The signal detection requires a bandwidth faster than the phase dithering frequency, so that the induced quadrature fluctuations may be sampled and subsequently averaged.

In the current system, as the sample is raster scanned, an image point is taken every 50 ms. The phase dithering frequency and amplitude are set so that the path length

difference varies over a quarter of wavelength in 50 ms. Thus, for every image point, 10 signal samples are taken and averaged over the phase dithering, resulting in a data point which is relatively unaffected by thermal quadrature variations. Figure 3.2 demonstrates the benefits of this phase dithering and averaging, comparing the demodulated interferometric signal versus time taken with and without the phase dithering technique employed.

3.5 Noise Sources, Detection, and Dynamic Range

The dynamic range of the transillumination system is important for imaging through thick samples. This section will review various noise sources, their statistical properties, and the limits they impose on the system sensitivity to weak transmitted light. A design procedure to achieve shot noise limited detection will be presented and trade-offs between different system parameters, such as scanning velocity, spatial resolution, and dynamic range will be discussed.

3.5.1 Notation and Definitions

The statistical expected value operator will be denoted by either $\langle\ \rangle$ or $E\{\ \}$. The operator is linear and commutes with differentiation, integration, and convolution.

A continuous time stochastic process $p(t)$ describes a family of probability distribution functions indexed by the variable t. Thus, $p(t)$ represents a infinite sequence of random variables, which, for a given experiment, defines a continuous function of time.

All the noise sources analyzed here may be described by zero-mean, wide-sense stationary (WSS) stochastic processes. A WSS stochastic process $p(t)$ has a constant mean

$$E\{p(t)\} = m_p \tag{3.50}$$

and a statistical autocorrelation

$$R_p(t_1,t_2) = E\{p(t_1)p(t_2)\} \tag{3.51}$$

which is a function of $t_2 - t_1$ alone, so that

$$R_p(t_1,t_2) = R_p(t_2 - t_1) = R_p(\tau). \tag{3.52}$$

The autocovariance is defined by

$$K_p(t_1,t_2) = R_p(t_1,t_2) - E\{p(t_1)\}E\{p(t_2)\} \tag{3.53}$$

and for zero-mean WSS processes is also a function of $t_2 - t_1$ and equal to the autocorrelation:

$$K_p(t_1,t_2) = K_p(\tau) = R_p(\tau). \tag{3.54}$$

The statistical power spectral density $S(\omega)$ is the Fourier transform of the autocorrelation

$$S(\omega) = \int_{-\infty}^{\infty} R(\tau) e^{-j\omega\tau} d\tau \tag{3.55}$$

and the usual Fourier transform relations apply. $S(\omega)d\omega$ gives the average power stored in the frequency band $d\omega$. The total average power in a process $p(t)$ may be obtained from

$$\overline{P} = \int_{-\infty}^{\infty} S_p(\omega)\frac{d\omega}{2\pi} = R_p(0) = \mathrm{var}\{p(t)\} = \langle p(t)\rangle^2 \tag{3.56}$$

and, as shown, is equal to the process variance.

The spectral density $S(\omega)$ is defined for both positive and negative frequencies and is a real and even function of ω by definition. Many diagnostic instruments such as spectrum analyzers, however, do not distinguish between positive and negative frequencies. For convenience, we define a positive frequency power spectral density $S^+(w)$ such that

$$S^+(w) = S(\omega) + S(-\omega) = 2S(\omega) \qquad \omega > 0. \tag{3.57}$$

This definition will allow direct comparison of theory with experiment.

White noise is a stochastic process which has equal power spectral density at all frequencies, a delta-function autocorrelation, and may be described by

$$S(\omega) = q \tag{3.58}$$

$$R(\tau) = \delta(\tau). \tag{3.59}$$

If a zero-mean WSS stochastic process $x(t)$ with power spectral density $S_x(\omega)$ is passed through a linear system described by the s-domain transfer function $H(s)$, the output stochastic process $y(t)$ is also zero-mean WSS with power spectral density $S_y(\omega)$ given by

$$S_y(\omega) = |H(j\omega)|^2 S_x(\omega). \tag{3.60}$$

3.5.2 Thermal Noise[15-17]

Thermal noise arises from the random motion of particles due to the thermal energy in a system. In electrical circuits, resistive components are the only passive elements which exchange energy with the environment. Thus, thermal noise is associated with the transfer of energy and temperature equilibrium established between a resistor and its surroundings.

The thermal noise density of an arbitrary resistor may be derived from

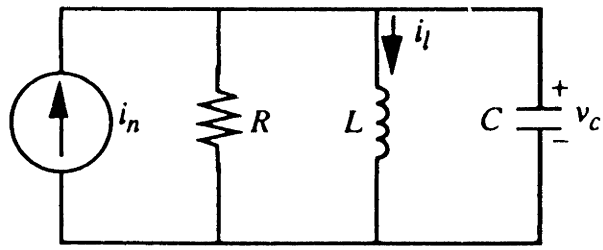

Figure 3.3. Circuit representation of a noisy resistor connected to a resonant LC harmonic oscillator.

thermodynamic reasoning. We assume that the resistor is connected to an arbitrary lossless energy storage system, which in electrical circuits may be composed of capacitors and inductors. The stored energy after thermal equilibrium is established must then equal the energy provided by the resistor interacting with its environment. The statistical characteristics of this energy define the statistics of the noise process.

A noisy resistor may be modeled as the parallel combination of an ideal resistor with resistance R, and a current source i_n which represents the thermal noise or energy

provided by the environment. We compute the power spectral density of the source i_n by assuming that the noisy resistor is connected to an arbitrary resonant LC circuit, as shown in Fig. 3.3. The thermal energy stored in the LC circuit at the resonance frequency will determine the power density of the thermal noise from the resistor at that particular frequency. The parallel LC combination is the electrical analog of the familiar harmonic oscillator; thus, the development of the thermal energy storage will parallel the derivation of the spectral characteristics of black-body radiation[18] or the classical specific heat of a solid[19].

The LC storage element has a resonance frequency $\omega_0 = 1/\sqrt{LC}$. From quantum theory[18], the energy levels available to a harmonic oscillator resonant at frequency ω_0 are restrained to

$$E_n(\omega_0) = \left(n + \frac{1}{2}\right)\hbar\omega_0 \qquad n = 0,1,2... \tag{3.61}$$

In thermal equilibrium at temperature T, the mean energy of the oscillator may be computed from Boltzmann statistics as[16,18]

$$\left\langle E(\omega_0)\right\rangle = \frac{\sum_{n=0}^{\infty} E_n(\omega_0) e^{-\frac{E_n(\omega_0)}{kT}}}{\sum_{n=0}^{\infty} e^{-\frac{E_n(\omega_0)}{kT}}} = \frac{1}{2}\hbar\omega_0 + \frac{\hbar\omega_0}{e^{\frac{\hbar\omega_0}{kT}} - 1}. \tag{3.62}$$

This mean thermal energy is exactly the mean electrical energy stored in the circuit, so that the following relationship holds:

$$\left\langle E(\omega_0)\right\rangle = \frac{1}{2}L\left\langle i_l^2\right\rangle + \frac{1}{2}C\left\langle v_c^2\right\rangle \tag{3.63}$$

where $\left\langle i_l^2\right\rangle$ and $\left\langle v_c^2\right\rangle$ are the variances of the zero-mean inductor current i_l and capacitor voltage v_c, respectively.

We want to relate the power spectral density $S_{i_n}(\omega)$ of the noise current i_n to the mean energy $\left\langle E(\omega_0)\right\rangle$. This relationship is possible through the linear system defined by the circuit in Fig. 3.3. The s-domain transfer function $H(s)$ between the noise current $I_n(s)$ and the capacitor voltage $V_c(s)$ is

$$H(s) = \frac{V_c(s)}{I_n(s)} = \frac{s}{C} \frac{1}{s^2 + \frac{\omega_0}{Q} s + \omega_0^2} \tag{3.64}$$

where the quality factor Q is

$$Q = R\sqrt{\frac{C}{L}}. \tag{3.65}$$

The transfer function between the noise current $I_n(s)$ and inductor current $I_l(s)$ is simply

$$\frac{I_l(s)}{I_n(s)} = \frac{1}{sL} H(s). \tag{3.66}$$

Using Eq. (3.56), we rewrite Eq. (3.63) in terms of the power spectral densities $S_{i_l}(\omega)$ and $S_{v_c}(\omega)$ of the inductor current and capacitor voltage, respectively:

$$\langle E(\omega_0) \rangle = \frac{1}{2} L \int_{-\infty}^{\infty} S_{i_l}(\omega) \frac{d\omega}{2\pi} + \frac{1}{2} C \int_{-\infty}^{\infty} S_{v_c}(\omega) \frac{d\omega}{2\pi}. \tag{3.67}$$

The linear system relates these spectral densities to the power spectrum of the noise source through Eq. (3.60) and leads to

$$\langle E(\omega_0) \rangle = \frac{1}{2} L \int_{-\infty}^{\infty} \frac{|H(j\omega)|^2}{\omega^2} S_{i_n}(\omega) \frac{d\omega}{2\pi} + \frac{1}{2} C \int_{-\infty}^{\infty} |H(j\omega)|^2 S_{i_n}(\omega) \frac{d\omega}{2\pi}. \tag{3.68}$$

We evaluate the integrals by supposing that we have chosen the inductance L to be very small and the capacitance C to be very large so that Q approaches infinity. In this limit, $|H(j\omega)|^2$ approaches a pair of delta functions centered at the positive and negative resonance frequencies

$$\lim_{Q \to \infty} |H(j\omega)|^2 = \frac{1}{2} \frac{R}{C} \left[\frac{1}{2} \delta(\omega - \omega_0) + \frac{1}{2} \delta(\omega + \omega_0) \right] 2\pi \tag{3.69}$$

and the integrations simplify to

$$\langle E(\omega_0) \rangle = \frac{1}{2} R \cdot S_{i_n}(\omega_0). \tag{3.70}$$

Since the choice of resonance frequency is arbitrary, we can drop the zero subscript and insert Eq. (3.62) to arrive at the expression for the power spectral density of the noise current:

$$S_{i_n}(\omega) = S_{i_n}(-\omega) = \frac{2}{R}\left[\frac{1}{2}\hbar\omega + \frac{\hbar\omega}{e^{\frac{\hbar\omega}{kT}} - 1}\right] \qquad \omega \geq 0. \tag{3.71}$$

Any real resistor will be a noise source, providing a current with power spectral density given by Eq. (3.71).

For normal electronic frequencies, we can neglect the term due to the zero-point energy in Eq. (3.71) and Taylor expand the exponential. The noise current density is approximated by white noise with density

$$S_{i_n}(\omega) = \frac{2kT}{R}. \tag{3.72}$$

Through Thevenin's theorem, a noisy resistor may also be modeled as an ideal resistor in series with a zero-mean voltage source v_n, with spectral density

$$S_{v_n}(\omega) = 2kTR. \tag{3.73}$$

3.5.3 1/f Noise [20]

$1/f$ noise, or flicker noise, is present in all active electronic devices and optical systems. The power spectral density of flicker noise has a $1/f$ frequency dependence and its amplitude distribution is generally non-gaussian. The origins of $1/f$ noise are varied, but it is often caused by traps associated with contamination and defects in semiconductor materials. These traps capture and release carriers randomly with a certain time-constant, creating a noise density that is concentrated at low frequencies. In optical set ups, $1/f$ noise may also result from mechanical vibrations of optical mounts and components which tend to resonate at low-frequencies.

The effect of $1/f$ noise may be reduced by modulating and detecting the desired signal at a frequency above the effect of the predominant time-constants in the system, where the flicker noise density is reduced compared to other sources.

3.5.4 Shot Noise [15,17]

Shot noise arises from current fluctuations due to the quantization of light and charge. A photodetector will emit charge corresponding to a mean rate defined by the photocurrent; however, the time between specific emission events will be random. Thus, on a microscopic scale, the fact that the charge must occur in finite increments induces random fluctuations in the current. We expect that the amount of photodetector shot noise should somehow be proportional to both the electronic charge and the mean photocurrent.

We assume that the probability of a photon arrival (and consequently the emission of an electron by the photodetector) during a given infinitesimal interval dt is independent of all other intervals and equal to λdt, where λ is the mean arrival rate. The electron emission times are therefore described by a Poisson distributed random variable[21] according to

$$\Pr[\text{k emissions in time } \Delta t] = \frac{e^{-\lambda \Delta t}(\lambda \Delta t)^k}{k!}. \tag{3.74}$$

The assumption of Poisson statistics for electron emission times is not fundamental and may be derived from the quantum mechanical statistics of the single-mode photon coherent state[18]. The mean of the above Poisson density function defines the average number of electrons emitted in a time interval Δt and equals $\lambda \Delta t$. The correlation of Poisson random variable x is

$$E\{x^2\} = \lambda \Delta t + (\lambda \Delta t)^2. \tag{3.75}$$

We will further assume that each emitted charge has an infinitesimal extent in time, so that the photocurrent may be modeled as a sequence of delta functions, each with area equal to the electronic charge e, which have Poisson distributed arrival times. The time-average of this Poisson impulse process will equal the average photocurrent $\langle i \rangle$. To arrive at the statistics of this process, we form the stochastic process $q(t)$, which represents the total amount of charge emitted by the photodetector between time 0 and t. For each given t, $q(t)$ is a Poisson distributed random variable, so that its mean and correlation are

$$E\{q(t)\} = e\lambda t \tag{3.76}$$

$$E\{q(t)^2\} = e^2\left[\lambda t + (\lambda t)^2\right] \tag{3.77}$$

respectively. To compute the stochastic process autocorrelation, $R_q(t_1,t_2) = E\{q(t_1)q(t_2)\}$, we use the fact that for Poisson emissions, different time intervals are statistically independent. For $t_1 < t_2$,

$$\begin{aligned} E\{q(t_1)q(t_2)\} &= E\{q(t_1)^2\} + E\{q(t_1)[q(t_2)-q(t_1)]\} \\ &= E\{q(t_1)^2\} + E\{q(t_1)\}E\{q(t_2)-q(t_1)\} \\ &= e^2\left[\lambda t_1 + (\lambda t_1)^2 + \lambda t_1 \lambda (t_2 - t_1)\right] \end{aligned} \tag{3.78}$$

Since $R_q(t_1,t_2) = R_q(t_2,t_1)$ by definition, we have

$$R_q(t_1,t_2) = e^2\left[\lambda \min(t_1,t_2) + \lambda^2 t_1 t_2\right]. \tag{3.79}$$

The Poisson impulse process which describes the shot noise photocurrent is the time-derivative of the random process which describes the total charge. Defining the stochastic process

$$i(t) = \frac{dq(t)}{dt} \tag{3.80}$$

we can immediately compute its mean $E\{i(t)\}$, which must equal the average photocurrent $\langle i \rangle$

$$E\{i(t)\} = E\left\{\frac{dq(t)}{dt}\right\} = \frac{d}{dt}E\{q(t)\} = e\lambda = \langle i \rangle \tag{3.81}$$

thereby defining the rate parameter λ. The autocorrelation $R_i(t_1,t_2)$ of the shot noise process is

$$\begin{aligned} R_i(t_1,t_2) = E\{i(t_1)i(t_2)\} &= E\left\{\frac{dq(t_1)}{dt_1}\frac{dq(t_2)}{dt_2}\right\} = \frac{\partial}{\partial t_1}\frac{\partial}{\partial t_2}R_q(t_1,t_2) \\ &= e^2\left[\lambda\delta(\tau) - \lambda^2\right] \end{aligned} \tag{3.82}$$

and is a function of $\tau = t_2 - t_1$ alone. Thus, shot noise is WSS.

The shot noise power spectral density $S_i(\omega)$ is just the Fourier transform of Eq. (3.82) and is given by

$$S_i(\omega) = e^2\left[2\pi\lambda^2\delta(\omega) + \lambda\right] = \langle i\rangle^2 2\pi\delta(\omega) + e\langle i\rangle. \tag{3.83}$$

Neglecting the delta function at zero frequency which just results from the mean DC value of the photocurrent, the shot noise associated with any photocurrent $\langle i\rangle$ is white, and its power spectral density is proportional to the photocurrent and the electronic charge via

$$S_i(\omega) = e\langle i\rangle. \tag{3.84}$$

Note that the noise power $S_i(\omega)$ scales as the square root of the photocurrent power $\langle i\rangle^2$.

The above analysis only applies for a constant mean photocurrent. This assumption is justified for the transillumination system since in practice the light incident on the photodetectors will be dominated by the constant light emitted from the reference arm.

3.5.5 Local Oscillator Noise and Dual Balanced Detection

In a conventional interferometer with only one detector, the interferometric photocurrent consists of two DC components and an interference component. Following the results of Sec. 3.3.2, for an ideal plane wave light source the photocurrent is given by

$$I \propto \frac{1}{2}A_R^2 + \frac{1}{2}A_S^2 + \cos\left[\beta_S\ell_S - \beta_R\ell_R - (\omega_S - \omega_R)t + \frac{\pi}{2}\right] \tag{3.85}$$

recalling that fields incident on the detector are

$$E_R = A_R e^{-j(\beta_R\ell_R - \omega_R t)}$$

$$E_S = A_S e^{-j(\beta_S\ell_S - \omega_S t)}. \tag{3.86}$$

Detection involves separating the interferometric component of the signal from the DC components, which may be accomplished by phase modulation and narrowband lock-in demodulation as described in Sec. 3.4.

If the source has random intensity fluctuations at the phase modulation frequency, then the amplitudes of the fields, A_R and A_S, will actually vary with time and invade the detection bandwidth which is centered around the modulation frequency. These intensity fluctuations will then be indistinguishable from the real interference signal and will degrade the dynamic range of the system. This effect is known as local oscillator noise.

Dual balanced detection reduces the effect of local oscillator noise by employing two detectors and subtracting their photocurrents to cancel out the unwanted DC components[22]. Cancellation of the DC components while preserving the interference signal is possible because the interference signal is 180° out of phase at each detector. This phase relation is evident from evaluating the scattering matrix presented earlier in Eq. (3.6)

Dual balanced detection does not reduce shot noise. The zero-mean shot noise stochastic processes from each detector are statistically uncorrelated, so that their noise variances add when the photocurrents are subtracted.

3.5.6 Excess Intensity Noise

Excess intensity noise includes any noise source whose power spectral density scales linearly with the mean photocurrent power $\langle i \rangle^2$. Examples include excess local oscillator noise not canceled by balanced detection, and mechanical motion of optical mounts that does not have a $1/f$ character. The spectral density of the noise current may be approximated as white over the frequency band of interest and may be modeled as

$$S_i(\omega) = e\gamma\langle i \rangle^2 \tag{3.87}$$

where the noise parameter γ must usually be determined by experiment.

3.5.7 System Design for Shot Noise Limited Sensitivity

Figure 3.4 shows a schematic diagram of the dual balanced detection circuit. The photocurrents are subtracted at a node, and the difference photocurrent is converted into a

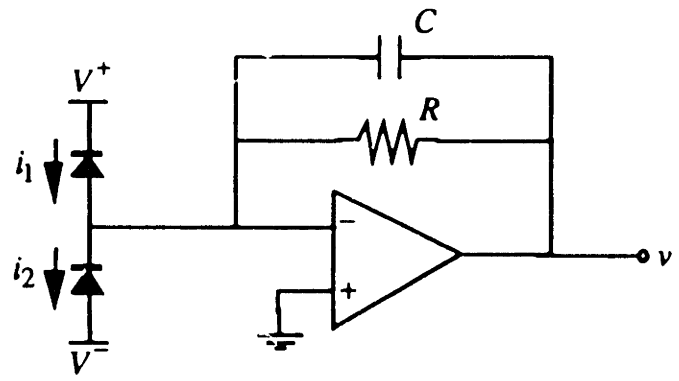

Figure 3.4. Schematic diagram of the dual balanced detectors and the transimpedance amplifier.

voltage by a transimpedance amplifier. For low frequencies, the signal voltage v at the output is equal to

$$v = (i_1 - i_2)R \tag{3.88}$$

where R is the amplifier feedback resistance, and i_1 and i_2 are the two detector photocurrents. The capacitance C in parallel with the feedback resistance is necessary for amplifier stability and causes the amplifier to roll-off at 20 dB/decade for frequencies above the dominant pole at

$$f_c = \frac{1}{2\pi RC}. \tag{3.89}$$

For the component values $R = 1$ MΩ and $C = 0.01$ pF, the transimpedance amplifier bandwidth is $f_c = 159$ kHz.

The ability of the balanced detection circuit to cancel local oscillator fluctuations was assessed by placing a sinusoidally modulated light source incident on both detectors. The amount of cancellation was defined as the ratio of the output power with no detectors blocked divided by the output power with one detector blocked. Figure 3.5 plots the cancellation as a function of source modulation frequency showing that 60 dB of cancellation is obtained at a modulation frequency of 10 kHz. The amount of cancellation decreases quickly for frequencies above 10 kHz.

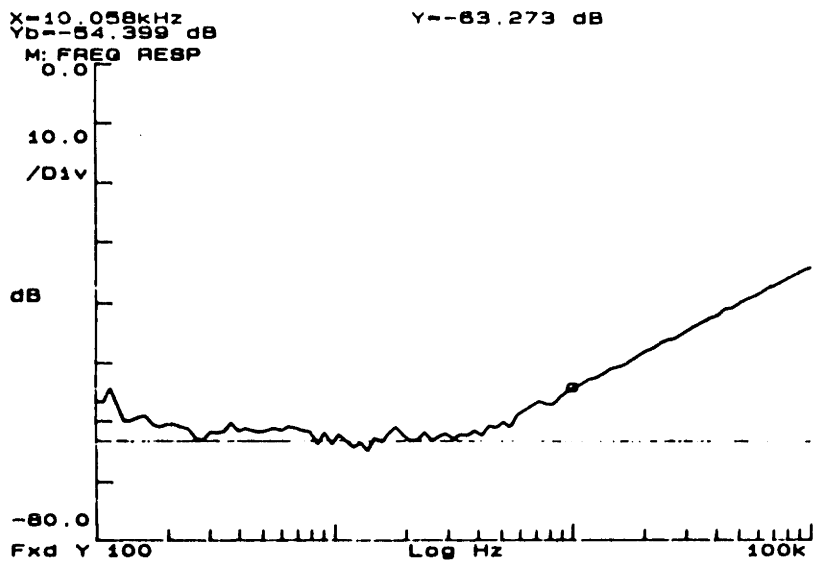

Figure 3.5. Local oscillator intensity noise cancellation with dual balanced detectors. More than 60 dB of cancellation is obtained at a modulation frequency of 10 kHz.

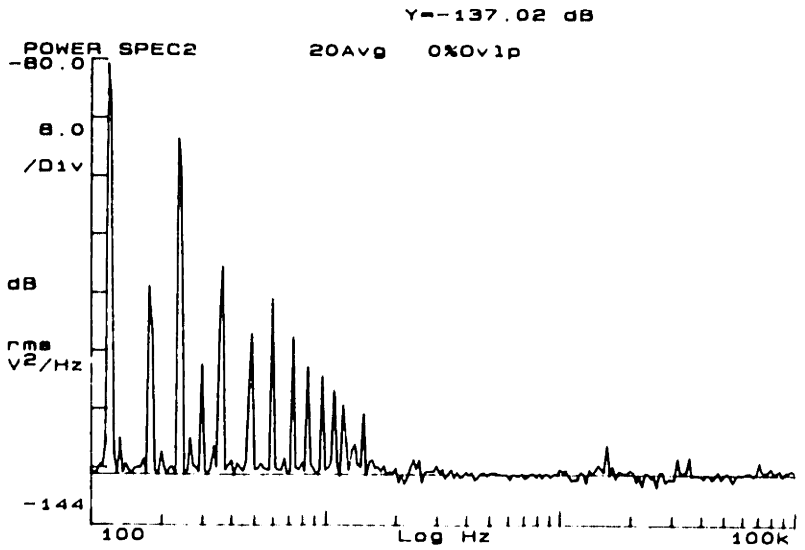

Figure 3.6. Thermal noise spectral density of the transimpedance amplifier. The measured density is predicted by $4kTR = -138$ dB V^2/Hz.

The thermal noise in the system is dominated by the thermal noise due to the large feedback resistance in the amplifier. The noise power spectrum for the transimpedance amplifier was measured by plotting the output voltage on a spectrum analyzer with both detectors covered, shown in Fig. 3.6. The white component of the noise is measured at -137 dB V^2/Hz, which corresponds to the predicted thermal noise density $4kTR = -138$ dB V^2/Hz for $R = 1\ M\Omega$ and $T = 300°\ K$. Note that the spectrum analyzer measures the power spectral density for both positive and negative frequencies simultaneously so that the theoretical expressions for the spectral density derived in earlier sections must be multiplied by two to compare with actual measurements ($S^+(\omega) = 2S(\omega)$).

An ideal detection system will only be limited by the shot noise arising from random intensity and voltage fluctuations arising due to the quantization of light and charge. To achieve this shot noise limit, the system parameters must be chosen so that the shot noise spectral density overwhelms the noise spectral density from other sources in the detection bandwidth of interest.

First the phase modulation frequency, or detection band is selected so that it is above the predominant, low frequency $1/f$ noise in the system. A modulation frequency of 10 kHz was chosen as the highest frequency at which the balanced detectors could achieve adequate cancellation.

The low-frequency s-domain transfer function between the input current $I(s)$ and output voltage $V(s)$ of the transimpedance amplifier is just $H(s) = V(s)/I(s) = R$. Thus, using Eq. (3.60) and noting that different noise processes are statistically independent, the positive frequency power spectral density $S_v^+(\omega)$ of the noise voltage at the output of the transimpedance amplifier is equal to R^2 times the noise current input spectral density, or

$$\begin{aligned} S_v^+(\omega) &= 2e\langle i\rangle R^2 + 2e\gamma\langle i\rangle^2 R^2 + 4kTR \\ &= 2e\langle v\rangle R + 2e\gamma\langle v\rangle^2 + 4kTR \end{aligned} \tag{3.90}$$

where the terms represent, from left to right, the contributions from shot noise, excess intensity noise, and thermal noise, respectively. $\langle v\rangle$ is the mean voltage output of the amplifier, and in the limit where the reference arm light intensity dominates the weak light emerging from the sample, $\langle v\rangle$ is proportional to the reference arm power. Note that

for a dual detector system, $\langle v \rangle$ equals the sum of the magnitudes of the DC voltages at each detector separately.

The transimpedance gain R and the reference arm power $\langle v \rangle$ are chosen so the shot noise term in Eq. (3.90) is greater than the excess intensity noise and thermal noise. To ensure that the shot noise eclipses the thermal noise, we require $2e\langle v \rangle R > 4kTR$, or

$$\langle v \rangle > \frac{2kT}{e} \approx 0.05 \text{ V} \quad \text{for } T = 300^\circ \text{ K}. \tag{3.91}$$

This limit defines the absolute minimum reference arm power. The gain R must be chosen so that the shot noise dominates the excess intensity noise, or

$$R > \gamma \langle v \rangle. \tag{3.92}$$

The upper limit on R is determined by the transimpedance amplifier stability and roll-off frequency in Eq. (3.89). Ideally, the gain R should be as small as possible and the reference arm power $\langle v \rangle$ should be as large as possible so that the resulting light intensity will be strong enough to fall in the linear region of the detectors, and so that the reference arm power will dominate the light emerging from the sample.

In practice, to construct the detector circuit, R is chosen before $\langle v \rangle$. Since the excess intensity noise parameter γ is usually unknown, given R, the optimal value of $\langle v \rangle$ must be determined experimentally. The procedure is to successively attenuate the reference arm power $\langle v \rangle$ and examine the noise spectral density on the spectrum analyzer until the white component equals the predicted shot noise value $2e\langle v \rangle R$. Attenuation of the reference arm intensity reduces the excess intensity noise linearly with decreasing signal power $\langle v \rangle^2$, but only affects the shot noise component as the square root. If $\langle v \rangle$ needs to be decreased below the thermal noise limit of 0.05 V, then the amplifier gain R should be increased, and the procedure repeated.

Figure 3.7 shows the measured noise spectral density at the output of the transimpedance amplifier for $R = 1$ MΩ and the reference arm power optimally attenuated so that the DC voltage from each detector separately is $\langle v \rangle = 0.2$ V. The $1/f$ component of the noise is negligible above 2 kHz. The white component of the spectral density occurs at -127.5 dB V^2/Hz, which is 1.5 dB above the shot noise level of $2e\langle v \rangle R = -129$ dB V^2/Hz. The detection is significantly worse if only a single detector is employed (Fig. 3.8). For a single detector, the spectrum is dominated by local

oscillator and $1/f$ noise, so that at the detection band of interest (10 kHz), the noise level is -108 dB V^2/Hz and more than 20 dB above the shot noise value.

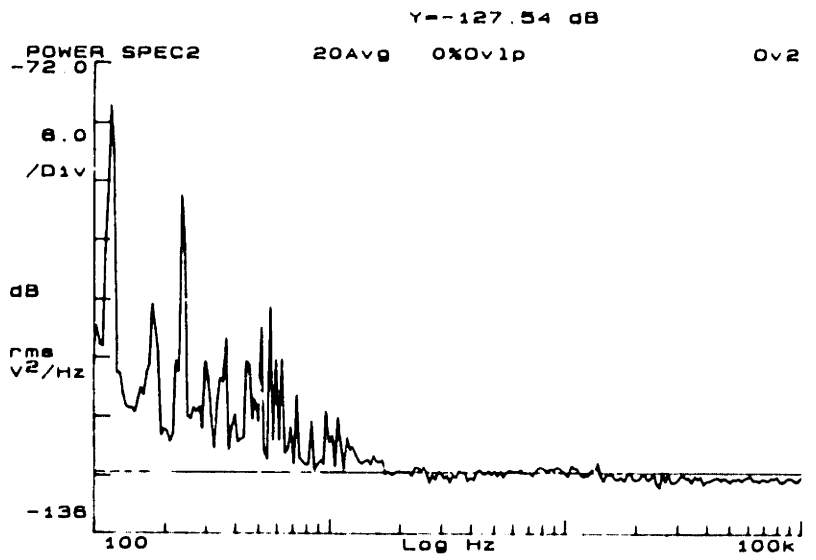

Figure 3.7. Shot noise and $1/f$ noise spectral density with dual balanced detection. At the detection band of 10 kHz, the system is within 1.5 dB of the predicted shot noise limit $2e\langle v\rangle R = -129$ dB V^2/Hz.

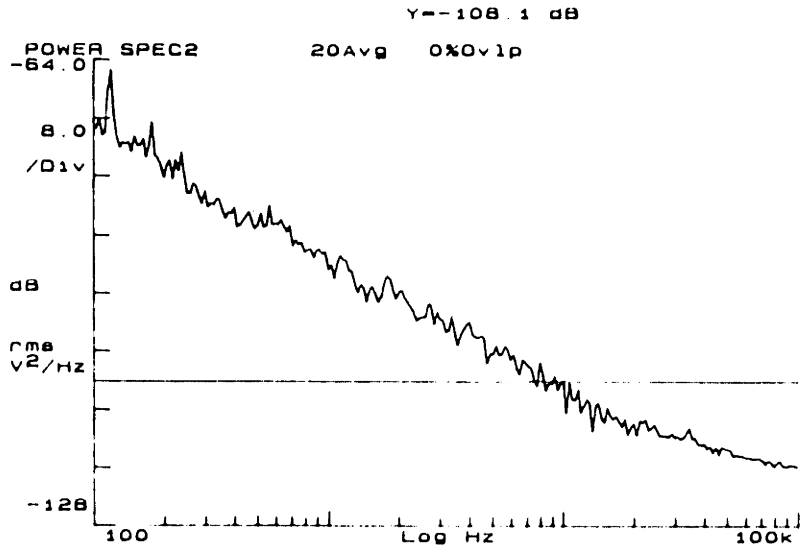

Figure 3.8. Local oscillator noise without dual balanced detection. The noise spectral density at 10 kHz is -108 dB V^2/Hzwhich is more than 20 dB above the shot noise density of $2e\langle v\rangle R = -129$ dB V^2/Hz.

3.5.8 System Dynamic Range

The dynamic range, or signal-to-noise ratio (*SNR*) for any system is defined simply as the maximum signal power P_{signal} divided by the mean noise power P_{noise}. From Eq. (3.56), the mean power of a noise process $n(t)$ equals the integral of its power spectral density $S_n(\omega)$ over all frequencies, or equivalently the noise process variance $\mathrm{var}\{n(t)\}$, so that the *SNR* is given by

$$SNR = \frac{P_{signal}}{P_{noise}} = \frac{P_{signal}}{\int_{-\infty}^{\infty} S_n(\omega)\frac{d\omega}{2\pi}} = \frac{P_{signal}}{\mathrm{var}\{n(t)\}}. \tag{3.93}$$

For the coherence-gated transillumination system, the maximum electrical signal power is equal to the square of the photocurrent signal evaluated at the peak of the coherence-gate cross-correlation in Eq. (3.23). To simplify the expression for the signal power, we neglect the degradations in signal amplitude caused by group velocity dispersion (Eq. (3.29)), self-phase modulation (Eq. (3.41)), piezoelectric phase modulation and lock-in detection (Eq. (3.49)), and quadrature fluctuations (Sec. 3.4.2), although these effects may considered later by reducing the *SNR* by the respective multiplicative degradation factors (squared). The maximum signal power P_{signal} for the ideal case is obtained for a sample which does not attenuate transmitted light, and is given by

$$P_{signal} = \left(\frac{\eta e}{\hbar\omega}\right)^2 R^2 P_S P_R \tag{3.94}$$

where η is the detector quantum efficiency, ω is the optical frequency, R is the transimpedance amplifier gain, P_S is the time-averaged optical power incident on the sample, and P_R is the time-averaged optical power in the reference arm.

The mean noise power P_{noise} depends on the noise spectral density $S_n(\omega)$ at the output of the system and is function of the detection bandwidth. After the interference signal is detected and amplified by the transimpedance amplifier, the signal is demodulated and low-pass filtered by the lock-in amplifier. The demodulation and filtering action may be described by a linear system $H(s)$. If the noise spectral density at the output of the transimpedance amplifier is $S_v(\omega)$ (Eq. (3.90)), then the total system noise spectral density $S_n(\omega)$ is, from Eq. (3.60),

$$S_n(\omega) = |H(j\omega)|^2 S_v(\omega). \tag{3.95}$$

For a shot-noise limited system (Sec. 3.5.7), $S_v(\omega)$ is white over the frequency range of $H(j\omega)$, and the noise power may be written

$$P_{noise} = \int_{-\infty}^{\infty} |H(j\omega)|^2 S_v(\omega) \frac{d\omega}{2\pi} = S_v^+(\omega) \cdot NEB \tag{3.96}$$

recalling that $S_v^+(\omega) = 2S_v(\omega)$, and defining the noise equivalent bandwidth (NEB) as

$$NEB = \int_0^{\infty} |H(j\omega)|^2 \frac{d\omega}{2\pi}. \tag{3.97}$$

The noise power is proportional to NEB, which is a measure of the width of the detection bandwidth.

Since the system has been designed for shot noise limited detection as in Sec. 3.5.7, the main contribution to $S_v^+(\omega)$ is the shot noise voltage spectral density $2e\langle i \rangle R^2$, where the mean current $\langle i \rangle$ is proportional to the reference arm power P_R. Inserting Eqs. (3.96) and (3.94) into Eq. (3.93), the signal-to-noise ratio becomes

$$SNR = \left(\frac{\eta}{\hbar\omega}\right) \frac{P_S}{2 \cdot NEB}. \tag{3.98}$$

In the shot noise limit, the dynamic range does not depend on the reference arm power P_R. Equation (3.98) shows that the instrument sensitivity depends linearly on the power P_S incident on the sample, and inversely on the detection bandwidth NEB. For the transillumination system, the detection bandwidth is essentially the bandwidth of the final low-pass filtering operation after demodulation.

3.5.9 Acquisition Speed, Dynamic Range, and Spatial Resolution

The required NEB of the detection system is determined by the trade-off between acquisition speed and spatial resolution. Raster scanning the sample produces a time-varying signal waveform. The maximum bandwidth of this waveform, determined by the scanning velocity and spatial resolution, defines the minimum cut-off frequency of the final low-pass filtering operation.

Suppose that the final low-pass operation is an ideal, rectangular low-pass filter with cutoff frequency f_c. The impulse response $h(t)$ of such a filter is given by

$$h(t) = \frac{\sin(2\pi f_c t)}{\pi t}. \tag{3.99}$$

The full width of the main lobe of $h(t)$ is $\Delta t = 1/f_c$ and defines the temporal resolution of the low-pass filter. In other words, impulses in time at the input of the low-pass filter may be localized at the output of the filter if they are separated by about Δt seconds. The spatial resolution Δx of the system is related to the temporal resolution Δt of the filter through the scanning velocity v_s:

$$\Delta x = v_s \Delta t = \frac{v_s}{f_c}. \tag{3.100}$$

Given a desired spatial resolution and scanning velocity, one can compute the necessary filter bandwidth through the relation $f_c = v_s/\Delta x$.

To accurately digitize the signal, sampling must occur at the Nyquist rate $2f_c$ to prevent aliasing. Thus, the required distance between samples is $\Delta d = \Delta x/2$, or half the spatial resolution.

The *NEB* of the ideal low-pass filter is just equal to f_c, so that the signal-to-noise ratio in Eq. (3.98) becomes

$$SNR = \left(\frac{\eta}{\hbar\omega}\right)\frac{P_S}{2}\frac{\Delta x}{v_s}. \tag{3.101}$$

Since the scanning velocity determines the total acquisition time, the dynamic range increases linearly with increasing acquisition time. The sensitivity also increases linearly with decreasing spatial resolution.

For the current system, the scanning velocity is limited by the two-dimensional translation stage to $v_s = 1$ mm / s. Since a spatial resolution of $\Delta x = 100$ μm is desired, the minimum low-pass filter bandwidth is $f_c = 10$ Hz. The interferometer path length phase is dithered at a low frequency to enable averaging over quadrature fluctuations, as described in Sec. 3.4.2. In order to average over 10 samples, the filter cut-off was increased by a factor of 10 to $f_c = 100$ Hz so that the filter could respond to signal variations induced by the phase dithering. Although the filter bandwidth was increased

by a factor or 10, the mean noise power was not affected because the 10 times signal averaging reduced the noise spectral density by a corresponding 10 times. Averaging the signal fluctuations, however, reduced the dynamic range by approximately 6 dB.

The actual dynamic range for these parameters was measured by placing neutral density filters in the transmission path and was 130 dB. The spatial resolution was determined by raster scanning an Air-force resolution chart (see Sec. 5.2.1), and was measured to be about 100 μm, as expected.

References

1. C. J. R. Sheppard and T. Wilson, "Image formation in confocal scanning microscopes," Optik **55**, 331-342 (1988).

2. C. J. R. Sheppard and T. Wilson, "Image formation in scanning microscopes with partially coherent source and detector," Opt. Acta **25**, 315-325 (1978).

3. M. Gu, C. J. R. Sheppard, and X. Gan, "Image formation in a fiber-optical confocal scanning microscope," J. Opt. Soc. Am. A **8**, 1755-1761 (1991).

4. T. Sawatari, "Optical Heterodyne Scanning Microscope," Appl. Opt. **12**, 2768-2772 (1973).

5. M. Toida, M. Kondo, T. Ichimura, and H. Inaba, "Experimental Verification of Image Detection in Highly Scattering Media Using Antenna Properties of Optical Heterodyne Microscope Scheme," Electron. Lett. **26**, 700-702 (1990).

6. M. Toida, M. Kondo, T. Ichimura, and H. Inaba, "Two-Dimensional Coherent Detection Imaging in Multiple Scattering Media Based on the Directional Resolution Capability of the Optical Heterodyne Method," Appl. Phys. B **52**, 391-394 (1991).

7. E. N. Leith, C. Chen, H. Chen, Y. Chen, J. Lopez, P.-C. Sun, and D. Dilworth, "Imaging through scattering media using spatial incoherence techniques," Opt. Lett. **16**, 1820-1822 (1991).

8. E. Leith, C. Chen, H. Chen, Y. Chen, D. Dilworth, J. Lopez, J. Rudd, P.-C. Sun, J. Valdmanis, and G. Vossler, "Imaging through scattering media with holography," J. Opt. Soc. Am. A **9**, 1148-1153 (1992).

9. G. P. Agrawal, *Nonlinear Fiber Optics*, Academic Press, New York (1989).

10. E. P. Ippen, C. V. Shank, and T. K. Gustafson, "Self-phase modulation of picosecond pulses in optical fibers," Appl. Phys. Lett. **24**, 190-192 (1974).

11. R. H. Stolen and C. Lin, "Self-phase modulation in silica optical fibers," Phys. Rev. A **17**, 1448-1453 (1978).

12. R. A. Fisher and W. K. Bischel, "Numerical studies of the interplay between self-phase modulation and dispersion for intense plane-wave laser pulses," J. Appl. Phys. **46**, 4921-4934 (1975).

13. W. J. Tomlinson, R. H. Stolen, and C. V. Shank, "Compression of optical pulses chirped by self-phase modulation in fibers," J. Opt. Soc. Am. B **1**, 139-149 (1984).

14. W. J. Tomlinson and W. J. Knox, "Limits of fiber-grating optical pulse compression," J. Opt. Soc. Am. B **4**, 1404-1411 (1987).

15. W. B. Davenport, Jr. and W. L. Root, *An Introduction to the Theory of Random Signals and Noise*, McGraw-Hill, New York (1958).

16. M. Schwartz, *Information, Transmission, Modulation, and Noise: A Unified Approach to Communication Systems, 3rd ed.*, McGraw-Hill, New York (1980).

17. A. Papoulis, *Probability, Random Variables, and Stochastic Processes, 2nd ed.*, McGraw-Hill, New York (1984).

18. R. Loudon, *The quantum theory of light, 2nd ed.*, Clarendon Press, Oxford (1983).

19. N. W. Ashcroft and N. D. Mermin, *Solid State Physics*, W. B. Saunders Co., Philadelphia (1976).

20. P. R. Gray and R. G. Meyer, *Analysis and Design of Integrated Circuits, 2nd ed.*, John Wiley & Sons, New York (1984).

21. A. W. Drake, *Fundamentals of Applied Probability Theory*, McGraw-Hill, New York (1967).

22. G. L. Abbas, V. W. S. Chan, and T. K. Yee, "A Dual-Detector Optical Heterodyne Receiver for Local Oscillator Noise Suprression," J. Lightwave Technol. **3**, 1110-1122 (1985).

Chapter 4

Coherence-Gated Light Scattering in Random Media

4.1 Introduction

The coherence-gated transillumination system is a useful tool for studying the coherent scattering properties of model scattering media and biological tissues. A scattering sample is inserted into the transmission arm of the interferometer. The spatially and phase coherent component of the scattered light emerging from the specimen is temporally profiled by plotting the magnitude of the interference signal versus the reference arm path length, or equivalent coherence-gate time delay.

Coherent scattering profiles have been obtained with the transillumination system for model scattering systems consisting of latex microsphere suspensions. Since the complete electromagnetic field solution for scattering from a uniform sphere is known, these studies permit correlation of analytically predicted scattering parameters with experimentally observed scattering profiles. Time-resolved coherent scattering from biological specimens has also been analyzed, although tissue inhomogeneities make these profiles more difficult to interpret. These biological profiles may be compared to the model scattering system to potentially establish or confirm tissue optical characteristics.

This chapter will present a brief introduction to Mie theory and radiative transport theory for scattering from uniform spheres and random distributions of particles respectively. Then, some previous results involving time-resolved incoherent scattering

will be reviewed. These results will then be compared to coherent scattering experiments performed with the coherence-gated transillumination system.

4.2 Scattering Theory for Spherical Particles

Mie scattering theory is an exact solution for the scattering of a plane electromagnetic wave by a single, homogenous, isotropic sphere. Since the theory is based on a rigorous solution of Maxwell's equations, it includes the effects of polarization, interference, and diffraction. This section will define the amplitude scattering matrix, a convenient formalism for describing the scattered field radiating from an arbitrary particle, and the scattering cross-section and anisotropy parameters. Rayleigh scattering will be reviewed and placed in the scattering matrix formalism. Finally, numerical solutions describing Mie scattering from various sized spheres will be presented.

4.2.1 Amplitude Scattering Matrix[1]

The amplitude scattering matrix $\bar{\mathbf{S}}$ relates the incident to the scattered field in the far field approximation. Consider a scattering particle located at the origin with a plane wave $\mathbf{E}_i$ incident in the $\hat{\mathbf{z}}$ direction (Fig. 4.1). In the far field, regardless of the shape of the particle, the scattered wave $\mathbf{E}_s$ is approximately transverse and has the form of a time-harmonic spherical wave[2]:

$$\mathbf{E}_s(r,\theta,\phi) \approx \mathbf{f}(\theta,\phi)\frac{e^{-jkr}}{r} \tag{4.1}$$

where $\mathbf{f}(\theta,\phi)$ is a complex vector representing the amplitude, phase, and polarization of the scattered field propagating in the direction defined by the scattering angle θ and the azimuthal angle ϕ (which are the normal spherical coordinates).

The incident and scattered fields can each be split into two orthogonal polarization components perpendicular and parallel to the scattering plane, defined as the plane containing the $\mathbf{k}$ vectors of the incident and scattered waves. Then, the vector function $\mathbf{f}(\theta,\phi)$ becomes a scalar 2 x 2 complex matrix $\bar{\mathbf{S}}(\theta,\phi)$. The relation between the complex amplitudes of the incident and scattered fields may be rewritten as

$$\begin{bmatrix} E_{s\parallel} \\ E_{s\perp} \end{bmatrix} = \frac{e^{-jkr}}{r} \bar{\mathrm{S}}(\theta,\phi) \cdot \begin{bmatrix} E_{i\parallel} \\ E_{i\perp} \end{bmatrix} \tag{4.2}$$

where

$$\bar{\mathrm{S}}(\theta,\phi) = \begin{bmatrix} S_{11} & S_{12} \\ S_{21} & S_{22} \end{bmatrix} \tag{4.3}$$

and the subscripts $\parallel$ and $\perp$ denote the parallel and perpendicular polarization components

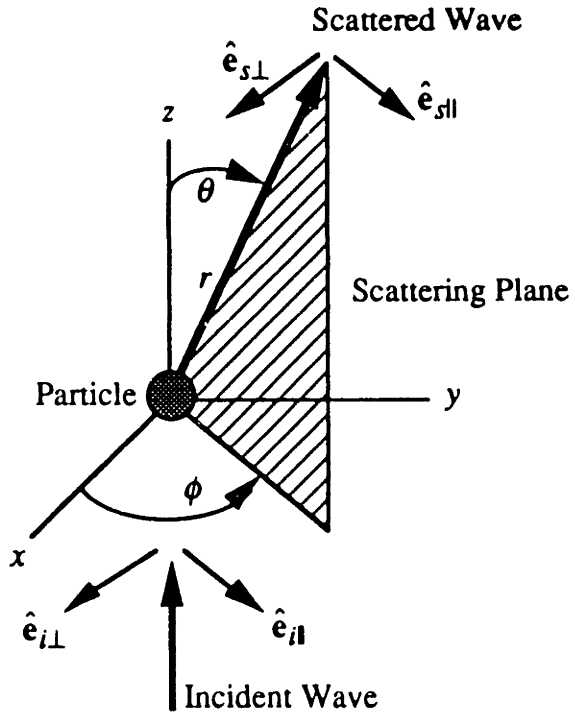

Figure 4.1. Geometry of the general scattering problem. The incident wave propagates in the $\hat{z}$ direction. θ is the scattering angle and ϕ is the azimuthal angle. $\hat{e}_{i\parallel}$, $\hat{e}_{i\perp}$, $\hat{e}_{s\parallel}$ and $\hat{e}_{s\perp}$ define the unit vectors for the parallel and perpendicular polarizations of the incident and scattered waves.

respectively of the incident or scattered field. For clarity this definition is different from the scattering matrix presented in Ref. 1. The unit vectors in the parallel and perpendicular directions for both the incident and scattered waves are shown in Fig. 4.1.

For spherical particles, symmetry simplifies the amplitude scattering matrix so that the off-diagonal matrix elements are nonexistent and $\bar{\mathbf{S}} = \bar{\mathbf{S}}(\theta)$ is a function of the scattering angle θ alone:

$$\bar{\mathbf{S}}(\theta) = \begin{bmatrix} S_{11}(\theta) & 0 \\ 0 & S_{22}(\theta) \end{bmatrix}. \tag{4.4}$$

4.2.2 Rayleigh Scattering[1-3]

Rayleigh scattering is a special case of Mie theory, giving an analytical solution for the scattered field valid for particles with dimensions much smaller than a wavelength. In the Rayleigh limit, the incident electric field is assumed to have no variation across the dielectric sphere. The incident field induces a time-harmonic dipole moment in the particle, which consequently radiates a scattered field analogous to a classical Hertzian dipole.

The electro-quasistatic dipole moment $\mathbf{p}$ for a dielectric sphere of volume V experiencing a constant electric field $\mathbf{E}_i$ is

$$\mathbf{p} = \varepsilon_m V \frac{\varepsilon_s - \varepsilon_m}{\varepsilon_s + 2\varepsilon_m} \mathbf{E}_i \tag{4.5}$$

where ε_s and ε_m are the dielectric constants of the sphere and the surrounding medium respectively. The dipole moment is proportional to the volume of the particle and the amplitude of the incident field. For the case of scattering, the incident field $\mathbf{E}_i$ is a plane wave with frequency ω, so that the scattered field $\mathbf{E}_s$ may be assumed to arise from the radiation pattern of an ideal oscillating dipole with moment $\mathbf{p}$. If $\mathbf{E}_i$ is polarized in the $\hat{\mathbf{z}}$ direction, then the expression for the scattered wave in the far field at a distance r and an angle θ from the particle is then

$$E_\theta = -\frac{k_m^2 p}{4\pi\varepsilon_m} \sin\theta \frac{e^{-jk_m r}}{r} \tag{4.6}$$

where k_m is the wavenumber in the medium and p is the magnitude of the induced dipole. The scattered field is symmetric with respect to the azimuthal angle ϕ and behaves like a plane wave polarized in the $\hat{\theta}$ direction propagating radially from the particle. The scattered field is always exactly in phase with the excitation since the induced dipole responds instantaneously to the incident field.

To derive the amplitude scattering matrix for a Rayleigh particle, we instead assume that the incident wave is propagating in the $\hat{\mathbf{z}}$ direction. Thus, the incident field must be transversely polarized in the x-y plane. In this geometry, the spherical coordinate θ is exactly the scattering angle. The scattering matrix accounts for the polarization of the incident and scattered waves by the division into components perpendicular and parallel to the scattering plane. For Rayleigh particles, the scattering matrix $\bar{\mathrm{S}}(\theta,\phi)$ is

$$\bar{\mathrm{S}}(\theta,\phi) = \frac{k_m^2}{4\pi}\frac{\varepsilon_s - \varepsilon_m}{\varepsilon_s + 2\varepsilon_m} V \begin{bmatrix} \cos\theta & 0 \\ 0 & 1 \end{bmatrix}. \tag{4.7}$$

The polarization component parallel to the scattering plane has a $\cos\theta$ dependence on the scattering angle, while scattering of the perpendicular polarization is completely isotropic. As expected for a spherical particle, $\bar{\mathrm{S}}(\theta,\phi)$ is symmetric with respect to the azimuthal angle ϕ, and its off-diagonal matrix elements vanish.

The total scattering cross-section σ_s is defined as the ratio of the total scattered power divided by the incident intensity and has units of area. For Rayleigh scattering,

$$\sigma_s = \frac{1}{6\pi}\left(\frac{\varepsilon_s - \varepsilon_m}{\varepsilon_s + 2\varepsilon_m}\right)^2 V^2 k_m^4 \tag{4.8}$$

showing that the scattered power is proportional to the incident intensity and inversely proportional to the fourth power of the wavelength.

The average cosine of the scattering angle, or the anisotropy parameter g, is defined as

$$g = \langle\cos\theta\rangle = \frac{\int_{4\pi} |\mathrm{f}(\theta,\phi)|^2 \cos\theta \, d\Omega}{\int_{4\pi} |\mathrm{f}(\theta,\phi)|^2 \, d\Omega} \tag{4.9}$$

and is an indication of the proportion of forward or backward directed scattering by the particle. For isotropic, or symmetric scattering, $g \to 0$; for highly forward scattering, $g \to 1$; and for highly backscattering, $g \to -1$. The scattering for Rayleigh particles is isotropic in the perpendicular polarization and symmetric about 90° for the parallel polarization, so $g = 0$.

4.2.3 Mie Scattering Theory[1,3,4]

The general Mie solution for scattering from a spherical particle of arbitrary size is difficult and requires a series solution. The derivation will not be described here. However, Ref. 1, Appendix A provides a useful FORTRAN program for numerically evaluating the relevant scattering coefficients given the indices of refraction of the sphere and the surrounding medium, the sphere diameter, and the incident wavelength.

Once the amplitude scattering matrix has been obtained, the cross-section σ_s may be calculated from the matrix components for a general spherical particle as follows:

$$\begin{aligned}\sigma_s &= \int_{4\pi} \left(|S_{11}|^2 + |S_{22}|^2\right) d\Omega \\ &= \pi \int_{-1}^{1} \left(|S_{11}(\theta)|^2 + |S_{22}(\theta)|^2\right) d(\cos\theta)\end{aligned} \tag{4.10}$$

Similarly, the anisotropy parameter $g = \langle \cos\theta \rangle$ is given by

$$\begin{aligned}g &= \frac{1}{\sigma_s} \int_{4\pi} \left(|S_{11}|^2 + |S_{22}|^2\right) \cos\theta \, d\Omega \\ &= \frac{\pi}{\sigma_s} \int_{-1}^{1} \left(|S_{11}(\theta)|^2 + |S_{22}(\theta)|^2\right) \cos\theta \, d(\cos\theta)\end{aligned} \tag{4.11}$$

For Rayleigh particles, these expressions reduce to the results given in Sec. 4.2.2.

Figures 4.2, 4.3, and 4.4 plot the Mie theory solution for 100 nm, 1 μm, and 10 μm latex particles suspended in water illuminated by an incident field at $\lambda = 830$ nm. The amplitude and phase of the perpendicular (S_{22}) and parallel (S_{11}) polarization components (with respect to the scattering plane) of the amplitude scattering matrix are plotted versus the scattering angle θ. The components of the scattering matrix correspond to the normalized amplitude of the scattered field as a function of scattering angle. For the 100 nm particles in the Rayleigh limit (Fig. 4.2), the numerical Mie theory solution closely corresponds to the analytical expressions obtained in Sec. 4.2.2. The anisotropy $g = 0.066$, and the cross-section $\sigma_s = 2.0 \times 10^{-13}$ cm^2. The scattering appears isotropic, with very little phase variation with scattering angle. For 1 μm particles with diameter on the order a wavelength (Fig. 4.3), the scattering is predominantly forward directed ($g = 0.960$) and the cross-section is significantly larger

($\sigma_s = 1.4 \times 10^{-8}$ cm^2). The phase of the scattered field varies approximately 45° over the scattering angles corresponding to the forward scattering lobe. Finally, for 10 μm particles with diameter much greater than a wavelength (Fig. 4.4), the scattering is very highly forward directed ($g = 0.998$), and the cross-section has increased to $\sigma_s = 1.5 \times 10^{-6}$ cm^2. The phase of the scattered field varies rapidly with the scattering angle. Thus, as particle size increases, the scattering becomes increasingly forward directed, the cross-section increases so more power is scattered, and the phase of the scattered field varies increasingly more with the scattering angle.

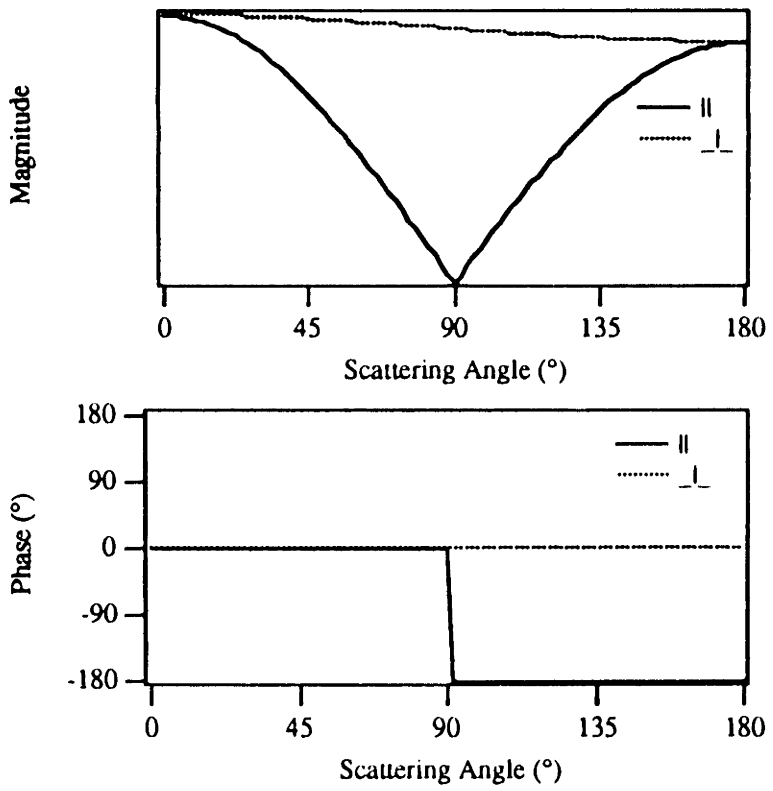

Figure 4.2. Mie scattering solution for a 100 nm diameter sphere ($g = 0.066$). (A) Amplitude of the parallel and perpendicular polarization components of the scattered field. (B) Phase of the parallel and perpendicular polarization components.

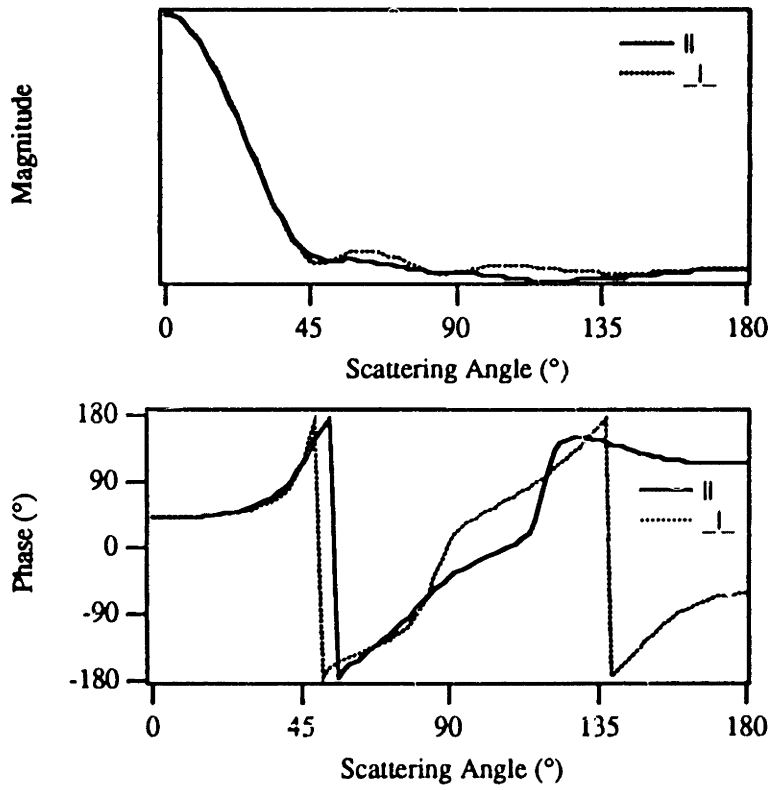

Figure 4.3. Mie scattering solution for a 1 μm diameter sphere (g = 0.960). (A) Amplitude of the parallel and perpendicular polarization components of the scattered field. (B) Phase of the parallel and perpendicular polarization components.

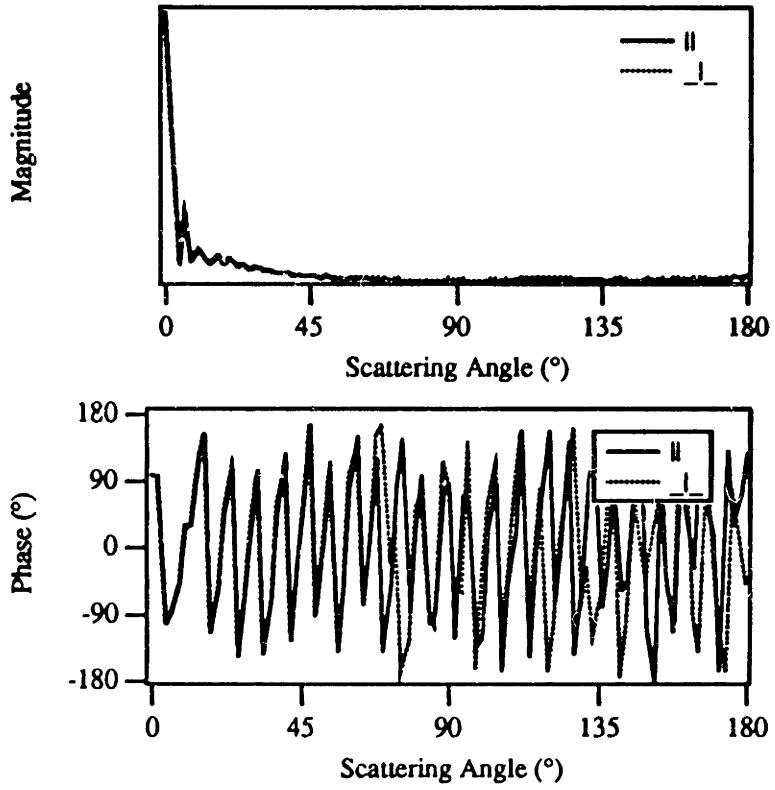

Figure 4.4. Mie scattering solution for a 10 μm diameter sphere ($g = 0.998$). (A) Amplitude of the parallel and perpendicular polarization components of the scattered field. (B) Phase of the parallel and perpendicular polarization components.

4.3 Radiative Transport Theory

An exact solution of Maxwell's equations is not feasible to describe scattering by biological tissue and other inhomogenous random media. Radiative transport theory is a heuristic approximation to the scattering problem and deals with the transport of energy through turbid media, rather than the propagation of electromagnetic fields. Since only the intensity enters the formulation, diffraction and interference effects are ignored. The theory also assumes that there is no interaction between successive scattering events.

This section will briefly describe the transport equation and its diffusion approximation, which is commonly used to model light propagation through biological specimens and describe tissue optical properties.

4.3.1 Boltzmann Transport Equation[4]

The transport equation used to describe light propagation through tissue relies on the fundamental quantity $I(\mathbf{r},\hat{\mathbf{s}})$ known as the specific intensity. The specific intensity has MKS units of W m^{-2} sr^{-1} and represents the intensity per unit steradian (solid angle) at the position $\mathbf{r}$ in the direction of the unit vector $\hat{\mathbf{s}}$. $I(\mathbf{r},\hat{\mathbf{s}})$ is decreased by absorption and scattering in the media, but increased by light that is scattered from other directions $\hat{\mathbf{s}}'$ into the direction $\hat{\mathbf{s}}$. The transport equation is the continuity relation which describes these interactions and is given by

$$\hat{\mathbf{s}}\cdot\nabla I(\mathbf{r},\hat{\mathbf{s}}) = -(\mu_a+\mu_s)I(\mathbf{r},\hat{\mathbf{s}}) + \mu_s\int_{4\pi} p(\hat{\mathbf{s}},\hat{\mathbf{s}}')I(\mathbf{r},\hat{\mathbf{s}}')d\Omega + S(\mathbf{r},\hat{\mathbf{s}}). \tag{4.12}$$

where μ_a is the absorption coefficient, μ_s is the scattering coefficient, $d\Omega$ is the differential solid angle in the direction of $\hat{\mathbf{s}}'$, $p(\hat{\mathbf{s}},\hat{\mathbf{s}}')$ is the normalized scattering phase function, and $S(\mathbf{r},\hat{\mathbf{s}})$ is the distributed source function. The transport equation may be intuitively understood as follows. The term $\hat{\mathbf{s}}\cdot\nabla I(\mathbf{r},\hat{\mathbf{s}})$ is the differential increase in the specific intensity in the direction $\hat{\mathbf{s}}$. The specific intensity is decreased by losses $\mu_a I(\mathbf{r},\hat{\mathbf{s}})$ and $\mu_s I(\mathbf{r},\hat{\mathbf{s}})$ due to absorption and scattering out of $\hat{\mathbf{s}}$, respectively. The term

$$\mu_s\int_{4\pi} p(\hat{\mathbf{s}},\hat{\mathbf{s}}')I(\mathbf{r},\hat{\mathbf{s}}')d\Omega \tag{4.13}$$

represents the increase in intensity due to scattering from directions $\hat{\mathbf{s}}'$ back into $\hat{\mathbf{s}}$, and $S(\mathbf{r},\hat{\mathbf{s}})$ describes any sources at $\mathbf{r}$ also emitting light into $\hat{\mathbf{s}}$.

The absorption and scattering coefficients μ_a and μ_s have units of inverse length and describe the attenuation of light due to absorption and scattering. One may view μ_a and μ_s as the probability of an absorption or scattering event occurring per unit distance of propagation. Thus, the intensity of light which has not been either scattered or absorbed after propagating a distance z through a random medium is reduced by a factor of

$$e^{-(\mu_a+\mu_s)z} \tag{4.14}$$

from the incident intensity. The mean-free-path (MFP) between an absorption or scattering event is given by either $1/\mu_a$ or $1/\mu_s$ respectively.

The phase function $p(\hat{\mathbf{s}},\hat{\mathbf{s}}')$ is the probability density function for scattering from $\hat{\mathbf{s}}$ into $\hat{\mathbf{s}}'$ and is normalized so that

$$\int_{4\pi} p(\hat{\mathbf{s}},\hat{\mathbf{s}}')d\Omega = 1. \tag{4.15}$$

If the scattering is symmetric about the direction $\hat{\mathbf{s}}$ of the specific intensity, then the phase function is only a function of the scattering angle θ between $\hat{\mathbf{s}}$ and $\hat{\mathbf{s}}'$. Usually the phase function is not known precisely, so its effects are lumped into a single anisotropy parameter, g, defined by

$$g = \int_{4\pi} p(\hat{\mathbf{s}},\hat{\mathbf{s}}')(\hat{\mathbf{s}}\cdot\hat{\mathbf{s}}')d\Omega = \int_{4\pi} p(\theta)\cos\theta d\Omega = \langle\cos\theta\rangle. \tag{4.16}$$

g is a convenient description of the anisotropy of a single scattering event and is analogous to the anisotropy parameter defined for Mie theory. Thus, for complete forward scattering $g \to 1$, for isotropic scattering $g \to 0$, and for complete backscattering $g \to -1$.

The radiant energy fluence rate $\varphi(\mathbf{r})$ at any point $\mathbf{r}$ is found by integrating the specific intensity over all 4π steradians and has units of W m^{-2}:

$$\varphi(\mathbf{r}) = \int_{4\pi} I(\mathbf{r},\hat{\mathbf{s}})d\Omega. \tag{4.17}$$

4.3.2 Diffusion Approximation[4-12]

In the multiple scattering limit, the transport equation may be simplified into the more tractable diffusion equation. The diffusion approximation is applicable far from tissue boundaries or sources when scattering dominates absorption.

The specific intensity $I(\mathbf{r},\hat{\mathbf{s}})$ may be divided into two components:

$$I(\mathbf{r},\hat{\mathbf{s}}) = I_c(\mathbf{r},\hat{\mathbf{s}}) + I_d(\mathbf{r},\hat{\mathbf{s}}). \tag{4.18}$$

$I_c(\mathbf{r},\hat{\mathbf{s}})$ represents all the light which has not yet interacted with the medium and exponentially attenuates with propagation distance according to Eq. (4.14). $I_d(\mathbf{r},\hat{\mathbf{s}})$ is the remaining scattered portion of the intensity containing light which has been scattered at

least once. If $I_d(\mathbf{r},\hat{\mathbf{s}})$ is approximated by the first two terms of a Taylor expansion, then the transport equation can be simplified to a steady-state diffusion equation:

$$-D\nabla^2\phi(\mathbf{r}) + \mu_a\phi(\mathbf{r}) = s(\mathbf{r}) \tag{4.19}$$

where $s(\mathbf{r})$ is a source term, $\phi(\mathbf{r})$ is the total diffuse fluence rate given by

$$\phi(\mathbf{r}) = \int_{4\pi} I_d(\mathbf{r},\hat{\mathbf{s}})d\Omega \tag{4.20}$$

and D is the diffusion coefficient:

$$D = \frac{1}{3[\mu_a + \mu_s(1-g)]}. \tag{4.21}$$

If the diffusion approximation is valid, and if one can only make measurements of $I_d(\mathbf{r},\hat{\mathbf{s}})$ and not $I_c(\mathbf{r},\hat{\mathbf{s}})$, then both the scattering coefficient μ_s and the anisotropy g cannot be independently determined. Only the combined factor $\mu_s(1-g)$ appears in the diffusion equation. Therefore, it is customary to define a reduced scattering coefficient μ' such that

$$\mu_s' = \mu_s(1-g). \tag{4.22}$$

Equation (4.22) highlights the fact that anisotropic scattering ($g \neq 0$) described by a scattering coefficient μ_s is indistinguishable from isotropic scattering ($g = 0$) described by a reduced scattering coefficient μ_s'. The diffuse intensity for an anisotropic scattering system may be analyzed as an equivalent isotropic system. A transport, or forward scattering mean-free-path may be defined such that

$$mfp_{forward} = \frac{1}{\mu_a + \mu_s(1-g)} \tag{4.23}$$

representing the mean-free-path between absorption and scattering events in the equivalent isotropic system.

The diffusion equation in Eq. (4.19) is a steady-state equation and valid only after equilibrium has been established. To analyze the transient dynamics of the fluence $\phi(\mathbf{r},t)$, a time-dependent term may be phenomenologically added to the expression:

$$-D\nabla^2\phi(\mathbf{r},t)+\frac{1}{c}\frac{\partial}{\partial t}\phi(\mathbf{r},t)+\mu_a\phi(\mathbf{r},t)=s(\mathbf{r},t). \tag{4.24}$$

Recall that the diffusion approximation is only valid in the multiple scattering limit, so that Eq. (4.24) only applies for times much greater than the mean-free-time between scattering events after all the sources have been turned on. Equation (4.24) has been solved analytically for a homogenous slab yielding expressions for the reflection and transmission of a short pulse[12].

4.3.3 Transport Coefficients for Mie Scatterers and Biological Tissue

The diffusion approximation of radiative transport theory reduces the properties of the scattering medium to three parameters: the absorption and scattering coefficients μ_a and μ_s, and the anisotropy parameter g. While these parameters clearly cannot describe many of the characteristics of a turbid media, they are standard, intuitive, and permit a quick comparison of the optical properties of various biological tissues. The transport parameters may be measured by many techniques, including steady-state and time-resolved optical reflectance and transmittance[13-16].

In general, μ_a, μ_s and g depend on the wavelength. For biological tissue, the wavelengths between 600 and 1300 nm are known as the "therapeutic window" because these wavelengths fall outside the absorption bands of hemoglobin, melanin, and water so that light has the deepest penetration into tissue. For light in the therapeutic window, typical values of the transport parameters are $\mu_a = 1\ \text{cm}^{-1}$, $\mu_s = 100\ \text{cm}^{-1}$, and $g = 0.9$. Thus, a typical tissue has a MFP between absorption events of 1 cm, and a MFP between scattering events of 100 μm, and a forward scattering MFP of 1 mm. For most tissue, scattering dominates absorption and each scattering event is highly forward directed. A good summary of tissue optical properties for various wavelengths and tissues is provided in Ref. 16.

The transport coefficients may also be related to the scattering amplitude matrix obtained from Mie theory for scattering from spheres. If the spheres are not absorbing then the absorption coefficient $\mu_a \approx 0$. If each scattering event is independent, then the scattering coefficient μ_s is proportional to the scattering cross section σ_s computed from Mie theory, and the number density N of particles in the medium:

$$\mu_s = N\sigma_s. \tag{4.25}$$

Thus, the mean-free-path between scattering events is $\mu_s^{-1} = (N\sigma_s)^{-1}$. The anisotropy parameter g is interchangeable between Mie and transport theory. As seen earlier, $g \rightarrow 0$ in the Rayleigh limit for small spheres. As the particle size increases, the scattering becomes more forward directed, and $g \rightarrow 1$.

Since scattering dominates absorption in tissue, suspensions of Mie scatterers provide a convenient and quantitative tissue phantom for scattering experiments. The anisotropy and number of scattering MFPs may be varied to approximate various tissue types by using spheres of different diameters and concentrations.

4.3.4 Monte Carlo Simulation[17-20]

Monte Carlo simulation is based on radiative transport theory and improves on the approximations in diffusion theory. Light distribution in tissue is calculated by probabalistically propagating individual photons during discrete units of time. For each time interval, a given photon has a probability of absorption or scatter defined by the transport coefficients μ_a and μ_s respectively. The direction of each scattering event, if one occurs, is determined by a random number weighted by an assumed phase function.

Unlike diffusion theory, Monte Carlo methods are applicable near tissue boundaries and sources, for all times, and for few scattering events. A complete phase function is assumed and not compressed into a single anisotropy parameter. However, the computational resources required by a Monte Carlo program can be considerable. Comparisons of diffusion theory with Monte Carlo simulation have shown that results are similar in the regime where diffusion theory is valid.

4.4 Review of Time-Resolved Incoherent Scattering Studies

Time-resolved studies of short laser pulses transmitted through turbid media have so far been limited to incoherent detection and time-gating techniques. Experiments show that a short pulse propagating through a scattering system emerges in two components: an early arriving, unscattered, or ballistic component, and a later arriving, multiply scattered and temporally broadened diffuse component.

Yoo and Alfano[21] have used an 8 ps resolution streak camera to temporally profile an 80 fs pulse propagating through a slab of random media consisting of various

sizes and concentrations of latex microspheres suspended in water. The concentration of microspheres was measured in the number of mean-free-paths (MFPs), computed from Mie theory, contained in the 1 cm thickness of scattering media. An early arriving ballistic component is observed for concentrations below 15 MFPs, while both a ballistic and later arriving and temporally broadened diffuse component appear for concentrations above 15 MFPs. The diffuse component overwhelms the ballistic component above 25 MFPs. The temporal displacement between the ballistic and diffuse peaks decreases as the size of the scatterers increases, from 20 ps for 330 nm diameter spheres, to 0 ps for 15.8 μm spheres. The diffuse pulse extends for hundreds of picoseconds for various diameters and concentrations. The authors observe that the temporal spread of the diffuse constituent is narrower for larger spheres and claim the effect is due to anisotropic scattering.

Kuga, *et. al.*[22] performed similar experiments with 109 nm, 481 nm, 2.02 μm and 5.7 μm diameter microsphere suspensions using a Kerr gate with 20 ps resolution. The authors observed broadening of the transmitted pulse for high sphere concentrations, but were unable to resolve separate ballistic and diffuse components due to the low temporal resolution of their system. The ballistic peak attenuated by $1/e$ for every scattering MFP, regardless of sphere size. The broadened, diffuse peaks attenuated approximately 10 times slower in the exponential, also fairly independent of particle diameter and anisotropy. A diffuse peak was not observed for 109 nm particles possibly due to geometric factors or low dynamic range, according to the authors.

Hebden[23] has recently repeated the above experiments with a 10 ps resolution streak camera and various concentrations of 1.3 μm microspheres. Diffuse light was observed for concentrations above 20 MFPs, and extended for more than 100 ps. The ballistic component attenuated exponentially with increasing numbers of scattering MFPs computed from Mie theory, as observed by Kuga, *et. al.*. Comparison with diffusion theory[12] revealed that the theory was a good predictor of diffuse pulse shape, and less accurate predicting attenuation or arrival time, although results are not reported.

Liu, *et. al.*[24] have analyzed the arrival time of the ballistic component propagating through various concentrations of 91 nm diameter microspheres with an 85 fs resolution second harmonic gate. The delay time increased with increasing microsphere concentration and was predicted accurately by assuming that the propagating laser pulse experienced the average refractive index of the microsphere suspension.

The temporal profile of the diffuse component has been investigated by Yoo, *et. al.*[11] A streak camera was used to analyze the diffuse light emerging from various size and concentration microsphere suspensions illuminated by 100 fs pulses. Diffusion theory was unable to predict the diffuse pulse shape when the concentration of microspheres was less than 10 forward scattering MFPs. The deviation from theory occurred mostly for early times (< 300 ps) and for anisotropically scattering particles, as expected.

4.5 Coherence-Gated Scattering in Microsphere Suspensions

Coherent scattering experiments were performed with suspensions of scattering microspheres of varying concentrations and diameters. A cuvette containing the microspheres suspended in water was placed in the transmission path of the coherence-gated transillumination system. Short pulses of light incident on the sample emerged temporally broadened due to multiple scattering events in the suspension. The magnitude of the coherent interference signal was recorded for the on-axis transmitted light while the reference path length was varied to progressively increase the coherence-gate delay. In this manner, a time-resolved plot of the directionally selected and phase coherent constituent of the transmitted pulse was obtained.

In the following sections, experimentally obtained coherence-gated scattering profiles for 1 μm, 10 μm and 100 nm diameter spheres will be presented and discussed. The implications of these profiles for time and spatially resolved transillumination imaging will be addressed in Ch. 5.

4.5.1 1 μm Microspheres

Figure 4.5 plots the normalized magnitude of the interference signal amplitude versus normalized coherence-gate delay for increasing concentrations of 1 μm diameter latex microspheres suspended in water ($g = 0.960$, $\sigma_s = 1.4 \times 10^{-8}$ cm^2). The 1 μm sphere diameter is on the order of the optical wavelength. The concentration is measured in the number of scattering mean-free-paths (MFPs), computed from Mie theory, contained in the $L = 5$ mm length cuvette. For readability, the signal amplitude for each concentration is normalized to the same peak height; however, the absolute magnitudes attenuate with increasing microsphere concentration. The normalized delay parameter is

defined as ct/nL, where t is the actual time delay, c/n is the speed of light in the medium, and L is the sample thickness. The concentration and delay parameter are both normalized to the sample length L and the plots may be easily extended to specimens of differing thicknesses.

In the transmission arm of the interferometer, light emerging from a single mode fiber (5 μm core diameter) was focused by a 12 mm focal length diode collimating objective onto the center of the cuvette containing the microspheres, located 11.4 cm away from the lens. The beam diameter was approximately 50 μm at the focus and 1.1 mm at the lens and the numerical aperture was 0.01. Light exiting the cuvette was symmetrically recoupled back into the single mode fiber interferometer by an identical objective lens. The full length confocal parameter of the focused beam was 5.6 mm, meaning that the beam diameter was approximately constant over the $L = 5$ mm length cuvette.

The incident optical power on the microsphere suspensions was 38 μW attenuated at the interferometer input for concentrations from 0 to 15 MFPs, and 50 mW for concentrations from 20 to 50 MFPs. The full-width-half-maximum (FWHM) of the time-resolved profile for light propagating through water (0 MFPs in Fig. 4.5) is 750 fs and defines the temporal resolution of the system for low incident optical powers. For 50 mW incident power, the temporal resolution is improved to 400 fs due to nonlinear self-phase modulation in the fiber optics (see Sec. 3.3.5).

According to Fig. 4.5, the phase coherent constituent of the transmitted light consists of two components: an early arriving ballistic component, and a later arriving, temporally broadened, diffuse component. The ballistic component arrives with almost no delay relative to water and represents completely unscattered light. The broadened diffuse component consists of the fraction of multiply scattered light which retains enough spatial and phase coherence to permit both confocal and coherent detection, respectively. The division into ballistic and diffuse components is qualitatively similar to earlier studies described above of time-resolved scattering with incoherent gating techniques. Here, however, the diffuse component displays a notably reduced temporal extent (1 normalized delay unit equals 22 ps for this geometry) due to loss of phase coherence and spatial rejection of scattered light. The peak of the diffuse component arrives later and broadens with increasing sphere concentration, similar to the results observed by Kuga, *et. al.*[22] for incoherent detection.

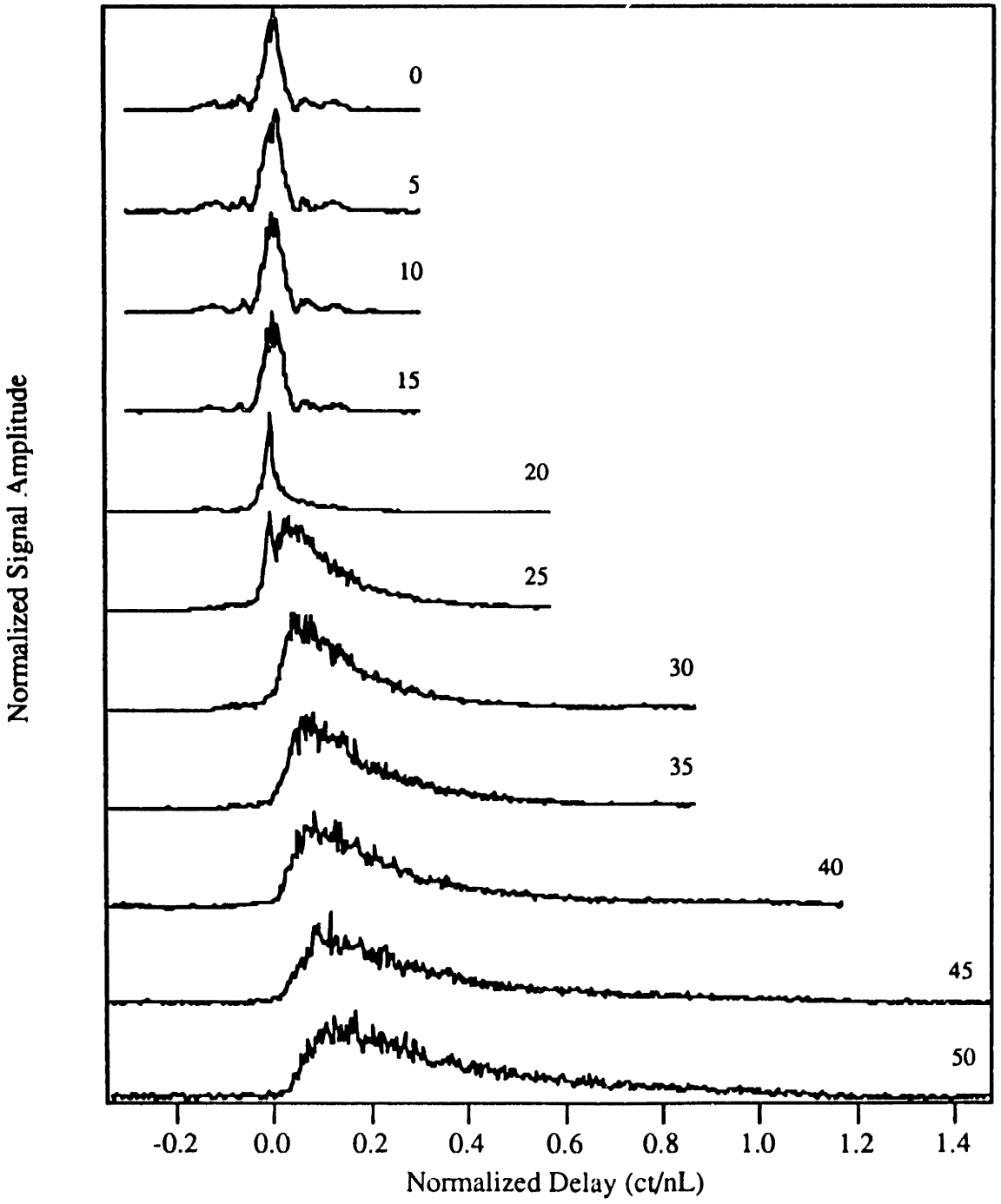

Figure 4.5. Coherence-gated scattering profiles for various concentrations of 1 μm microspheres ($g = 0.960$, $\sigma_s = 1.4 \times 10^{-8}$ cm^2) measured in the number of scattering MFPs contained in the $L = 5$ mm length cuvette. The normalized signal amplitude for each concentration is plotted versus the normalized delay parameter ct/nL, where t is the time delay, c/n is the speed of light in the medium, and L is the sample thickness.

Figure 4.6 displays the natural logarithm of the signal power for each of the coherence-gated profiles in Fig. 4.5 so that signal attenuation may be considered. The signal power is normalized to water (0 MFPs). The inset of Fig. 4.6 plots the attenuation of the ballistic and diffuse peak powers derived from the log plot for increasing numbers of scattering MFPs, or equivalent sample thickness. The ballistic component attenuates exactly by $1/e$ for every additional scattering MFP (least squares fit slope = -1.01), as expected assuming that the ballistic peak consists of completely unscattered light. The diffuse component is not visible below 20 MFPs. The ballistic and diffuse components have equal heights at about 25 MFPs, after which the ballistic peak is dominated by the diffuse peak. Yoo, *et. al.*[21] and Kuga, *et. al.*[22] also observed this transition from ballistic to diffuse dominated detected light to occur between 15 and 25 MFPs for a variety of particle sizes with incoherent detection. The inset also shows that the diffuse light attenuates about a factor of 10 more slowly (least squares slope = -0.115), than the ballistic light with increasing sphere concentration. This result is also consistent with the incoherent detection studies of Kuga, *et. al.*[22] Note that this logarithmic attenuation rate is almost a factor of 3 greater than the forward scattered attenuation rate of $-(1-g) = -0.04$ predicted from diffusion theory.

The amount of detected diffuse light presumably depends on a many factors, including the solid angle of detection and the temporal width of the coherence-gate. The experiments reported here were performed with the transmission beam focused through the sample. Since the confocal parameter was longer than the sample thickness, no difference in detected light was seen compared to experiments performed with a collimated beam. The detected diffuse power did increase linearly with increasing coherence-gate temporal width.

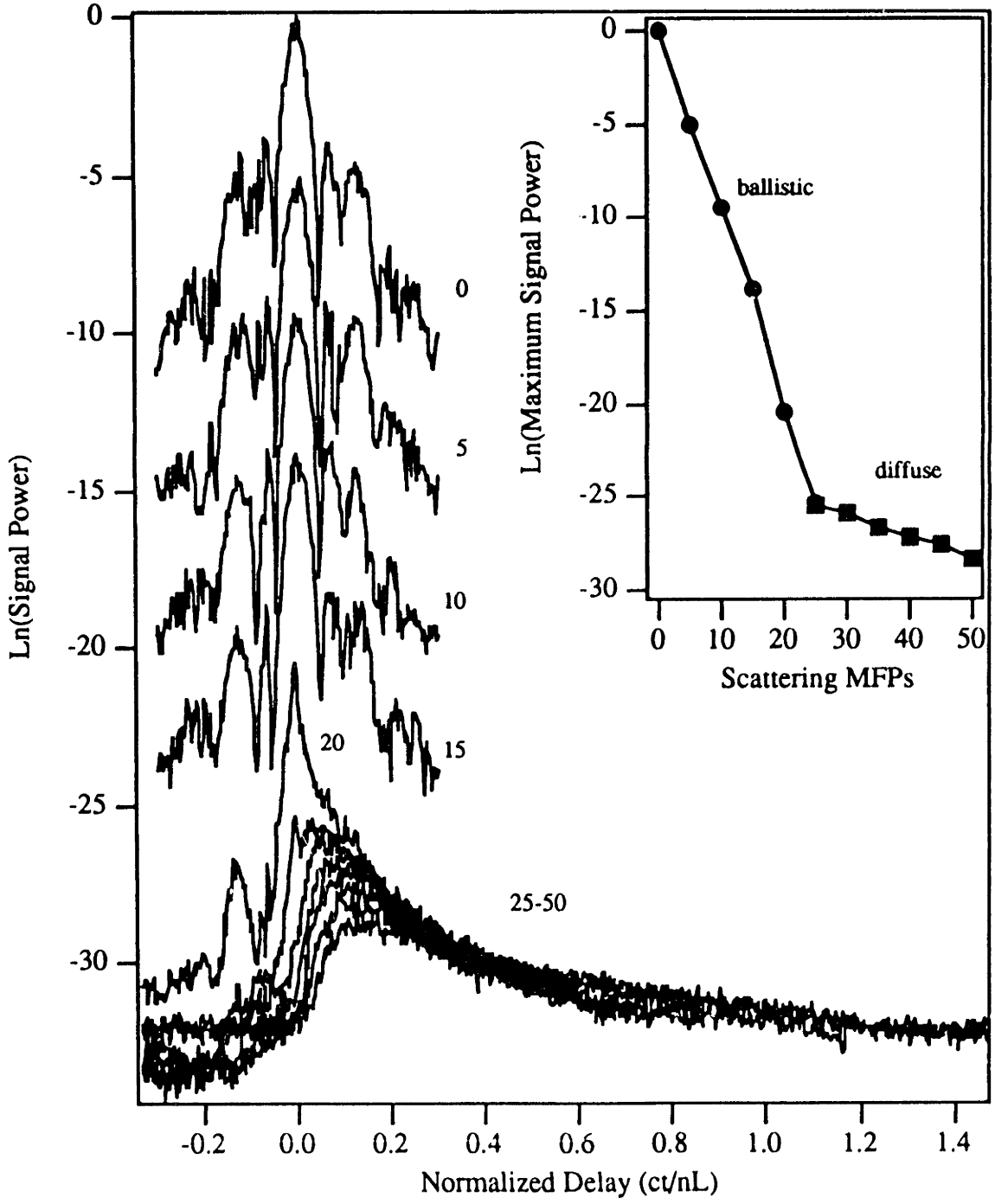

Figure 4.6. Coherence-gated scattering profiles for 1 μm microspheres displayed on a natural log scale. Inset: Attenuation of the ballistic and diffuse component peak signal power as a function of the number of scattering MFPs, or equivalent sample thickness.

4.5.2 10 μm Microspheres

Coherence-gated scattering profiles of 10 μm microspheres ($g = 0.998$, $\sigma_s = 1.5 \times 10^{-6}$ cm^2) show characteristics similar to the 1 μm particles discussed earlier. The linear scattering amplitude profiles, shown in Fig. 4.7, are qualitatively the same, with the transmitted light again separated into a ballistic and a diffuse component.

Figure 4.8 compares the normalized arrival time of the diffuse peak for 1 μm and 10 μm diameter spheres. For the 10 μm particles, the diffuse component arrives earlier and is almost coincident with the ballistic peak for 20 and 25 scattering MFPs. This effect is a manifestation of the very highly forward scattering nature of particles much larger than the optical wavelength. Since scattering events are very forward directed, the average diffuse path length through the sample decreases. For both sizes of particles, the diffuse components are increasingly delayed for increasing concentrations of scattering spheres, or equivalently, increasing sample thickness.

The highly forward scattering also causes a narrowing of the temporal extent of the diffuse component for the 10 μm compared to the 1 μm particles. Figure 4.9 details the normalized full-width-half-maximum (FWHM) $c\Delta t/nL$ of the diffuse peak for both 1 μm and 10 μm particles plotted versus the concentration of scattering microspheres. For both particle sizes the FWHM increases with increasing concentration (or sample thickness). However, the diffuse peak is always narrower for the 10 μm particles due to the predominantly forward scattering. Both the earlier arrival time (Fig. 4.8) and the reduction in temporal width (Fig. 4.9) for larger compared to smaller sized particles were observed by Yoo, *et. al.*[21] and Kuga, *et. al.*[22] with incoherent detection.

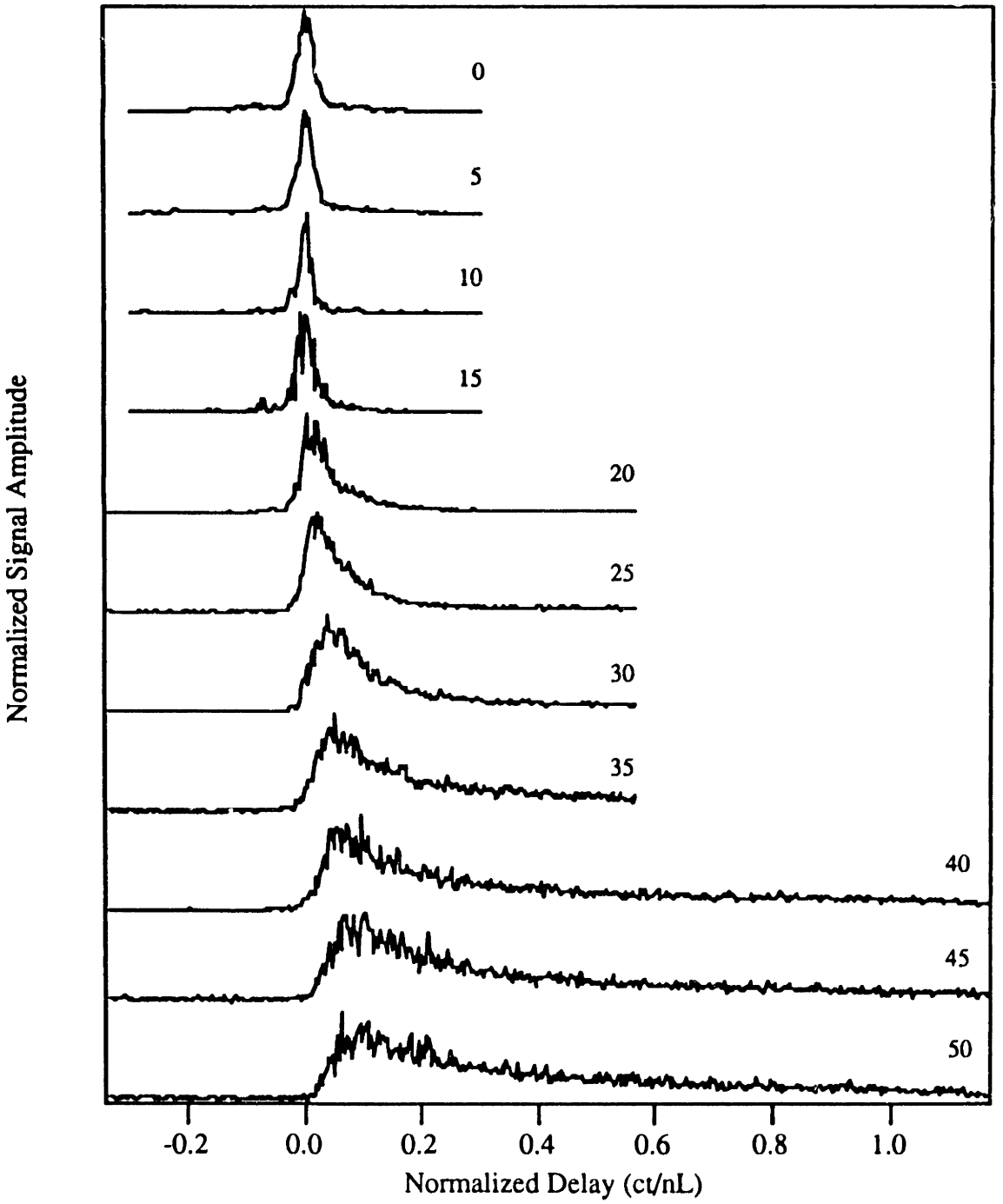

Figure 4.7. Coherence-gated scattering profiles for various concentrations of 10 μm microspheres ($g = 0.998$, $\sigma_s = 1.5 \times 10^{-6}$ cm^2) measured in the number of scattering MFPs contained in the $L = 5$ mm length cuvette. The normalized signal amplitude for each concentration is plotted versus the normalized delay parameter ct/nL, where t is the time delay, c/n is the speed of light in the medium, and L is the sample thickness.

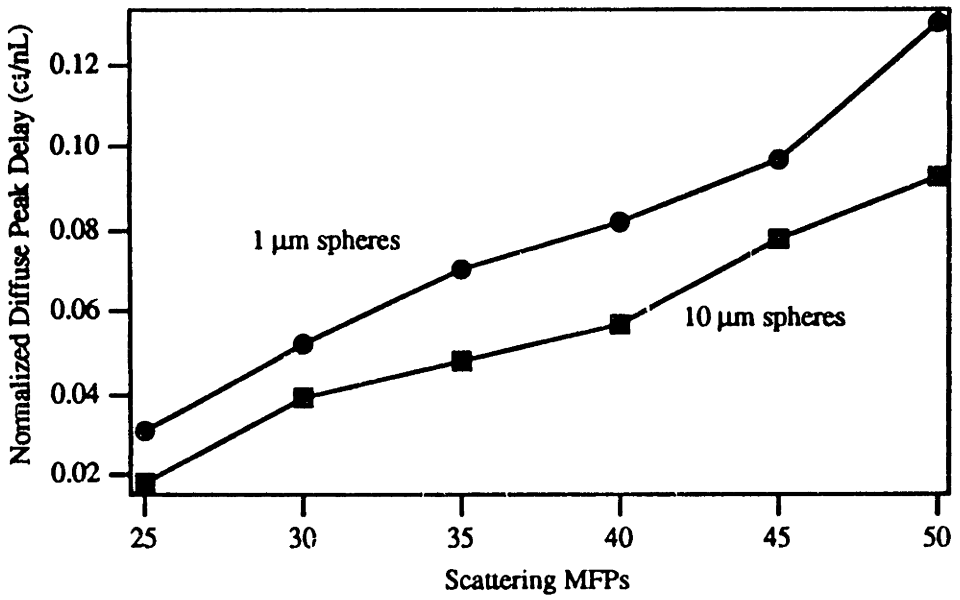

Figure 4.8. Normalized arrival time ct/nL of the diffuse peak for 1 μm and 10 μm particles, plotted versus the concentration of microspheres measured in the number of scattering MFPs. The cuvette length was $L = 5$ mm.

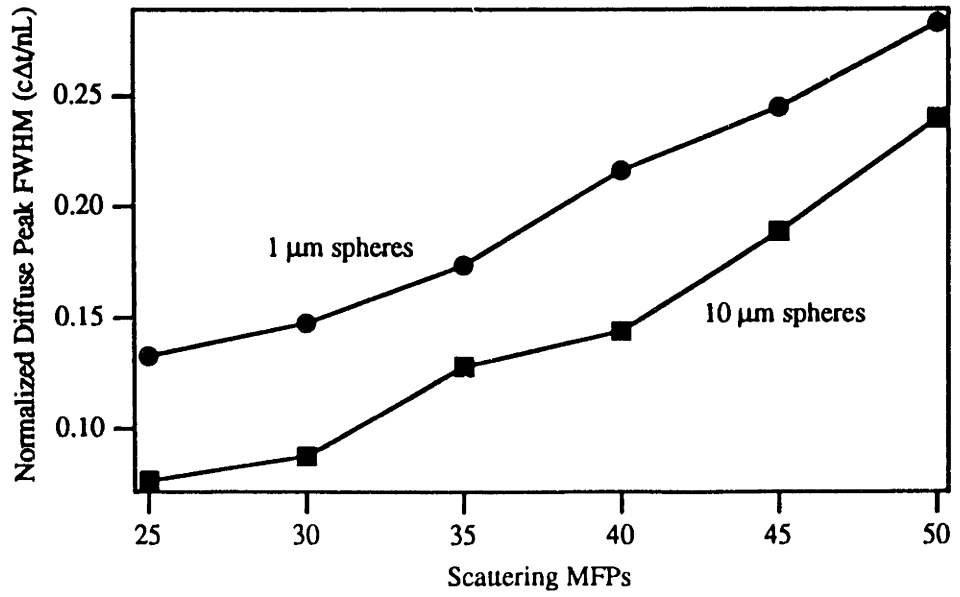

Figure 4.9. Normalized full-width-half-maximum (FWHM) $c\Delta t/nL$ of the diffuse peak for 1 and 10 μm diameter spheres as a function of scattering concentration measured in the number of MFPs. Δt is the actual temporal FWHM, c/n is the speed of light in the medium, and $L = 5$ mm is the cuvette length.

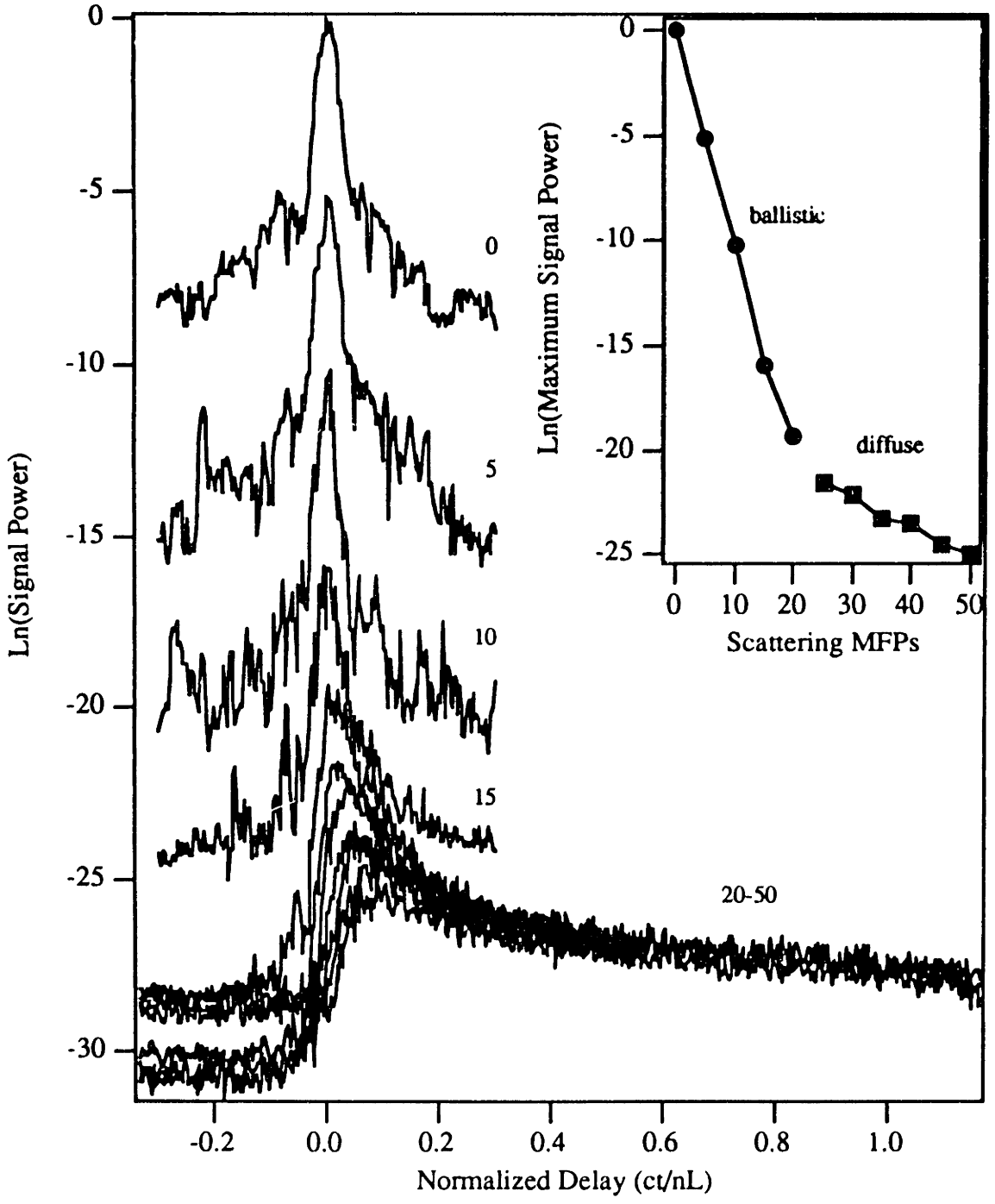

Figure 4.10. Coherence-gated scattering profiles for 10 μm microspheres displayed on a natural log scale. Inset: Attenuation of the ballistic and diffuse component peak signal power as a function of the number of scattering MFPs, or equivalent sample thickness.

The logarithmic plot of ballistic and diffuse component attenuation for 10 μm spheres is shown in Fig. 4.10. As expected, the ballistic light exponentially attenuates exactly with increasing scattering MFPs (least squares slope = -0.989). The diffuse component becomes predominant at about 20 MFPs, and attenuates about a factor of 7 more slowly than the ballistic component (slope = -0.140). Since the scattering is so highly forward directed for 10 μm compared to 1 μm spheres, one would expect that the diffuse component would attenuate more slowly for the 10 μm spheres. The reduced MFP is 500 times longer than the scattering MFP for 10 μm particles, and only 20 times longer for 1 μm particles. However, the experimental results show that the diffuse attenuation is approximately the same for both particles. The observed attenuation rate is about a factor of 500 more severe than the diffusion theory forward scattering attenuation rate of $-(1-g) = -0.002$. Kuga, *et. al.*[22] have reported similar results with incoherent detection. For 0.481 μm, 2.02 μm, and 5.7 μm particles, the diffuse logarithmic attenuation rate was always about a factor of 10 less rapid than the ballistic attenuation, and largely independent of the anisotropy g.

4.5.3 100 nm Microspheres

100 nm microspheres are in the Rayleigh scattering limit for particles small compared to a wavelength ($g = 0.066$, $\sigma_s = 2.0 \times 10^{-13}$ cm^2). Figure 4.11 plots the coherent scattering amplitude profiles for various concentrations of these microspheres versus normalized delay ct/nL. Only a ballistic peak is observed out to coherence-gate delays as large as 250 ps. The lack of a diffuse component is most likely due to the limited dynamic range of the system and the scattering geometry. A 4 cm length by 1 cm width cuvette was used to suspend the microspheres. Since the scattering is nearly isotropic, a large proportion of the diffuse light probably escaped through the cuvette edges and remained undetected by the system. The minimum cuvette length was constrained because the concentration of microspheres could not be so dense that multiple particles existed in a cubic wavelength. This constraint ensures that successive scattering events are noninteracting.

The expanded time scale in Fig. 4.11 clearly shows the narrowing of the coherence-gate temporal width due to nonlinear self-phase modulation. Concentrations of microspheres ranging from 0-10 MFPs were profiled with 40 μW incident power, while 46 mW was incident on concentrations from 15-30 MFPs. The arrival time of the

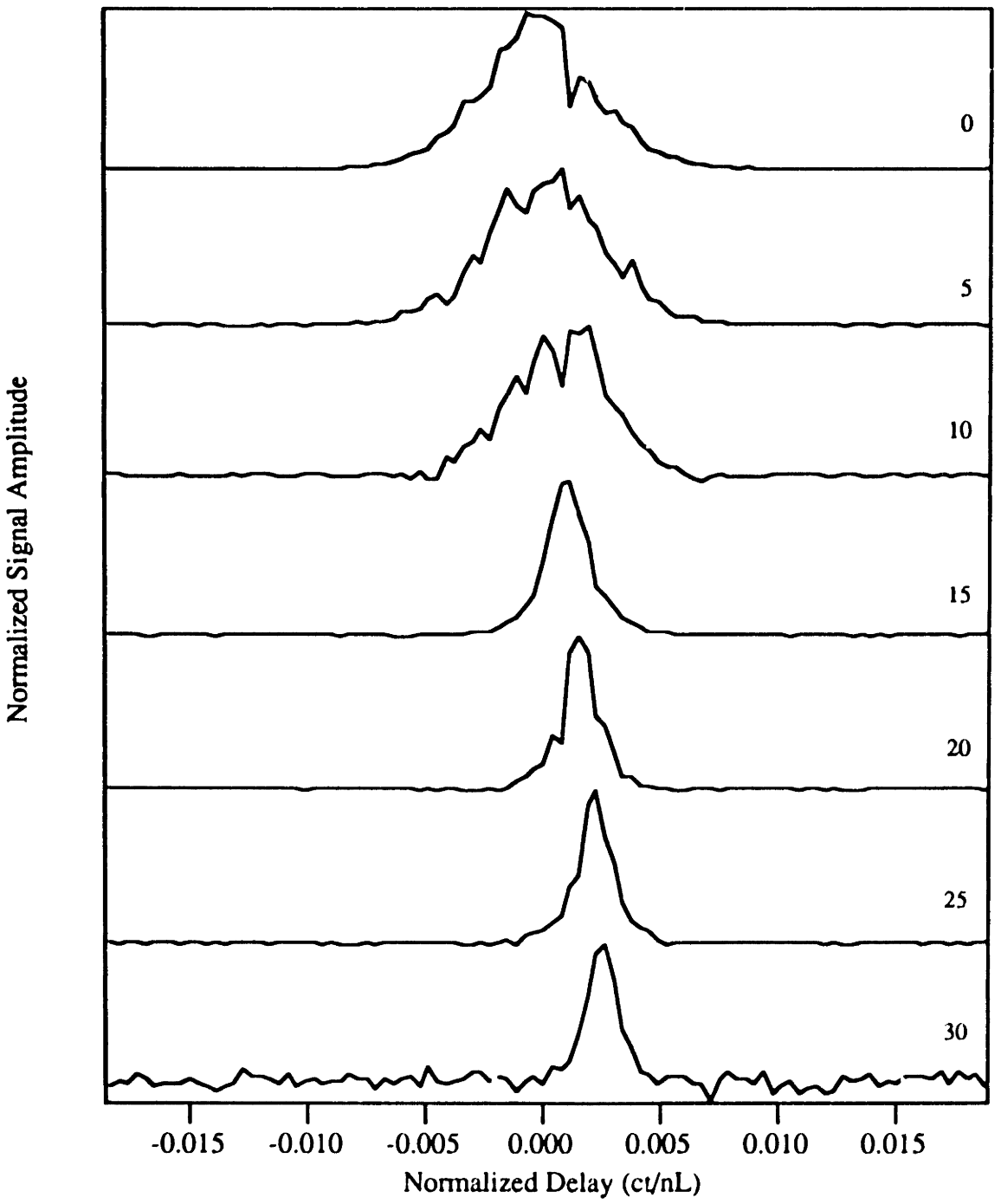

Figure 4.11. Coherence-gated scattering profiles for various concentrations of 100 nm microspheres ($g = 0.066$, $\sigma_s = 2.0 \times 10^{-13}$ cm^2) measured in the number of scattering MFPs contained in the $L = 4$ cm length cuvette. The normalized signal amplitude for each concentration is plotted versus the normalized delay parameter ct/nL, where t is the time delay, c/n is the speed of light in the medium, and L is the sample thickness.

ballistic peak increases with increasing concentration of microspheres, consistent with the incoherent detection results of Liu, *et. al.*[24] The delay may be explained by assuming that the ballistic light sees the average refractive index of the suspension since the particles are much smaller than a wavelength. The average index increases linearly with the number of scattering MFPs resulting in a delayed arrival time. Figure 4.12 displays the normalized arrival time of the ballistic peak versus the concentration of scattering microspheres in measured in number of scattering MFPs. The arrival time is linearly dependent on the particle concentration, as expected.

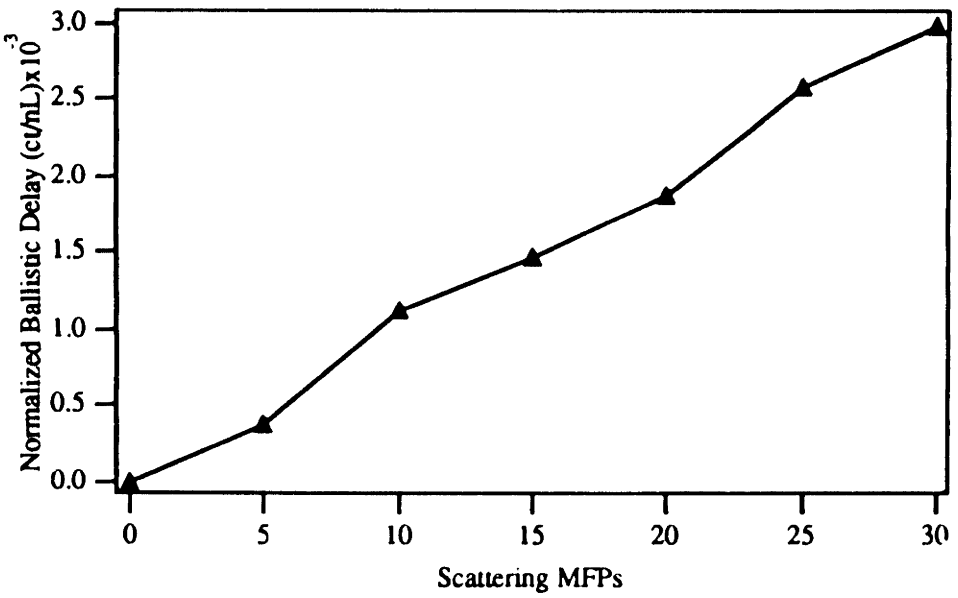

Figure 4.12. Normalized arrival time ct/nL of the ballistic peak versus the concentration of 100 nm microspheres measured in the number of scattering MFPs contained in the L = 4 cm length cuvette.

Figure 4.13 details the attenuation of the ballistic peak with sample thickness, or number of scattering MFPs. The ballistic peak attenuates exponentially with the number of scattering MFPs (least squares slope = -0.83). However, the attenuation does not go exactly as the number of MFPs as expected. This deviation may be accounted for by noting that even for a 4 cm length cuvette, there were still multiple particles contained within a cubic wavelength for most of the dilutions used. Thus, successive scattering events may have interacted, reducing the effective cross-section of each particle.

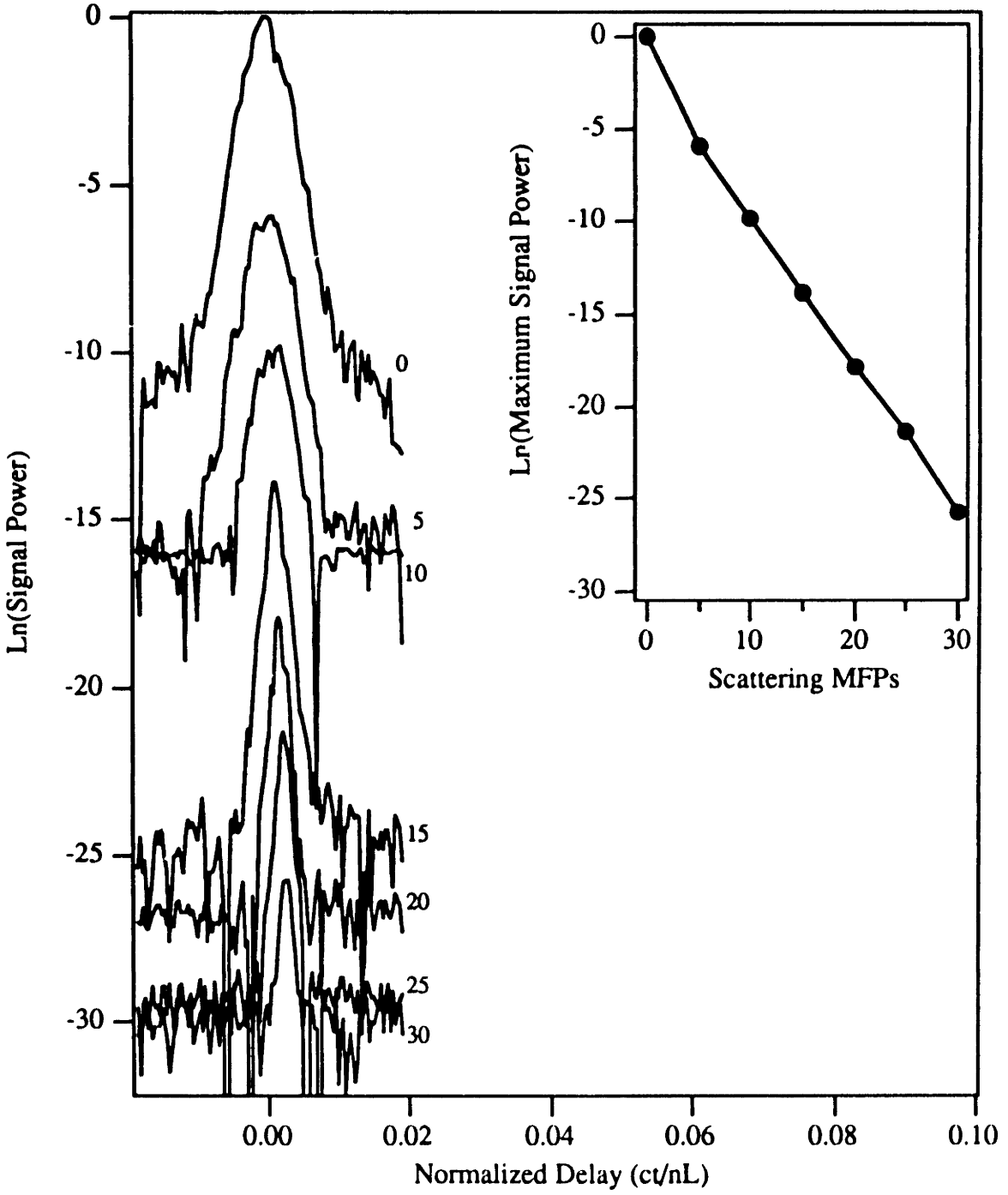

Figure 4.12. Coherence-gated scattering profiles for 100 nm microspheres displayed on a natural log scale. Inset: Attenuation of the ballistic and diffuse component peak signal power as a function of the number of scattering MFPs, or equivalent sample thickness.

References

1. C. F. Bohren and D. R. Huffman, *Absorption and Scattering of Light by Small Particles*, John Wiley & Sons, New York (1983).

2. J. D. Jackson, *Classical Electrodynamics, 2nd ed.*, John Wiley & Sons, New York (1975).

3. M. Kerker, *The Scattering of Light and Other Electromagnetic Radiation*, Academic Press, New York (1969).

4. A. Ishimaru, *Wave Propagation and Scattering in Random Media, vol. 1*, Academic Press, New York (1978).

5. R. Graaff, J. G. Aarnoudse, F. F. M. de Mul, and H. W. Jentink, "Light propagation parameters for anisotropically scattering media based on a rigorous solution of the transport equation," Appl. Opt. **28**, 2273-2279 (1989).

6. J. L. Karagiannes, Z. Zhang, B. Grosswiener, and L. I. Grossweiner, "Applications of the 1-D diffusion approximation to the optics of tissue and tissue phantoms," Appl. Opt. **28**, 2311-2317 (1989).

7. A. Ishimaru, "Diffusion of a pulse in densely distributed scatterers," J. Opt. Soc. Am. **68**, 1045-1050 (1978).

8. A. Ishimaru, "Diffusion of light in turbid material," Appl. Opt. **28**, 2210-2215 (1989).

9. A. E. Profio, "Light transport in tissue," Appl. Opt. **28**, 2216-2222 (1989).

10. G. Yoon, S. A. Prahl, and A. J. Welch, "Accuracies of the diffusion approximation and its similarity relations for laser irradiated biological media," Appl. Opt. **28**, 2250-2255 (1989).

11. K. M. Yoo, F. Liu, and R. R. Alfano, "When Does the Diffusion Approximation Fail to Describe Photon Transport in Random Media?" Phys. Rev. Lett. **64**, 2647-2660 (1990).

12. M. S. Patterson, B. Chance, and B. C. Wilson, "Time resolved reflectance and transmittance for the non-invasive measurement of tissue optical properties," Appl. Opt. **28**, 2331-2336 (1989).

13. K. M. Yoo and R. R. Alfano, "Determination of the scattering and absorption lengths from the temporal profile of a backscattered pulse," Opt. Lett. **15**, 276-278 (1990).

14. S. L. Jacques, "Time-Resolved Reflectance Spectroscopy in Turbid Tissues," IEEE Trans. Biomed. Engr. **36**, 1155-1161 (1989).

15. B. C. Wilson and S. L. Jacques, "Optical Reflectance and Transmittance of Tissues: Principles and Applications," IEEE J. Qauntum Electron. **26**, 2186-2199 (1990).

16. W. Cheong, S. A. Prahl, and A. J. Welch, "A Review of the Optical Properties of Biological Tissues," IEEE J. Quantum Electron. **26**, 2166-2185 (1990).

17. S. T. Flock, M. S. Patterson, B. C. Wilson, and D. R. Wyman, "Monte Carlc Modeling fo Light Propagation in Highly Scattering Tissues I: Model Predictions and Comparison with Diffusion Theory," IEEE Trans. Biomed. Engr. **36**, 1162-1168 (1989).

18. S. T. Flock, M. S. Patterson, B. C. Wilson, and D. R. Wyman, "Monte Carlo Modeling fo Light Propagation in Highly Scattering Tissues I: Comparison with Measurements in Phantoms," IEEE Trans. Biomed. Engr. **36**, 1162-1168 (1989).

19. S. L. Jacques, "Time resolved propagation of ultrashort laser pulses within turbid tissues," Appl. Opt. **28**, 2223-2229 (1989).

20. Y. Hasegawa, Y. Yamada, M. Tamura, and Y. Nomura, "Monte Carlo simulation of light transmission through living tissues," Appl. Opt. **30**, 4515-4520 (1991).

21. K. M. Yoo and R. R. Alfano, "Time-resolved coherent and incoherent components of forward light scattering in random media," Opt. Lett. **15**, 320-322 (1990).

22. Y. Kuga, A. Ishimaru, and A. P. Bruckner, "Experiments on picosecond pulse propagation in a diffuse medium," J. Opt. Soc. Am. **73**, 1812-1815 (1983).

23. J. C. Hebden, "Time-resolved attenuation of transmitted laser pulses by a homogeneous scattering medium," Opt. Lett. **17**, 444-446 (1992).

24. F. Liu, K. M. Yoo, and R. R. Alfano, "Speed of the coherent component of femtosecond laser pulses propagating through random scattering media," Opt. Lett. **15**, 351-353 (1991).

Chapter 5

Coherence-Gated Transillumination Imaging

5.1 Introduction

Two-dimensional shadowgram images of hidden objects embedded in scattering media may be obtained by using the coherence-gating properties of the transillumination system to temporally isolate the early arriving portion of light transmitted through the specimen. The reference path length delay is fixed so that the coherence-gate selects the least scattered light emerging from the sample. The specimen is raster scanned over each spatial resolution element.

The coherence-gated light scattering experiments described in Ch. 4 demonstrate that the directionally selected and phase coherent constituent of light transmitted through a scattering media consists of an early arriving, unscattered ballistic component, and a later arriving, temporally broadened, diffuse component. Imaging hidden objects with coherence-gated ballistic light is illustrated with the transillumination system and results in high resolution images. However, ballistic light images may only be acquired through relatively thin specimens due to signal attenuation. A fundamental sensitivity limit on ballistic imaging through turbid media is established for any optical imaging technique.

Images through thick samples may be obtained at the expense of reduced resolution by coherence-gating the forward scattered, or early arriving portion of the diffuse component, since the attenuation of diffuse light with sample thickness is less

severe. The trade-off between image resolution and increasingly later coherence-gate delay is experimentally investigated, and empirical resolution limits are proposed.

5.2 Ballistic Light Imaging

High resolution images of opaque objects in scattering media have been obtained with the coherence-gated transillumination system by setting the coherence-gate to select only the ballistic light and reject all diffuse light. Since the ballistic component of the transmitted light is completely unscattered, ballistic gated images are theoretically diffraction limited. As seen in Ch. 4, the ballistic component intensity attenuates exponentially with increasing number of scattering MFPs, or sample thickness. In light of this attenuation law, a fundamental shot noise limit may be established for ballistic imaging with any detection method. Purely spatially resolved imaging methods are shown to be inferior to time-gating methods for ballistic imaging.

5.2.1 Resolution Chart Between Microspheres

As an initial demonstration, a standard Air Force resolution chart was imaged between two 5 mm length cuvettes containing 1 μm diameter latex microspheres suspended in water. While this model scattering suspension only approximates the behavior of actual tissue, its scattering parameters may be accurately computed from Mie theory to allow quantitative assessment of system performance. Recall that Figs. 4.5 and 4.6 plot the time-resolved coherence-gated scattering profiles for various concentrations of these 1 μm microspheres.

Figure 5.1 shows images of the test chart obtained with the coherence-gated transillumination system with and without the scattering microspheres for various coherence gate delays. Each 130 x 100 pixel image took 13 minutes to acquire. The upper left image is a view of the resolution chart through water alone and is provided for reference. While keeping the reference pulse delay constant, scattering microspheres were added until the total length of the medium equaled 27 scattering mean-free-paths computed from Mie theory ($N\sigma L = 27$, where $N = 1.9 \times 10^{10}$ cm^{-3} is the number density of particles, $\sigma = 1.4 \times 10^{-8}$ cm^2 is the scattering cross section of a single particle computed from Mie theory, and $L = 1$ cm is the thickness of scattering medium). The lower right figure displays the resulting image obtained with 45 mW optical power

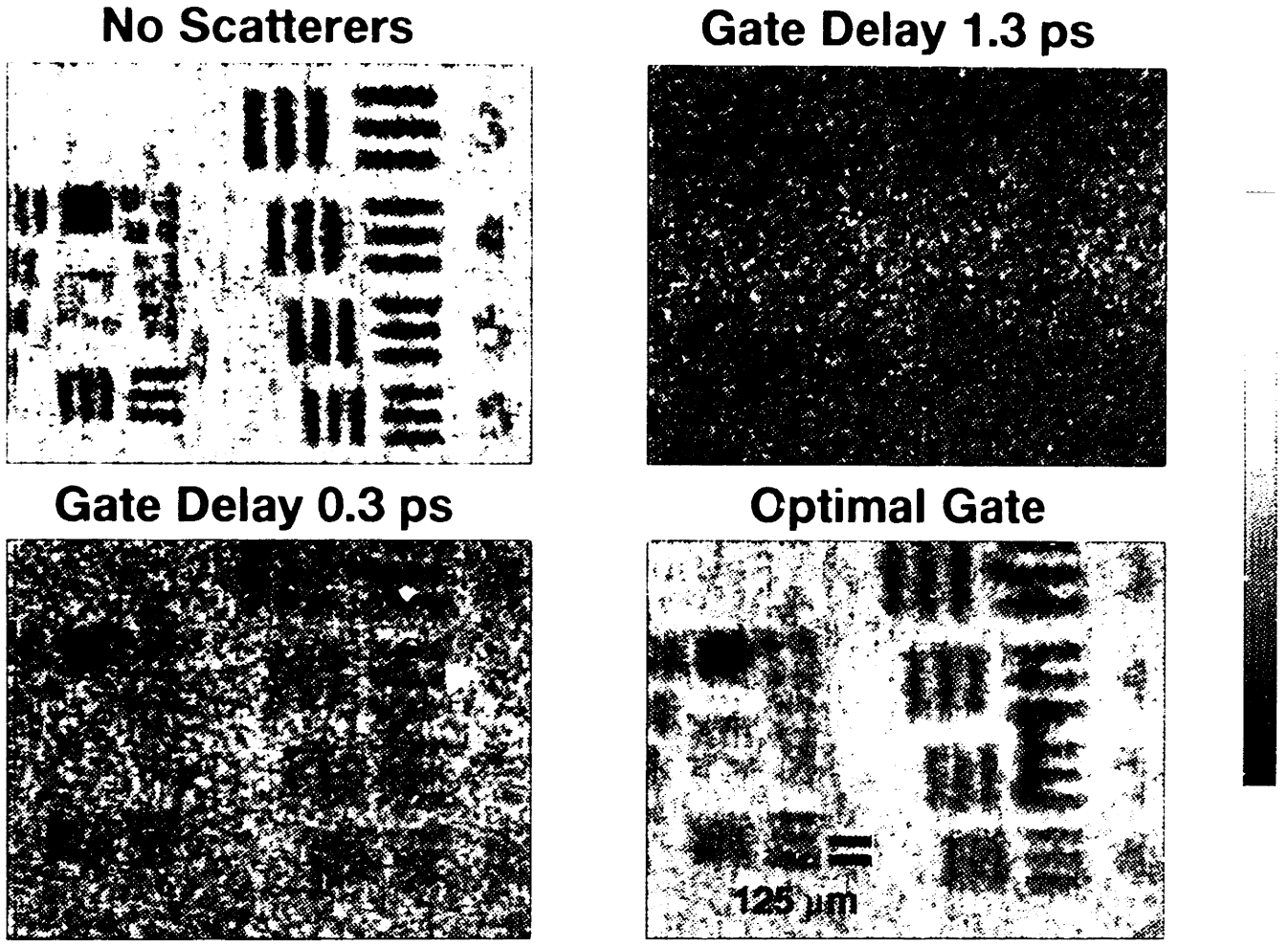

Figure 5.1. Ballistic light coherence-gated images of an Air Force resolution chart placed between two 5 mm length cuvettes containing 27 scattering MFPs of 1 µm diameter latex microspheres suspended in water.

incident on the scattering microspheres and an optical coherence-gate delay set to isolate only the ballistic light. The resolution chart is almost perfectly reconstructed with a 125 μm spatial resolution indicated by the group II, element 1 bars, demonstrating that the early light still retains image information. This image represents the highest resolution ever obtained through a similarly dense scattering media. With a slightly non-optimal coherence-gate (0.3 ps reference delay) the chart is degraded but still visible (lower left). With a 1.3 ps gate delay, the image consists entirely of diffuse light and no bars are resolved (upper right).

Since the ballistic component is completely unscattered, ballistic image resolution is theoretically diffraction limited. In practice, the resolution depends on the bandwidth of the low-pass frequency filter used for signal demodulation. Larger bandwidths increase resolution by reducing pixel size (see Eq. (3.100)), but also reduce sensitivity to transmitted light (Eq. (3.98)). For this particular application, the trade-off between scanning velocity and image resolution was designed to achieve approximately 100 μm spatial resolution (see Sec. 3.5.9).

5.2.2 Fundamental Sensitivity Limits

Figure 4.6 details the exponential attenuation of the ballistic and diffuse peaks versus increasing number of scattering MFPs, or equivalent sample thickness. Although ballistic gating provides high resolution images, the transmitted ballistic component attenuates by 1/e for every additional scattering MFP. Similar results for ballistic peak attenuation have been obtained with incoherent detection techniques. This fast exponential decrease for linearly increasing sample thickness means that ballistic images may only be acquired through relatively thin samples.

A fundamental limit on both coherent and incoherent ballistic imaging through turbid media may be established by noting that the presence or absence of ballistic light must be discernible from random intensity variations due to quantization. For the case of ideal detection, this shot noise limit may be computed from Eq. (3.98) by assuming a signal-to-noise ratio of 1 as the detectivity limit, and that the transmitted ballistic power attenuates according to $\exp(-\mu L)$, where $1/\mu$ is the mean-free-path between photon absorption or scattering events and L is the sample thickness. With these substitutions, the shot noise limit in Eq. (3.98) becomes

$$1 = \left(\frac{\eta}{\hbar\omega}\right)\frac{P_s e^{-\mu L}}{2 \cdot NEB}. \tag{5.1}$$

The sample power divided by the detection bandwidth, P_s/NEB, is approximately the total optical energy E delivered to each resolution element on the sample during detection (equal to P_s multiplied by the detection period). If ideal detectors are assumed ($\eta = 1$), then Eq. (5.1) simplifies to

$$L \approx \frac{1}{\mu}\ln\left(\frac{1}{2}\frac{E}{\hbar\omega}\right), \tag{5.2}$$

describing the maximum sample thickness through which a ballistic image may be obtained for a given incident energy E and a MFP $1/\mu$.

Equation (5.2) may be intuitively understood by noting that the quantity $E/\hbar\omega$ is the number of photons delivered to each resolution element during detection. For a sample of length L and MFP $1/\mu$, the average number of exiting photons N_p at each resolution element, assuming that there is no hidden object blocking the photon path, is given by

$$N_p = \frac{E}{\hbar\omega}e^{-\mu L}. \tag{5.3}$$

To determine whether a hidden object is in the photon path, the sample must be thin enough so that N_p is at least 1, since a photodetector will only see discrete photons. In fact, Eq. (5.2) states that N_p should be at least 2 to account for statistical variations in photon arrival time during the detection period.

The maximum sample thickness for ballistic imaging may be estimated by inserting some typical values for tissue optical properties into Eq. (5.2) and considering tissue damage thresholds. We assume 800 nm light, a 100 x 100 pixel image with 500 μm spatial resolution, and 10 minutes total acquisition time. For a scanning system, the ANSI Z136 standard maximum permissible exposure for skin at 800 nm is 1.5 J / cm^2 given the detection period of 60 ms per pixel. Thus, the maximum energy E deposited to each 2.5×10^{-3} cm^2 area pixel is 3.6 mJ. The photon energy $\hbar\omega$ at 800 nm is 2.5×10^{-19} J. Using these values in Eq. (5.2), the maximum tissue thickness is calculated to be $\mu L \approx 40$ MFPs.

Assuming a generous 100 μm MFP for skin, the maximum ballistic image tissue thickness is limited to about 4 mm. Since all of the assumed parameters above except for the MFP appear in the logarithm of Eq. (5.2), the 4 mm limit is very robust. Similarly, linear increases in optical power, data acquisition time, or number of averages only affect the maximum thickness as the logarithm and do not alter the limit appreciably. The shot noise limit is fundamental for any classical optical imaging technique which attempts to use ballistic light.

5.2.3 Limits of Spatial Rejection Techniques

The combined directional and temporal coherence selection of coherence-gated transillumination enables a comparison of both time and spatially resolved imaging techniques. Ballistic imaging with solely spatially resolved imaging methods, such as confocal imaging, optical heterodyning, and spatial incoherence techniques, cannot reach the quantum shot noise limit because a substantial amount of diffuse light may be spatially coherent at the detector aperture when enough scattering has occurred. The performance of spatial resolved techniques may be simulated with the coherence-gated transillumination system by integrating the interference signal magnitude over all coherence-gate delays. According to coherence-gated scattering profiles in Fig. 4.5, for high resolution images, spatial resolved methods are confined to the regime where the ballistic component intensity overwhelms the time-integrated diffuse component intensity, or in this case to specimens thinner than about 15 to 20 MFPs (less than approximately 2 mm of tissue assuming a 100 μm MFP).

5.3 Forward Scattered Diffuse Light Imaging

Most medical diagnostic applications require imaging through tissues substantially thicker than achievable by ballistic gating. Figure 4.6 shows that the transmitted diffuse peak exponentially attenuates about a factor of ten more slowly than the ballistic peak with increasing sample thickness. Thus, while ballistic gated images are restricted to tissues with millimeter thicknesses, the phase coherent constituent of the diffuse light can penetrate tissues on the order of centimeters thick. The early arriving component of the diffuse light represents multiply scattered light that is predominantly forward directed. This forward scattered light retains less image information than the

unscattered ballistic component, but still has traveled a relatively direct path through the specimen compared to the later arriving portion of the diffuse light.

In this section, the trade-off between resolution and coherence-gate delay is experimentally investigated. A simple geometric limit for the worst case spatial resolution for a given gate delay is derived. Experimental results suggest a potentially useful empirical expression for the best case resolution given a certain gate delay.

5.3.1 Diffuse Imaging Resolution

Since quantum noise prohibits ballistic imaging through thick turbid media, early arriving diffuse light must be used, at the expense of reduced spatial resolution. Incoherent time-gating techniques have demonstrated that centimeter size objects may be imaged by gating the first 10 to 100 ps of incoherent diffuse light[1-4]. The coherent scattering profiles in Fig. 4.6, however, show that directional (confocal) and phase coherence selection alone is already sufficient to eliminate diffuse light after only about 20 ps for a 5 mm thick object.

Millimeter level image resolution is probably contained only in the most forward scattered diffuse light. To quantify the relationship between photon arrival time and image resolution for forward scattered diffuse light, one-dimensional images were acquired of varying width opaque bars placed in the center of a 1 cm length cuvette containing 25 MFPs of 1 μm latex microspheres suspended in water. A sequence of one-dimensional images was acquired for each bar for progressively later coherence-gate delays. Figure 5.2 displays the resulting two dimensional datasets as false color images for a 500 μm, a 1 mm, and a 2 mm diameter bar. The coherence-gate delay increases horizontally to the right in each image and is measured in the length of water (mm) required to produce the equivalent optical delay. Each 100 x 100 pixel image was 5 times averaged to reduce the contribution of speckle noise and required 40 minutes of acquisition time.

The ballistic peak is conspicuous at zero delay in each image and sharply defines the boundaries of each object. As the coherence-gate delay is increased, the object boundaries become progressively obscured as more and more diffuse light is detected which has taken paths around the object. For spatial resolution elements (pixels) blocked by the bar, the diffuse light creeps inward toward the middle due to light paths around the object destroying resolution as the coherence-gate delay increases .

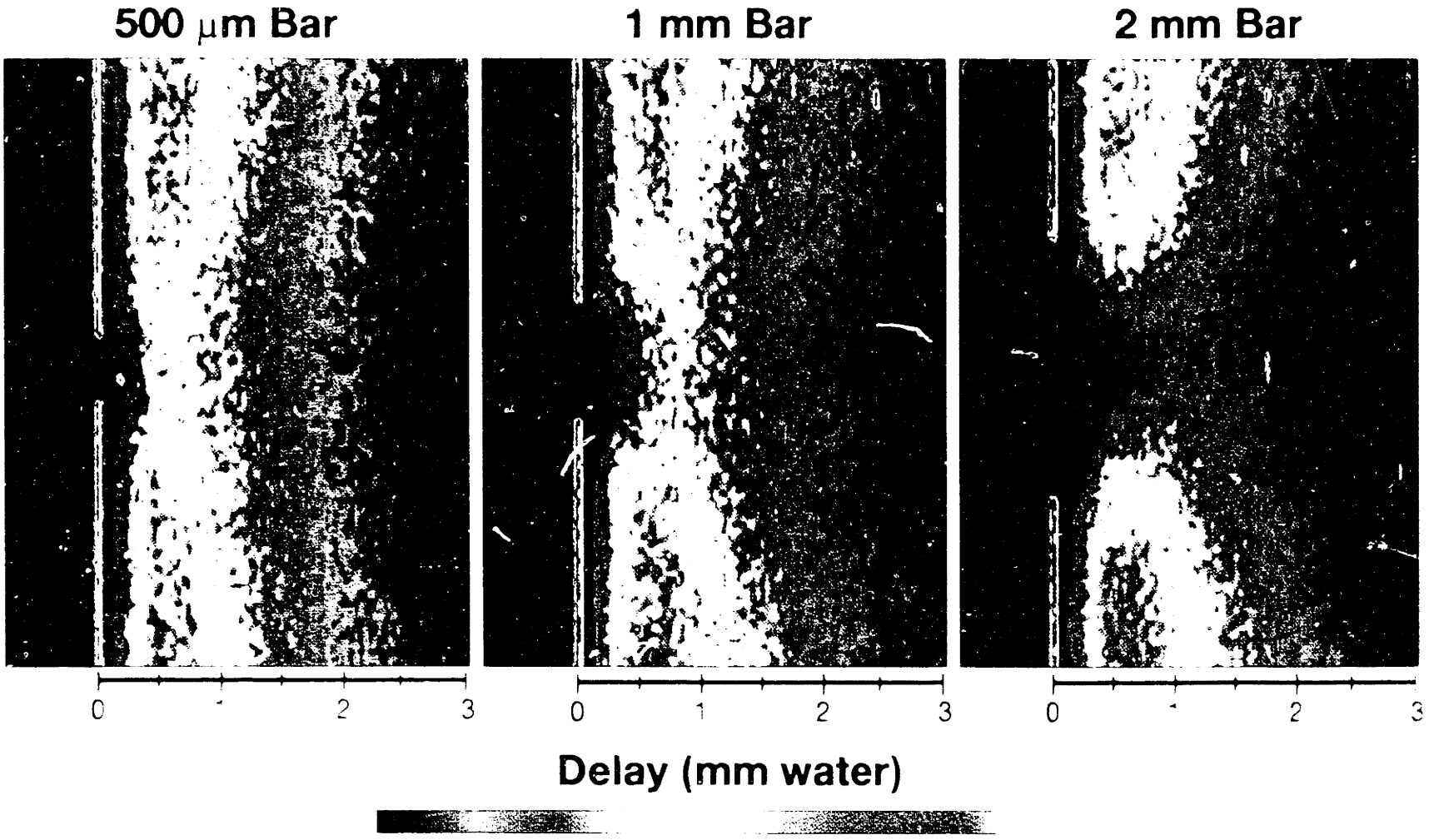

Figure 5.2. Coherence-gated images (false color) of a 500 μm, 1 mm and 2mm width bar placed in a 1 cm length cuvette containing 25 scattering MFPs of 1 μm diameter latex microspheres suspended in water. One-dimensional images of each bar (vertical) are plotted versus successive coherence-gate delay (horizontal) expressed in mm water.

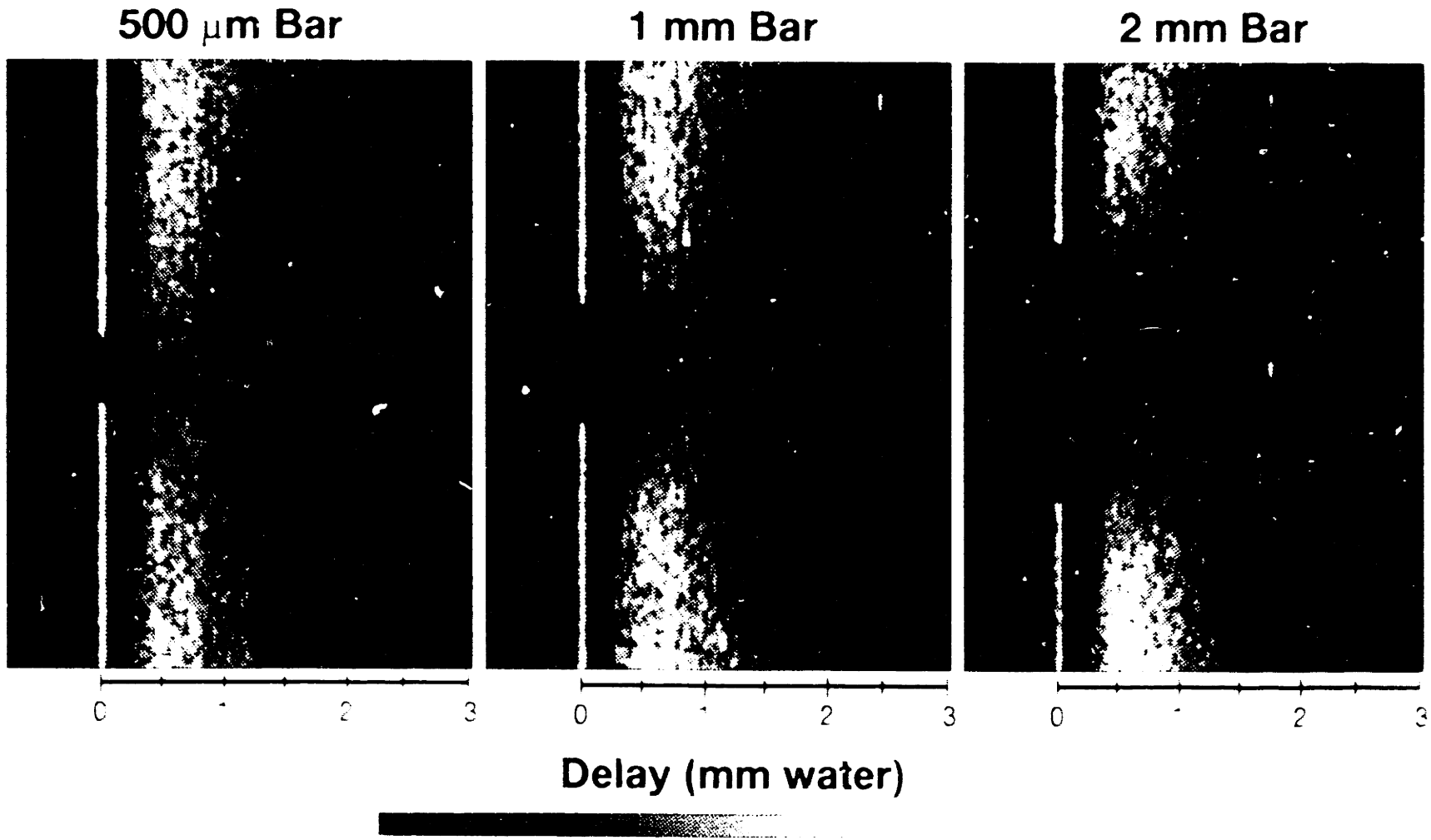

Figure 5.2 Coherence-gated images (grey scale) of a 500 μm, 1 mm and 2mm width bar placed in a 1 cm length cuvette containing 2% solution of 0.1 μm diameter latex microspheres suspended in water. One-dimensional images of each bar, vertical axis plotted versus success ve coherence-gate delay, horizontal, expressed in mm water.

The profile of the late arriving diffuse light is affected for spatial resolution elements far from the object. A reduction in diffuse tail intensity expands in a cone-like manner for increasingly late coherence-gate delays. Resolution elements far from the object are only affected once the coherence-gate delay is late enough so that a wandering diffuse light path travels enough transverse distance encounter the bar.

Recall that Fig. 4.6 plots the coherence-gated scattering profile for 25 MFPs of 1 μm microspheres suspended in a 5 mm length cuvette with no intervening bar. In the images of Fig. 5.2, the ballistic peak appears narrower and more distinct from the diffuse light compared to the profile in Fig. 4.6. Part of the narrowing is due to the fact that the FWHM temporal coherence-gate width Δt was 230 fs for the images in Fig. 5.2, and only 400 fs for the profiles in Fig. 4.6. The ballistic peak also appears narrower in Fig. 5.2 because a 10 mm instead of 5 mm length cuvette was used. The longer cuvette reduces the normalized coherence-gate width parameter $c\Delta t/nL$, providing an apparent additional factor of 2 increase in temporal resolution.

It is instructive to consider a simple geometric limit on the worst case spatial resolution possible for a given coherence-gate delay. If confocal spatial rejection is employed, then photons will only be detected if they exit the sample at approximately the same transverse spatial coordinate at which they entered. Given a sample of length L, we assume that the coherence-gate is set to only accept delayed photons which have traveled a total distance

$$L_{gate} = L\left(1 + \frac{ct}{nL}\right) \tag{5.4}$$

where ct/nL is the normalized delay parameter defined in Sec. 4.5. The photon paths which deviate the most in the transverse direction define the worst case spatial resolution, and fall on an ellipsoid with foci at the photon entrance and exit points. The worst case full width spatial resolution $2\Delta x$ equals the transverse diameter of this ellipsoid taken at the center of the sample, and is given by

$$2\Delta x = 2\sqrt{\left(\frac{L_{gate}}{2}\right)^2 - \left(\frac{L}{2}\right)^2}. \tag{5.5}$$

In terms of a normalized full width resolution parameter $2\Delta x/L$, Eq. (5.5) simplifies to the worst case geometric limit

$$\frac{2\Delta x}{L} = \sqrt{2\frac{ct}{nL} + \left(\frac{ct}{nL}\right)^2} \approx \sqrt{2\frac{ct}{nL}} \tag{5.6}$$

where we have assumed in the approximation that $ct/nL << 1$ for the forward scattered component of the diffuse light (also see Figs. 4.5 and 4.7). Since $ct/nL << 1$, Eq. (5.6) says that the geometric resolution limit is slightly worse than a purely linear degradation of resolution with increasing delay, which would be described by

$$\frac{2\Delta \tilde{x}}{L} = 2\frac{ct}{nL}. \tag{5.7}$$

The actual degradation in resolution for increasing coherence-gate delay was empirically determined for the 2 mm bar image displayed in Fig. 5.2. The full width resolution for a given delay was calculated by hand as the transition length, from minimum to maximum interference signal amplitude, of the image of one edge of the bar. Fig. 5.3 plots the experimentally observed normalized resolution parameter $2\Delta x/L$ versus the normalized coherence-gate delay ct/nL. The normalized coherence-gate delay extends out to an actual distance delay of $ct/n = 0.53$ mm, since the sample length $L = 10$ mm. The observed resolution is seen to fall in between the geometric limit and linear degradation, computed from Eqs. (5.6) and (5.7) respectively.

For all gate delays shown, the observed resolution is never better than the linear degradation case. Thus, the linear degradation defined by Eq. (5.7) is potentially useful as a best case normalized full width resolution estimate for a given normalized coherence-gate delay. More experimental investigation is needed to determine whether this limit holds for different scattering anisotropies and for incoherent detection time-gating techniques. However, it is reasonable to assume that the resolution provided by incoherent detection methods as a function of time-gate delay will not be significantly different than the results shown here for coherent detection.

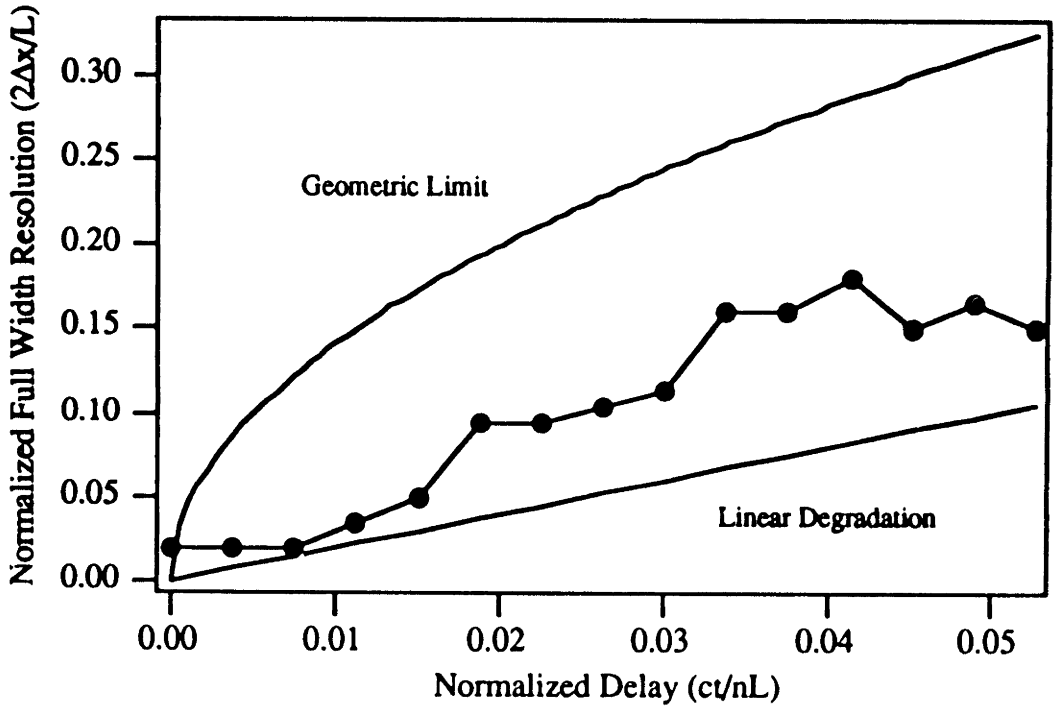

Figure 5.3. Experimentally observed degradation of spatial resolution with increasing coherence-gate delay for a 2 mm opaque bar placed in the center of a 1 cm cuvette containing 25 MFPs of 1 μm diameter microspheres suspended in water. Normalized full width resolution $2\Delta x/L$ is plotted versus normalized delay ct/nL. The worst case geometric limit curve and linear resolution degradation curve defined by Eqs. (5.6) and (5.7) respectively are plotted for reference.

5.3.2 Diffuse Imaging Thickness

It is tempting to formulate a fundamental limit on forward scattered diffuse imaging thickness by considering the attenuation of the diffuse peak with increasing numbers of scattering MFPs. With coherence-gated transillumination, the diffuse peak was observed to exponentially attenuate about a factor of 10 more slowly with sample thickness than the ballistic peak for both 1 μm and 10 μm particles (Figs. 4.6 and 4.8). Kuga, *et. al.*[5] have also reported that the diffuse peak attenuates a factor of 10 more slowly for particle diameters of 0.481 μm, 2.02 μm, and 5.7 μm with an incoherent detection technique. Thus, it appears that the diffuse peak attenuation is largely independent of scattering anisotropy for both coherent and incoherent detection methods. If in fact the attenuation rate remains constant for very large numbers of MFPs, then the shot noise limit on diffuse imaging tissue thickness will be approximately 10 times the ballistic limit, or about 4 cm.

It is not clear, however, that the diffuse attenuation rate will remain constant as the number of MFPs is increased. Diffusion theory predicts that the attenuation rate for forward scattered light should go as the forward scattering MFP which is 25 times longer than the scattering MFP for 1 μm microspheres and 500 times longer for 10 μm particles. The experiments performed here and by Kuga, *et. al.*[5] were limited to concentrations less than 50 MFPs which is equivalent to only a few forward scattering MFPs, so that diffusion theory may not be valid. In the thick sample limit, it is possible that the diffuse peak attenuation rate will level off to the less severe forward scattering MFP attenuation rate predicted by diffusion theory.

References

1. K. M. Yoo, B. B. Das, and R. R. Alfano, "Imaging of a translucent object hidden in a highly scattering medium from the early portion of the diffuse component of a transmitted ultrafast laser pulse," Opt. Lett. **17**, 958-960 (1992).

2. J. C. Hebden, R. A. Kruger, and K. S. Wong, "Time resolved imaging through a highly scattering medium," Appl. Opt. **30**, 788-794 (1991).

3. S. Andersson-Engels, R. Berg, S. Svanberg, and O. Jarlman, "Time-resolved transillumination for medical diagnostics," Opt. Lett. **15**, 1179-1181 (1990).

4. D. A. Benaron, M. A. Lennox, and D. K. Stevenson, "2-D and 3-D images of thick tissue using time-contrained times-of-flight and absorbance (tc-TOFA) spectrophotometry," unpublished manuscript.

5. Y. Kuga, A. Ishimaru, and A. P. Bruckner, "Experiments on picosecond pulse propagation in a diffuse medium," J. Opt. Soc. Am. **73**, 1812-1815 (1983).

Chapter 6

Summary and Conclusions

Coherence-gated transillumination has been developed as a new coherent imaging technique which takes advantage of both temporal and confocal directional rejection of scattered light. The system achieves a quantum shot noise limited 130 dB detection sensitivity to transmitted light with 50 mW incident on the sample. Two-dimensional raster scanning of the specimen is required; however, this is not a limitation since in a given detection time, the same optical energy may be delivered to a sample as in a two-dimensional imaging technique.

Using coherence-gated transillumination, time-resolved coherent scattering profiles have been investigated for the first time with a coherent detection method. Calibrated suspensions of 1 μm, 10 μm, and 100 nm diameter latex microspheres have been used and scattering profiles have been related to parameters derived from Mie scattering theory. Consistent with earlier studies of time-resolved scattering using incoherent detection, light transmitted through a scattering media emerges in two distinct components: an early arriving, unscattered ballistic peak, and a later arriving, temporally broadened diffuse component. Compared to previous results with incoherent detection methods, the coherent diffuse component displays a markedly reduced temporal extent due to the combined spatial and phase coherence requirement on detected light.

Coherence-gated scattering experiments have shown that the arrival time and temporal width of the diffuse peak depends on the scattering anisotropy. Diffuse light propagating through highly forward scattering, large diameter spheres arrives earlier and displays a narrower temporal extent compared to smaller sized particles.

The attenuation of the ballistic and diffuse component peak powers has been investigated as a function of sample thickness defined in number of scattering mean-free-paths (MFPs). The ballistic peak, consisting of completely unscattered light, exponentially attenuates by exactly a factor of $1/e$ for every additional scattering MFP, limiting detectable ballistic light transmission to relatively thin samples. The transmitted diffuse peak power dominates the ballistic light for samples thicker than about 25 MFPs, fairly independent of scattering anisotropy. Compared to the ballistic light, the diffuse peak attenuates about a factor of 10 more slowly in the exponential with increasing sample thickness also relatively independent of scattering anisotropy. Quantitatively similar results have been observed with incoherent detection methods.

Two-dimensional transillumination images of hidden objects embedded in scattering media were demonstrated with the coherence-gated transillumination system. High resolution (100 μm) images of an Air Force resolution test chart were obtained by coherence-gating the ballistic component of light transmitted through 27 scattering MFPs of 1 μm microspheres suspended in water.

The spatial resolution of ballistic imaging is theoretically diffraction limited; however, imaging with ballistic light is virtually impossible through thick objects due to the fast exponential attenuation of the ballistic component with increasing sample thickness. The quantum shot noise detection limit and tissue damage thresholds restrict ballistic images to about 4 mm thick tissue samples. Linear increases in optical power, detection time, or number of averages only affect this maximum thickness as the logarithm and do not alter the limit appreciably.

The combined temporal and directional rejection of scattered light with the coherence-gated transillumination system allows a comparison of time and spatially resolved imaging techniques. A spatial resolved imaging technique will see light detected by the coherence-gated transillumination system integrated over all possible coherence-gate delays. Coherence-gated scattering experiments in microsphere suspensions have shown that ballistic imaging is impossible for solely spatial resolved imaging techniques, such as confocal imaging, because a substantial amount of diffuse light may be coherent at the detector when the sample is thicker than about 20 MFPs.

Since ballistic gated imaging is fundamentally limited to thin samples, diffuse light must be used to penetrate thick specimens. The diffuse peak was found to attenuate about factor of 10 more slowly in the exponential compared to ballistic light, making

possible images through tissues of centimeter magnitude thicknesses. Spatial resolution is sacrificed for increasingly late time-gate delays. The degradation in resolution for increasing coherence-gate delay was empirically characterized for various sized opaque bars placed in 25 scattering MFPs of 1 μm diameter microspheres. The spatial resolution for a given gate delay was found to be bounded above and below by a simple worst case geometrical resolution limit, and an empirically determined best case limit.

The fundamental signal attenuation and resolution limits described in this thesis indicate that time-gated optical transillumination through real biological tissue will necessarily involve reduced spatial resolution imaging using the forward scattered portion of the diffuse transmitted light. Given the constraints described here, the stage is now set to investigate whether specific biomedical imaging problems can be solved with optical imaging systems optimally designed to operate within these limits.